

The composition of the lithospheric mantle beneath the Karowe Mine and its associated diamond sources in north-eastern Botswana

by

Theetso Motsamai

A thesis submitted in partial fulfillment of the requirements for the degree of

Doctor of Philosophy

Department of Earth and Atmospheric Sciences
University of Alberta

© Theetso Motsamai, 2018

Abstract

This study presents the first comprehensive data on the recently developed Karowe diamond mine from the Orapa kimberlite cluster, which hosts mines such as Orapa, Damtshaa, and Letlhakane. The objectives of the study were to establish the compositional characteristics of the lithospheric mantle beneath the Karowe mine at the time of kimberlite eruption by studying the major- and trace-element characteristics of 24 mantle xenoliths and 106 clinopyroxene xenocrysts. In addition, the possible diamond sources beneath Karowe were evaluated through examination of major- and trace-element compositions of mineral inclusions in 120 diamonds. Finally, the physical characteristics of the diamonds themselves as well as their total nitrogen contents and carbon isotope compositions were investigated.

The mantle xenoliths are predominantly melt-depleted garnet-free spinel peridotites ($n = 14$), with a small proportion of pervasively refertilised garnet-spinel lherzolites ($n = 4$), and variably metasomatised garnet-bearing pyroxenites ($n = 3$). The remaining three xenoliths are a garnet lherzolite, an eclogite, and a megacrystic olivine. The mineralogical evidence indicates that all these come from relatively low-pressure regions of the mantle outside of the diamond stability field. The predominant spinel lherzolites are characterised by coarse-grained and granolublastic textures, exsolution lamellae in clinopyroxenes and orthopyroxenes, and low equilibration temperatures (630 to 800 °C). They have high Mg# in olivines (median: 92.1) and orthopyroxenes (median: 92.4) as well as variable Cr# in spinels (13 to 47; median: 37). Clinopyroxenes show variable LREE_N enrichment ($La_N/Sm_N=0.24$ to 3.8) which is consistent with secondary re-enrichment processes. Trace element compositions of the garnets and clinopyroxenes in the garnet-bearing xenoliths indicate cryptic melt metasomatism as well as modal metasomatism associated with the introduction of phlogopite. Clinopyroxene-based geothermobarometry on

clinopyroxene xenocrysts (25 out of the 106) and one garnet lherzolite xenolith indicate a 39 to 40 mW/m² model paleogeotherm, which overlaps at greater depths with two non-touching garnet-orthopyroxene inclusion pairs recovered from Karowe diamonds. These data imply that the lithospheric mantle beneath Karowe is 210 km thick with a diamond window of approximately 90 km thickness, which is consistent with other estimates of lithospheric depths in this region of the Zimbabwe Craton derived from petrology and geophysics.

The major- and trace-element compositions of mineral inclusions in the diamonds indicate that 53 % are derived from eclogitic sources, 44 % are peridotitic, 2% have a sublithospheric origin, and 1 % are websteritic. The sublithospheric inclusion suite consists of three eclogitic garnets containing a majorite component (>6.12 to 6.46 apfu Si; with [O] = 24). This new observation of superdeep mineral inclusions in Karowe diamonds is unique within the Orapa cluster and may provide a key link to the presence of exceptionally large diamonds from this mine.

From the present diamond suite, Karowe diamonds have variable morphologies with a dominance of octahedra (30 %), macles (20 %), and moderately resorbed morphologies (transitional between octahedra and dodecahedra; 18 %). The remaining 32 % are made up of 10 % rounded dodecahedra, 4 % cubo-octahedra, 2 % pseudo-hemimorphic and 16 % aggregated crystals. Overall, diamonds have FTIR nitrogen contents that range from below the limit of detection (≤ 15 at.ppm) to 1217 at.ppm with variable nitrogen aggregation states (0 to 100 %B) and $\delta^{13}\text{C}$ values from -34.5 to -2.0 ‰. Both eclogitic and peridotitic diamonds show the same wide range in nitrogen aggregation states (0 to 100 %B), have the same median value of 39 %B and fall into two distinct groups: a dominant population of Type IaA to IaAB diamonds with less than 70 %B and a minor population of highly aggregated Type IaAB to IaB (80 to 100 %B) diamonds.

Eclogitic diamonds contain 24 to 1217 at.ppm nitrogen with a median of 513 at.ppm and their carbon isotope compositions range between -21.5 and -2.5 ‰ with a median at -4.9 ‰. Peridotitic diamonds contain up to 937 at.ppm nitrogen with a median of 129 at.ppm. The majority of peridotitic diamonds fall into a typical mantle-like $\delta^{13}\text{C}$ range (-8.6 to -2.0 ‰), with the exception of two diamonds that display unusual strongly ^{13}C -depleted isotope compositions (-34.5 and -14.9 ‰). The mode in $\delta^{13}\text{C}$ values for peridotitic diamonds (in class -4.0 to -3.5 ‰) is offset by about +1 ‰ relative to eclogitic diamonds (mode in class -5.0 to -4.5 ‰). These results could reflect derivation of mantle-like carbon from different sources through time for the two main parageneses or relate to the speciation of carbon fluids with constant $\delta^{13}\text{C}$ (e.g., a minor increase in the CO_2/CH_4 ratio in the diamond-forming fluid from peridotitic to eclogitic diamonds).

Preface

All the work presented here is original and was conducted under the supervision of Professor Thomas Stachel.

The thesis is organized as follows: A modified version of **Chapter 2** will be submitted to South African Journal of Geology for publication as: *Motsamai T, Stachel T, Pearson DG, Harris JW, Armstrong J. The compositional structure and thermal state of the lithospheric mantle beneath Karowe Mine, north-eastern Botswana.* The samples were collected by J Armstrong (Lucara Diamond Corporation). T Motsamai prepared the samples and conducted all analytical work as well as writing the initial manuscript, while T Stachel, DG Pearson and JW Harris contributed to the discussion of results and their implications, as well as other valuable edits that improved this manuscript.

Chapter 3 has been modified and published as: *Motsamai T, Harris JW, Stachel T, Pearson DG, Armstrong J (2018) Mineral inclusions in diamonds from Karowe Mine, Botswana: super-deep sources for super-sized diamonds. Mineralogy and Petrology. Proceedings of the 11th International Kimberlite Conference.* For the purpose of this research, Lucara Diamond Corporation donated the diamond samples from their Karowe mine production. JW Harris and J Armstrong helped with the selection of samples, while T Motsamai characterised and conducted all the analytical work as well as writing up the first draft of the manuscript. In addition, JW Harris provided constructive criticism in the initial drafts of this manuscript. T Stachel and D G Pearson contributed to the discussion of results and their implications that helped to improve this manuscript.

A modified version of **Chapter 4** will be submitted to LITHOS for publication as: *Motsamai T, Stachel T, Pearson DG, Harris JW, Stern AR, Armstrong J. Physical characteristics,*

nitrogen content and carbon isotope composition of diamonds from the Karowe Mine in Botswana.

Diamonds were provided by Lucara Diamond Corporation (J Armstrong). T Motsamai conducted FTIR analysis and characterised diamonds as well as writing up the first draft of the manuscript. Carbon isotope and nitrogen content analyses by SIMS were performed by RA Stern with assistance of T Motsamai. T Stachel, JW Harris, and DG Pearson provided valuable discussions that helped to improve this manuscript.

The main findings of this thesis are summarised in **Chapter 5**.

Acknowledgements

I would like to express my deepest gratitude to my supervisor Thomas Stachel for his generous support, professional guidance, and constructive criticism to many drafts of this thesis, which greatly improved my writing skills.

The biggest thanks go to Jeffrey Harris who introduced me to the world of diamonds. I will always cherish this opportunity.

Many thanks go to Graham Pearson for all the encouragement and support throughout this project.

I would also like to thank my entire examining committee: Britta Jensen, Thomas Chacko and Gerhard Brey for agreeing to be examiners during my PhD thesis

The expert technical assistance from all our laboratory personnel was valuable and greatly appreciated, especially from Andrew Locock, Yan Luo, Martin von Dollen and Igor Jakab.

I received a bursary from the Government of Botswana as part of Pre-University Academic Programmes under Botswana International University of Science and Technology (BIUST) and this is sincerely acknowledged. Through Thomas Stachel, research funding was also received from an NSERC Discovery grant and the Canada Research Chairs program.

Lucara Diamond Corporation is thanked and in particular John Armstrong for the provision of samples studied in this project and financial support of diamond collection, while John Gurney is thanked for being a champion for this project on board of Lucara.

I would like to thank everyone within the Department of Earth and Atmospheric Sciences and elsewhere, for their support and input through this project. In particular Matthew Hardman, Janina Czas, Nicole Meyer, Mandy Krebs, Yannick Bussweiler, Dikabo Mogopodi, and Tebogo Leepile who continued to exchange scientific ideas with me and edited my draft manuscripts.

Lastly, my special thanks are extended to my wife Boikhutso, my children Atlang and Ame, and my whole family for their love and encouragement during my study.

List of Tables

Table 2.0 Equilibrium pressure and temperature estimates for Karowe xenoliths -----29-31

Table 3.0 Summary of analysed mineral inclusions contained in 107 Karowe diamonds and their parageneses -----46

Table 3.1 Estimated equilibrium pressures and temperatures for coexisting minerals inclusions in Karowe diamonds -----63

Table 4.0 Morphologies and colours observed in inclusion-bearing diamonds from Karowe----80

Table 4.1 Integrated platelet peak areas, concentrations of nitrogen in B-centers and model temperatures for selected samples processed with the Speich et al. (2018) program and derived using a manual approach (*)-----87

Appendix A

Table A1 Natural minerals and synthetic materials used as calibration standards for analyses of mineral grains from xenoliths as well as mineral inclusion in diaomds -----128-129

Table A2 Major element mineral compositions and modal proportions of 24 mantle xenoliths from Karowe mine -----130

Table A3 Major element compositions of clinopyroxene xenocrysts -----130

Table A4 Trace element concentrations of clinopyroxenes and garnets in peridotite, pyroxenite, and eclogite xenoliths from Karowe-----130

Appendix B

Table B1 Major- (in wt%) and trace-element (in ppm) compositions of mineral inclusions from Karowe diamonds. For trace element concentrations, the BCR2G reference material was used to confirm precision and accuracy of the results -----130

Table B2 Composition of sulphide inclusions from Karowe diamonds, reported in both wt% and at.% -----130

Table B3 Eclogitic bulk rock compositions (oxides in wt%, trace elements in ppm) reconstructed for 50% garnet and 50% cpx (by weight), with N-MORB trace element compositions from Sun and McDonough (1989) -----130

Appendix C

Table C1 Physical characteristics, FTIR and SIMS analysis result for Karowe diamonds-----130

List of figures

- Fig. 1.1** Map of Botswana showing the location of the Karowe mine kimberlites within the Orapa cluster block (map modified after Brook 2012). Also shown for reference are the tectonic units of the Kalahari Super-Craton from Key and Ayres (2000) -----7
- Fig. 2.0** Photomicrographs showing a) irregular shaped spinel and b) textural relationship of spinel and garnet in the garnet-spinel lherzolite suite. In xenolith AK6-03 (above), spinels have ‘skeleton’ shape appearance, while in sample AK6-09 (below) garnets have ‘sieve’ texture appearance -----14
- Fig. 2.1** Triangular diagram for the classification of ultrabasic rocks based on the proportions of olivine (ol), orthopyroxene (opx) and clinopyroxene (cpx) after Streckeisen (1976), showing garnet peridotites (AK6-10 and AK6-19) and spinel peridotites from Karowe. The other two garnet pyroxenites are not shown because they contain only clinopyroxene and garnet. Primitive Mantle (PM) for spinel facies (McDonough and Rudnick 1998)-----15
- Fig. 2.2** Photomicrographs showing: a) exsolved clinopyroxene textures from sample AK6-15 (circled area; above). b) Equilibrated 120-degree grain boundaries defining interlocking fabric for Group II eclogite in sample AK6-25 -----17
- Fig. 2.3** Composition of olivines for Karowe and Letlhakane xenoliths (western edge of the Zimbabwe craton; Stiefenhofer et al. 1997) and Murowa-Sese xenoliths (southern part of the Zimbabwe craton; Smith et al. 2009) -----19
- Fig. 2.4** Plot of TiO_2 vs Al_2O_3 for orthopyroxenes from spinel lherzolite, garnet-spinel lherzolite and garnet lherzolite suites. Compositional fields shown are for garnets and spinel peridotites from McDonough and Rudnick (1988) -----19
- Fig. 2.5** Plot of Na+K versus Al cations for clinopyroxene from Karowe mantle xenoliths. Clinopyroxenes coexisting with spinel and garnet/spinel show excess of Al over Na indicative of the presence of a Tscherma component. AK6-03 and AK6-24 are clinopyroxenes with exsolution lamellae. Dashed line indicates a 1:1 ratio between Na and Al -----20
- Fig. 2.6** CaO vs Cr_2O_3 diagram with compositional fields from Grütter et al. (2004). Garnets from xenoliths are shown in comparison with the data from inclusions in Karowe diamonds (Motsamai et al. 2018) -----21
- Fig. 2.7** Plot of Cr_2O_3 vs TiO_2 in spinel from Karowe spinel lherzolite and garnet-spinel lherzolite suites -----22
- Fig. 2.8** C1 chondrite normalized (McDonough and Sun 1995) REE_N patterns of clinopyroxenes from the Karowe spinel lherzolite suite compared to Letlhakane (Borst 2012) -----23

Fig. 2.9 C1-chondrite normalized (McDonough and Sun 1995) REE patterns in clinopyroxenes from (a) garnet/spinel facies and (b) pyroxenite/eclogite xenoliths -----23

Fig. 2.10 C1-chondrite normalized (McDonough and Sun 1995) REE patterns of garnets from (a) garnet/spinel facies and (b) pyroxenite/eclogite xenolith suites -----24

Fig. 2.11 Comparison of calculated temperatures for spinel lherzolite and garnet-spinel lherzolite xenoliths from Karowe using the two thermometers from Taylor (1998) in grey and Brey and Köhler (1990) in red -----25

Fig. 2.12 Cr-diopside single grain pressure-temperature (P-T) results obtained using Nimis and Taylor (2000) geothermobarometry compared with two non-touching garnet-orthopyroxene inclusions pairs from Karowe diamonds (Brey and Köhler 1990; Harley 1984) and from Letlhakane peridotitic xenoliths (Brey and Köhler 1990). Model geotherms for 38 to 42mW/m² surface heat flow are from Hasterok and Chapman (2011) while the graphite-diamond transition (G/D) is from Day (2012) -----26

Fig. 2.13 FITPLOT geotherm regression showing the modelled geotherm for Karowe xenocrysts using the geothermobarometer of Nimis and Taylor and a single garnet lherzolite xenolith (Nickel and Green 1985; Brey and Köhler 1990). The model geotherm has crustal heat production of 0.86 $\mu\text{W}/\text{m}^3$ in accordance with models of Kramers et al. (2001) while the graphite-diamond transition (G/D) is from (Day 2012). Error envelop denotes the 1-sigma uncertainty in the fit to the depth parameter -----27

Fig. 2.14 Y versus Zr for garnets from peridotitic xenoliths shown plus garnet inclusions within diamonds from Karowe (Motsamai et al. 2018). Trends of melt- and fluid-style (phlogopite) metasomatism are for garnet xenocrysts from Griffin and Ryan (1995). MARID-like metasomatism (Creighton et al. 2009) -----32

Fig. 2.15 Mg # of olivine vs percent melting (F) in residual peridotites from experiments at varying pressure starting compositions (after Pearson & Wittig 2008). Fitting the median value of olivine Mg# in Karowe peridotites to the data predict melt extraction between ~27 and ~36%. The range is represented with bars on the Y-axis -----37

Fig. 2.16 Correlation of HREE contents (Yb) with increasing Mg# in clinopyroxenes -----38

Fig. 3.0 Na+K versus Al cations for clinopyroxene inclusions from Karowe diamonds. Omphacitic clinopyroxenes show excess of Al over Na indicative of the presence of a Tschermaks component. Dashed line indicates a 1:1 ratio between Na and Al -----49

Fig. 3.1 Sulphide compositions in Fe-Ni-S quadrilateral (based on atomic percentages). Filled red circles indicate an eclogitic paragenesis based on coexisting silicate and oxide inclusions while filled blue circles reflect an eclogitic paragenesis inferred from sulphide compositions. Similarly,

for the peridotitic suite filled and open symbol were used to reflect observed and inferred paragenesis. Compositional fields from Deines and Harris (1995) and small white circles from Stachel and Harris (2008) -----50

Fig. 3.2 Cr₂O₃ vs CaO diagram for garnets inclusions in Karowe diamonds. Isobars are from Grütter et al. (2006) and represent minimum pressures (as equilibrium with spinel is not established) -----52

Fig. 3.3 NiO (wt%) versus molar Mg# (100×Mg/[Mg+Fe]) in olivine inclusions from this study and localities worldwide (n=1,306; Stachel and Harris 2008) -----52

Fig. 3.4 Chondrite normalized (McDonough and Sun 1995) REE patterns for Karowe eclogitic garnet inclusions. **a:** Low-Ca garnets (n=3) and high-Ca garnets (n=6). **b:** Second group of high-Ca garnets with nearly flat REE patterns -----56

Fig. 3.5 Chondrite normalized (McDonough and Sun, 1995) REE patterns for Karowe eclogitic clinopyroxene inclusions. **a:** Similar, comparatively flat REE_N patterns for omphacites (n=6) and low-Cr augites (n=3). **b:** Four unusual (steeper MREE_N-HREE_N slopes) patterns for omphacitic samples -----57

Fig. 3.6 Reconstructed whole-rock REE_N for eclogitic bulk rocks associated with high- and low-Ca garnets (assuming garnet:clinopyroxene=1:1). N-MORB composition is from Sun and McDonough (1989) -----58

Fig. 3.7 Chondrite normalized (McDonough and Sun 1995) REE patterns for Karowe peridotitic garnet inclusions. **a:** Sinusoidal REE_N patterns for harzburgitic garnets. **b:** Two harzburgitic garnets with fairly flat and slightly U-shaped REE_N patterns and a single lherzolitic garnet, showing a normal REE_N pattern -----59

Fig. 3.8 Chondrite normalized (McDonough and Sun 1995) REE patterns of low- and high-Ca majoritic garnets from Karowe compared to majoritic garnets from Monastery (Moore et al. 1991) and Jagersfontein (Tappert et al. 2005) -----60

Fig. 3.9 Geothermobarometry results for two non-touching garnet-orthopyroxene pairs calculated using the barometer of Brey & Köhler (1990) barometer combined with thermometer of Harley (1984). Model geotherms for 38-41 mW/m² surface heat flow after Hasterok and Chapman (2011), graphite-diamond transition (G/D) from Day (2012). A 40 mW/m² Cretaceous paleo-geotherm was derived from mantle xenoliths at Letlhakane (Stiefenhofer et al. 1997) and agrees well with the 39-40 mW/m² geotherm indicated by Karowe peridotitic inclusions -----62

Fig. 3.10 a: Al+Cr versus Si as atoms per formula unit (apfu, with [O]=24) in majoritic garnet inclusions from Karowe and worldwide sources (n=69; database of Stachel and Harris 2008). Red

dashed line indicates threshold value of > 6.12 apfu Si used to define majoritic garnets. **b**: Si apfu plotted against pressure (GPa), calculated using the barometer of Beyer and Frost (2017) -----64

Fig. 3.11 Cr_2O_3 vs CaO diagram for garnets inclusions in diamonds from Karowe ($n=31$) and nearby localities (Deines and Harris, 2004; Deines et al.2009; Stachel et al.2004b). Isobars are from Grütter et al. (2006) -----66

Fig. 3.12 The relationship between (a) Sr^* and Eu/Eu^* and (b) between $\sum\text{HREE}$ (Tb-Lu) and Ti in eclogitic whole rock compositions reconstructed from Karowe inclusions and calculated whole rocks of gabbroic eclogite xenoliths from Orapa (Aulbach et al.2017). The HREE concentrations of N-MORB after 20% melt extraction, calculated assuming a modal clinopyroxene-garnet ratio of 1:1 are from Stachel et al. (2004a), Ti was calculated using partition coefficients from Klemme et al (2002). Sr^* is $\text{Sr}_N/(0.5 \times \text{Pr}_N + 0.5 \times \text{Nd}_N)$ and Eu/Eu^* is $\text{Eu}_N/\text{SQRT}(\text{Sm}_N \times \text{Gd}_N)$ -----67

Fig. 3.13 Y versus Zr for harzburgitic and lherzolitic garnet inclusions from Karowe and from Orapa (Stachel et al. 2004b). Main compositional fields and trends shown are for garnet xenocrysts from Griffin and Ryan (1995) -----70

Fig. 4.0 Some of the surface features on octahedral crystal faces of Karowe diamonds: (a) serrate laminae, (b) shield-shape laminae, (c) shield-shape laminae and pyramidal trigons as well as flat-bottomed negative trigons (d) stacked octahedral growth layers pattern, and (e,f) due to resorption intermediate patterns are formed, causing the development of a unique surface texture transitional between terraces and hillocks -----82

Fig. 4.1 Pie chart showing the relative proportions of diamond habits among Karowe diamonds-----82

Fig. 4.2 Histograms comparing the nitrogen content in diamonds from Karowe (a) and the Orapa kimberlite cluster (b); Karowe eclogitic (c) and peridotitic (d) diamonds are also shown separately (c, d). Data for diamonds from the Orapa kimberlite cluster are from Deines et al. (1993), Deines and Harris (2004) and Deines et al. (2009) -----84

Fig. 4.3. Total nitrogen concentration (at.ppm) versus relative percentage of nitrogen in B centers for Karowe inclusion-bearing diamond fragments. Isotherms shown are calculated for mantle residence times of 1 and 3 Ga after Leahy and Taylor (1997) -----85

Fig. 4.4 Histogram showing calculated platelet diameters (Speich et al. 2017) for Karowe diamonds -----86

Fig. 4.5 a) The relationship between integrated platelet peak area $[I(B^*)]$ and absorption due to nitrogen B-centers (μ_B). The kernel density estimation (KDE) and the reference line defining regular behaviour are from Speich et al. (2018). Also shown is the regularity trend of Woods (1986)

Samples plotting to the right of these lines are considered “irregular” and experienced platelet degradation. b) The relationship between platelet peak area and the position of platelet peak ----89

Fig. 4.6 Histograms comparing the carbon isotope compositions of diamonds from Karowe and other Orapa cluster kimberlites (a, b). Data for diamonds from the Orapa kimberlite cluster are from Deines et al. (1993), Deines and Harris (2004) and Deines et al. (2009) -----90

Fig. 4.7 Cumulative probability plot (Ludwig 2003) showing the main modes for peridotitic and eclogitic diamonds from Karowe -----91

Fig. 4.8 Co-variations between nitrogen content and carbon isotopic composition (both measured via SIMS) of Karowe diamonds. The dotted line represents the limit sector curve of Cartigny et al. (2001) -----91

Fig. 4.9 Examples of the internal growth structures of Karowe diamonds as seen in CL images, together with locations of SIMS analyses. The corresponding data are given in the tables below the figures. Left: Diamond KW8 shows nearly planar octahedral growth that appears to be resorbed on the right before being overgrown by the poorly luminescent layers containing spots 7 (likely equivalent to the layer with spot 6) and 8. Spot 5 marks the arrival of a new pulse of fluid with lower $\delta^{13}\text{C}$ and higher N content. Right: Diamond KW24 shows a jump from strongly ^{13}C depleted low nitrogen growth to mantle-like $\delta^{13}\text{C}$ and high nitrogen. Whilst in the CL image the main discontinuity seems to occur between the growth phases containing points 5 and 6, compositionally point 5 actually is already part of the mantle-like growth phase -----92

Fig. 4.10 Histograms showing calculated mantle residence temperatures for diamonds from Karowe (top) and worldwide (bottom) assuming mantle residence for a period of 1 Ga for eclogitic diamonds (a) and 3 Ga for peridotitic diamonds (b). Diamonds containing majoritic garnets are shown in black -----98

Fig. 4.11 Comparison of platelet degradation temperature (T_p) and nitrogen aggregation temperature (T_N) assuming 1 Ga mantle residence. Solid line indicates a 1:1 correlation and dashed lines indicate $\pm 50^\circ\text{C}$ error -----100

List of Abbreviations and Symbols

apfu	Atoms per formula unit
at.ppm	Atomic parts per million
%B	Percentage of nitrogen in B centres in a diamond
~	Approximately
×	Times
σ	Sigma or one standard deviation of the mean
$\delta^{13}\text{C}$	Carbon isotope composition relative to the international VPDB standard
CCIM	Canadian Centre for Isotopic Microanalysis
CHO fluids	Acronym for Carbon-Hydrogen-Oxygen fluids
CL	Cathodoluminescence
Ca#	Molar calcium number calculated as $[100 \times \text{Ca} / (\text{Ca} + \text{Mg} + \text{Fe})]$
Cr#	Molar chromium number calculated as $[100 \times \text{Cr} / (\text{Cr} + \text{Al})]$
EDS	Energy dispersive spectrometer
E/Eu*	Europium anomaly calculated geometrically as $\text{Eu}^* = \text{Eu}_N / [0.5\text{Gd}_N + 0.5\text{Sm}_N]$
EPMA	Electron probe micro analyser
FTIR	Fourier transform infrared
Ga	Giga-annum (billion years = 1×10^9)
GPa	Gigapascal
G/D	Graphite-diamond transition
G4	Class of mantle-derived eclogitic / pyroxenitic garnets
G9	Class of mantle-derived lherzolitic garnets
Hz	Herzt (pulses per second)
LA-ICP-MS	Laser-ablation inductively coupled plasma mass spectrometer
M/ Δ M	Mass resolution mode

Ma	Miga-annum (million years= 1×10^6)
MARID	Mica-Amphibole-Rutile-Ilmenite-Diopside assemblage
MC-SIMS	Multi-collector secondary ion mass spectrometer
Mg#	Molar magnesium number calculated as $[100 \times \text{Mg} / (\text{Mg} + \text{Fe})]$
N-MORB	Normal-mid-ocean ridge basalt
PIC	Phlogopite-ilmenite-clinopyroxene
ppm	Parts per million
P-T	Pressure and temperature
REE	Rare earth element
LREE	Light rare earth element
MREE	Middle rare earth element
HREE	Heavy rare earth element
QUIDDIT	Quantification of Infrared-active Defects in Diamonds and Inferred Temperatures
VPDB	Vienna-Pee-Dee-belemnite

Table of contents

Abstract	ii
Preface.....	v
Acknowledgements.....	vii
List of Tables	viii
List of figures.....	ix
List of Abbreviations and Symbols.....	xiv
Chapter One	1
1.0 Introduction.....	1
1.1 Kimberlite hosted xenoliths	1
1.2 Diamond host rocks	2
1.3 Diamond formation.....	4
1.4 Diamonds in Botswana	5
Chapter Two	8
2.0 The compositional structure and thermal state of the lithospheric mantle beneath Karowe Mine, north-eastern Botswana	8
2.1 Introduction.....	8
2.1.1 Geological setting	9
2.1.2 Host Kimberlite and Samples	11
2.3 Analytical Methods.....	11
2.4 Petrography.....	12
2.5 Results.....	13
2.5.1 Major element compositions of the minerals.....	18
2.5.2 REE and trace element compositions of clinopyroxenes and garnets	22
2.5.3 Geothermobarometry	24
2.6 Discussion.....	32
2.6.1 Comparison of xenoliths with inclusions in diamonds from Karowe.....	32
2.6.2 Equilibration conditions and textural relationships	33
2.6.3 The Cretaceous mantle geotherm beneath Karowe and mantle sampling	34
2.6.4 Evidence for partial melting and metasomatic modification	35
Chapter Three	41

3.0 Mineral inclusions in diamonds from Karowe Mine, Botswana: super-deep sources for super-sized diamonds?	41
3.1 Introduction.....	41
3.1.1 Previous work in the Orapa cluster and Zimbabwe Craton	41
3.2 Samples and analytical techniques.....	42
3.3 Results.....	44
3.3.1 Major element compositions of inclusions and paragenetic associations.....	46
3.3.1.1 Eclogitic suite.....	46
3.3.1.2 Peridotitic suite	50
3.3.1.3 Websteritic suite.....	53
3.3.1.4 Sublithospheric inclusions	53
3.3.2 REE and trace element compositions of the inclusions	53
3.3.2.1 Eclogitic suite.....	54
3.3.2.2 Peridotitic Suite.....	57
3.3.2.3 Sublithospheric inclusions	58
3.4.3 Geothermobarometry	59
3.4 Discussion.....	63
3.4.1 Origin and evolution of eclogitic and websteritic diamond substrates	64
3.4.2 Peridotitic diamond substrates in the lithospheric mantle beneath Karowe	67
3.4.3 Sublithospheric substrates.....	69
3.5 Conclusions.....	71
Chapter Four	73
4.0 Physical characteristics, nitrogen content and carbon isotope composition of diamonds from the Karowe Mine in Botswana.....	73
4.1 Introduction.....	73
4.1.1 Geological context	74
4.2 Samples and Analytical Methods.....	75
4.2.1 Fourier transform infrared (FTIR) spectroscopy	75
4.2.2 Cathodoluminescence (CL) imaging and secondary ion mass spectrometry (SIMS) .	76
4.3 Results.....	78
4.3.1 Physical characteristics	78

4.3.2 Nitrogen contents and nitrogen aggregation states	81
4.3.3 Platelet defects and hydrogen-related absorption peaks	84
4.3.4 Carbon isotope composition	88
4.4 Discussion	92
4.4.1 Diamond characteristics in comparison with those from the Orapa cluster	92
4.4.2 Diamond-forming fluids and carbon sources.....	93
4.4.3 Nitrogen thermometry.....	95
4.4.4 Platelet behaviour and platelet degradation thermochronometry	98
4.5 Conclusion	99
Chapter Five	101
5.0 Summary of the main findings.....	101
5.1 The lithospheric mantle beneath Karowe mine	101
5.2 Paragenetic origins of Karowe diamonds	102
5.3 Diamond characteristics.....	103
6.0 Future work and considerations	104
References.....	105
Appendix A-Geochemical data for Karowe xenoliths and xenocrysts	127
Appendix B-Geochemical data for mineral inclusions in Karowe diamonds.....	129
Appendix C- Physical characteristics, FTIR and SIMS data for Karowe diamonds	129

Chapter One

1.0 Introduction

1.1 Kimberlite hosted xenoliths

Mantle xenoliths and xenocrysts provide valuable information about the nature of the lithospheric mantle underlying particular regions, because they record chemical fingerprints from which their depth of origin and thermal state at the time of kimberlite eruption can be determined (Boyd and Gurney 1986; Griffin et al. 2003; Pearson et al. 2003). They are usually small often fragmented and may differ significantly in their petrographic and chemical constituents (Pearson et al. 2003). Dawson (1980) grouped xenoliths broadly into five divisions or suites: peridotite-pyroxenites, metasomatised peridotites (rich in amphibole and/or phlogopite), glimmerites and MARID (mica-amphibole-rutile-ilmenite-diopside), eclogites and megacrysts. The pressure-temperature estimates constraining the formations of these rocks and minerals are deduced from equilibration of individual minerals or assemblages using published geothermobarometers. The most common suite is coarse-grained Mg-rich, low-temperature garnet-bearing peridotite, while the abundances of other xenolith types vary between kimberlites (Dawson 1980; Pearson et al. 2003). Metasomatised peridotites are characterised by the development of new mineral species (e.g., phlogopite, rutile, K-richterite amphibole) or changes in the chemistry of pre-existing phases as a consequence of the infiltration of metasomatic fluids/melts prior to kimberlite eruption (Harte 1983; Erlank et al. 1987; Winterburn et al. 1990). Within the glimmerites and MARID-suite xenoliths, rocks are mainly dominated by phlogopite, where glimmerites usually contain more phlogopite (>90 %). Grégoire et al. (2002) subdivided this group into a PIC (phlogopite-ilmenite-clinopyroxene) suite related to Group I kimberlite (basaltic) magma and a MARID (mica-amphibole-rutile-ilmenite-diopside) suite linked to Group II kimberlite (micaceous) magma.

Eclogites are the high pressure metamorphic equivalent of basalts/gabbros. Based on textural (McGregor and Carter 1970) and chemical variations of garnet and clinopyroxene minerals (McCandless and Gurney 1989), eclogites classify as Group I (often diamondiferous) and Group II (non-diamondiferous). Diamondiferous eclogites contain sodium-rich garnets and potassium-rich clinopyroxenes and tend to yield higher estimated temperatures than non-diamondiferous eclogites (Robinson et al. 1984; McCandless and Gurney 1989). Megacrysts are a suite of single crystals or monomineralic polycrystalline aggregates measuring 1-15 cm in the longest dimension (Boyd et al. 1984). The most common mineral phases are orthopyroxene, clinopyroxene, garnet, olivine and ilmenite, while phlogopite and zircon are rare. They can be divided into Cr-poor and Cr-rich suites, based on the Cr contents of their minerals (Moore and Belousova 2005).

1.2 Diamond host rocks

Diamond source rocks in the subcratonic lithospheric mantle can be defined by common minerals trapped in diamonds. The two principal mineral inclusion suites are peridotitic and eclogitic, with distinct mineral assemblages and geochemical compositions (Meyer and Boyd 1972). The peridotitic suite is further subdivided into harzburgitic and lherzolitic. A third websteritic suite has also been recognised, which is chemically intermediate between peridotitic and eclogitic (Deines et al. 1993; Stachel and Harris 2008). Irrespective of paragenesis, mineral inclusions in diamonds can be classified into three types: protogenetic, syngenetic, and epigenetic (Harris 1968; Meyer 1987). Protogenetic inclusions formed earlier than the diamond and subsequently become incorporated during diamond growth, whilst syngenetic inclusions crystallised at the same time as their host diamond. Epigenetic inclusions result from later infiltration of fluids or melts into the diamond along cracks, making pseudomorphs of the primary inclusions. The majority of inclusion studies assume a syngenetic origin for these mineral inclusions because inclusions invariably have

a shape that can be shown to be imposed by the diamond (Harris 1968; Prinz et al. 1975; Meyer 1987; Stachel and Harris 1997; Pearson and Shirey 1999). However, these assumptions were recently challenged by Bruno et al. (2014) and Nestola et al. (2014), based on crystal morphology and the crystallographic orientations of olivine inclusions with diamond-imposed morphology. They argued that a diamond morphology may be imposed to a full-grown olivine (protogenetic) during their encapsulation. Therefore, the morphology alone cannot be considered as proof of syngensis. In addition, Nestola et al. (2017) further demonstrated that mineral inclusions in diamonds can have the same age as the diamonds in that they become enclosed in and isolated from any further isotopic exchange, suggesting synchronous rather than syngenetic trapping.

Reviewed major- and trace-element compositions of peridotitic mineral inclusions in diamonds indicate that the diamond substrate had a protolith derived during polybaric melt extraction proceeding from the garnet facies into the spinel stability fields (i.e., protolith depletion occurred in Archean mid-oceanic ridge environments; Stachel and Harris 2008). The eclogitic mineral inclusions reflect a substrate showing an evolutionary trend typical of subducted basaltic protoliths which originated during high degrees of partial melting at Archean or early Proterozoic spreading centres or that the rocks experienced secondary melt depletion during subduction or after emplacement in the subcratonic lithosphere (Stachel and Harris 2008). The websteritic suite reflects a broad range of pyroxenitic source rocks, which are transitional between peridotitic and eclogitic rocks. The results of geothermobarometric calculations on published data of mineral inclusions in diamonds from around the world indicate that the dominant harzburgitic paragenesis generally formed predominately under subsolidus conditions while most diamonds of lherzolitic and eclogitic paragenesis precipitated in the presence of melts, unless their formation is related to strongly reducing fluids (CH₄-rich) that increase the solidus temperatures (Stachel and Luth 2015).

In recent years a number of studies revealed that diamond formation may also be associated with craton margin settings or lithosphere that experience post-Archean tectonothermal events (Stachel and Harris 2008; Shirey et al. 2013). In addition, there are some studies that show evidence of diamond formation in the sublithospheric mantle at a depth range between 300 and 800 km, i.e., in the lower asthenosphere, the transition zone and the lower mantle (Harte, 2010). For the lower asthenosphere (<410 km) and transition zone (410 to 660 km), the inclusions are predominantly majoritic garnets (with or without clinopyroxene) which indicate bulk compositions of eclogitic/metabasic affinity (Kiseeva et al. 2013). From the upper mantle to lower mantle (>660 km), the dominant phases include ferropericlase, Ca-Si and Mg-Si perovskites and are mostly associated with metaperidotitic bulk compositions.

1.3 Diamond formation

Diamonds form and grow from melts/fluids (Navon et al. 1988; Stachel and Harris 2009; Wiggers-de Vries et al. 2013a; Stachel and Luth 2015). Diamond formation in Earth's mantle is dominated by two main reaction mechanisms, reduction of carbonates (Eggler and Baker 1982) or oxidation of methane introduced to the diamond substrates through infiltration melts and fluids (Taylor and Green 1989). Stachel and Luth (2015) introduced a new concept of diamond precipitation that does not involve redox reactions between diamond source rocks and infiltrating fluids but is based on isochemical cooling or combined cooling and depressurisation of ascending CHO fluids (dominated by CH₄, CO₂, and H₂O). At moment, the exact roles in diamond formation played by the release of fluids/melts from subducting oceanic crust, mantle metasomatism, redox state of the lithospheric mantle and carbon speciation in the ascending fluids are still debated (Wiggers-de Vries et al. 2013a; Shirey et al., 2013; Stachel and Luth 2015; Weiss et al. 2015). For example, do these mechanisms produce fluids by a common mechanism or do specific processes operate for

different diamond populations (suites and parageneses)? However, it has been found that subducted oceanic slabs played a major role during Proterozoic diamond formation beneath the Siberian Craton (Wiggers-de Vries et al. 2013b), while a combination of subduction and mantle metasomatism were reported as the main source of fluids for non-gem diamonds formed in the Northwest Territories, Canada (Weiss et al. 2015). Stachel and Luth (2015) confirmed that oxygen fugacity plays a critical role in determining the mode of diamond formation in peridotitic source rocks but in the absence of a suitable oxybarometer they could not quantitatively apply the same model to cratonic eclogites.

1.4 Diamonds in Botswana

Botswana is the world's largest producer of diamonds by value, with the bulk of the production being obtained from mines at Jwaneng and Orapa. The revenue generated from the sales of these diamonds continues to have great impact on the economy of the country. With the new mine at Karowe, a further opportunity arises to assess how diamonds form in this northern region of Botswana. The Karowe mine is located within the Orapa kimberlite cluster, less than 30 km from the main Orapa mine, both being on the western edge of the Zimbabwe Craton (Fig.1.1). Large diamonds continue to be recovered from the mine (up to 330 carats), which fuel the interest in understanding diamond formation in this area. Mantle xenoliths, diamonds and their inclusions will be the three main sample types from the Karowe mine that will be used in this study to provide a better understanding of the diamond-forming conditions and nature of fluids responsible for diamond crystallisation. The results of this work are expected to answer the principal question of how diamonds formed within the diamondiferous root beneath north-eastern part of Botswana? Such information will hopefully improve exploration models and thereby lead to an extension of

the lifespan of diamond mining operations in Botswana through the discovery of additional deposits.

This thesis aims to address the followings questions:

1. What is the compositional structure and thermal state of the lithospheric mantle beneath the western edge of Zimbabwe Craton (both at the time of diamond formation and at the time of Cretaceous kimberlite eruption)? This question is addressed in **Chapter Two** which examines the chemical and physical environment of diamond formation and residence beneath Karowe.
2. What are the common mineral inclusions in Karowe diamonds and their associated parageneses? **Chapter Three** links Karowe diamonds to specific lithologies in the lithospheric mantle.
3. What is the composition of diamond-forming fluids and how do different fluids affect the growth history of Karowe diamonds? **Chapter Four** addresses this question to reveal specific conditions suitable for the formation of high value diamonds.
4. Is there a link between diamond-forming carbon species and subducted oceanic crust? This question is addressed by combining new data obtained from the mineral inclusions (chapter three) and diamonds (chapter four) studies. Therefore, contributing to the longstanding discussion about the role of subducted carbon in the formation of diamonds.
5. Are the results obtained in this study comparable to those obtained in other diamond deposits in Botswana, southern Africa and worldwide? Putting the entire obtained data set into the context of other studies on diamonds and mantle xenolith from around the globe

will reveal any peculiarities associated with the Karowe Mine and its unusually coarse diamond population.

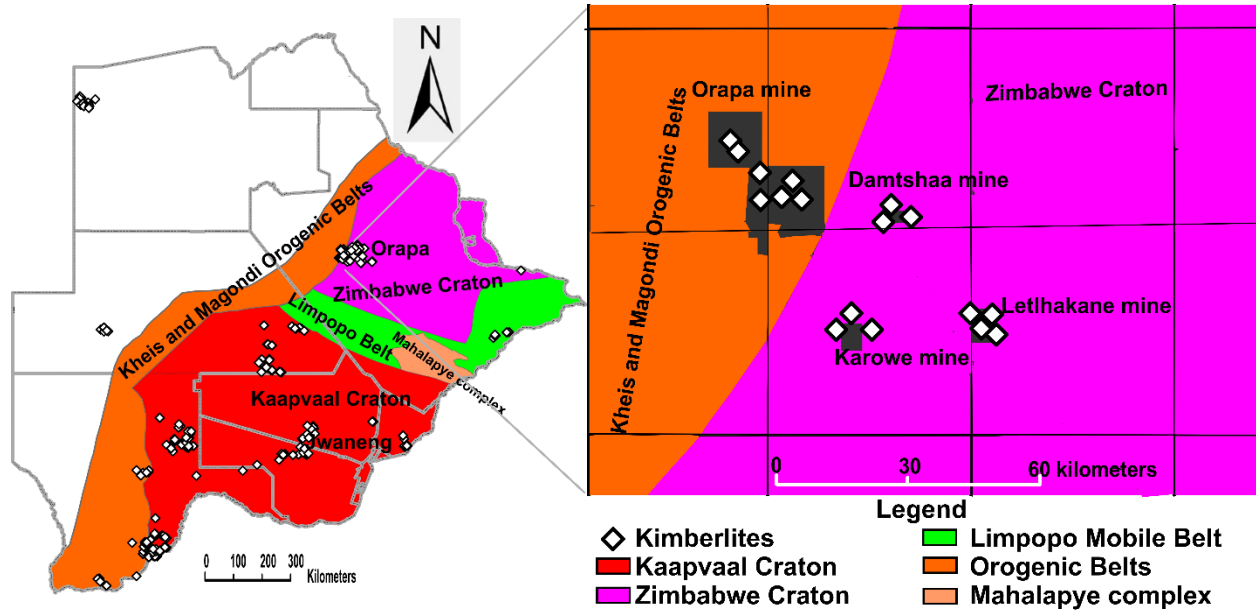


Fig.1.1 Map of Botswana showing the location of the Karowe mine within the Orapa cluster (map modified after Brook 2012). Also shown for reference are the main tectonic units of the Kalahari Super-Craton from Key and Ayres (2000)

Chapter Two

2.0 The compositional structure and thermal state of the lithospheric mantle beneath Karowe Mine, north-eastern Botswana

2.1 Introduction

The recent development of the Karowe diamond mine by Lucara Diamond Corporation in north-eastern Botswana provides an opportunity to examine the compositional structure and thermal state of the lithospheric mantle beneath the western edge of the Zimbabwe Craton. Karowe, formerly known as the AK6 kimberlite, is an open pit mine located approximately 25 km south of Orapa mine and 23 km west of Letlhakane mine. All three mines form part of the Cretaceous (~93 Ma; Davis 1977) Orapa kimberlite cluster. The Orapa and Letlhakane kimberlite bodies have been mined extensively for the past three decades, yielding a wide range of mantle xenolith suites (Shee and Gurney 1979; Stiefenhofer et al. 1997; Meulemans et al. 2012; Aulbach et al. 2017). In contrast, the Karowe kimberlites have only recently been mined and little is known about their mantle xenoliths. The observation of sublithospheric inclusions (three majorite garnets) in Karowe diamonds (Motsamai et al. 2018) indicates that the mantle underlying Karowe might be different from that of Orapa and Letlhakane in terms of diamond formation or Karowe kimberlites sampled a deeper part of the mantle. The depth of formation of sublithospheric inclusions were estimated to be between 330 to 420 km, straddling the asthenosphere–transition zone boundary. Sublithospheric inclusions across the Orapa kimberlite cluster have only been reported in Karowe so far. Therefore, in the current study we examine (1) if the Karowe mantle xenolith suite derives from the shallow or deep lithospheric mantle, (2) the degree of melt depletion and metasomatic modification, and (3) the degree to which mantle xenoliths fit into the regional thermal structure of the lithospheric mantle as established from Letlhakane xenoliths. Petrographic observations

from 24 mantle xenoliths, major and trace element compositions of individual minerals, as well as a geotherm at the time of kimberlite eruption will be presented in order to characterise the nature and composition of the mantle section sampled by the Karowe kimberlites.

2.1.1 Geological setting

The geology of Botswana is mainly defined by the domains of the Kalahari Super-Craton, which include the Archean basement of the Kaapvaal and Zimbabwe cratons sutured by the Archean to Paleoproterozoic Limpopo Mobile Belt (see Fig. 1.1). The Kaapvaal Craton forms the dominant structure of the Kalahari Super-Craton. The craton nucleated first and stabilised between 3.7 Ga to 2.6 Ga (De Wit et al. 1992) while the formation of the core and crustal growth of the Zimbabwe Craton occurred between 3.5 Ga to 2.6 Ga (Horstwood et al. 1999; Rollinson and Whitehouse 2011). The collision of the Kaapvaal and Zimbabwe cratons at about 2.7 to 2.6 Ga resulted in the formation of the Limpopo Mobile Belt (Van Reenen et al. 1987). In the west, the Kalahari Super-Craton is bounded by the 1.8 to 2.0 Ga Kheis and Magondi orogenic belts (Majaule et al. 2001; Treloar 1988)

The Orapa and Letlhakane kimberlites are emplaced into the Proterozoic Magondi Belt which bounds the western part of the Zimbabwe Craton. For the Orapa kimberlites, Shee and Gurney (1979) reported predominantly eclogitic xenoliths, but a more recent study of xenoliths based on samples from kimberlite drill core found a range of peridotitic xenoliths, comprising garnet and spinel-bearing peridotites and a minor proportion of eclogitic xenoliths (Meulemans et al. 2012). In the Letlhakane kimberlites, a wide range of xenoliths was documented by Stiefenhofer et al. (1997) including peridotites, eclogites, pyroxenites, megacrysts, glimmerites and MARID (mica-amphibole-rutile-ilmenite-diopside) assemblages. Based on these studies, it was established

that both Orapa and Letlhakane kimberlites sampled similar sections of lithospheric mantle belonging to the western edge of Zimbabwe Craton (Stiefenhofer et al. 1997), rather than the lithospheric mantle of the Proterozoic Magondi Belt intruded by these kimberlites at surface. This conclusion is consistent with findings of a magnetotelluric study of this region where the resistivity imaging shows lithosphere extending to approximately 220km depth (Miensopust et al. 2011).

Letlhakane peridotite xenoliths contain evidence of modal metasomatism recorded by enrichments in phlogopite, clinopyroxene, and Cr-spinel as well as cryptic metasomatic imprints (van Achterbergh et al. 2001). Xenoliths were also dated using the Re-Os isotopic system by Carlson et al. (1999) and Luguet et al. (2015) documenting Neoproterozoic mantle root formation ages. Numerous studies have found that the Orapa eclogite suite classifies into two groups based on textural and chemical variations of garnet and clinopyroxene minerals, i.e., often diamondiferous group I eclogites and diamond-free group II eclogites (Shee and Gurney 1979, Robinson et al. 1984, Viljoen et al. 1996). Based on the geothermobarometric data from Aulbach et al. (2017), both eclogite groups and the pyroxenite suite coexist over a calculated pressure interval of 3.2 to 4.9 GPa (along a geothermal gradient of 40 mW/m²). This overlap was interpreted as a reflection of late heating and/or decompression during lithosphere stretching and magmatism prior to kimberlite emplacement.

Apart from mantle samples from the Orapa kimberlite cluster, the lithospheric mantle below the Zimbabwe Craton has been studied via mantle xenoliths and inclusion-bearing diamonds from Cambrian kimberlites that comprise the Murowa-Sese cluster, located in the southern part of the craton. There, Smith et al. (2009) reported that the lithospheric mantle beneath the southern Zimbabwe Craton is extremely depleted with diamond substrates of harzburgitic-dunitic paragenesis. The region is underlain by ultradepleted chromite-harzburgites and chromite-dunites

of dominantly Neoproterozoic age (Pearson et al., in press) though older ages are recorded by some peridotitic sulphide inclusions in diamonds (Smith et al. 2009).

2.1.2 Host Kimberlite and Samples

The Orapa kimberlite cluster consists of more than 81 known kimberlite bodies (Brook 2012), of which four are currently active diamond mines: Orapa, Letlhakane, Damtshaa and Karowe. Kimberlites were emplaced during the Cretaceous period (Davis 1977) into sedimentary rocks of the Karoo Supergroup (Hanson et al. 2009). The Karowe mine consists of three pipes (North, Central, and South) coalescing near surface. The overall surface area of the combined kimberlite body is approximately 3.3 ha and expands to 7 ha at 120 m depth (Lynn et al. 2014).

The 24 mantle xenoliths and 106 clinopyroxene xenocrysts examined here were sampled randomly from the three pipes at the Karowe mine via mining processes. Mantle xenoliths have ellipsoidal shapes and measure 1.5 to 4.0 cm along the longest dimension. The size range of clinopyroxene xenocrysts varies from 1.0 mm to 4.0 mm.

2.3 Analytical Methods

Major- and minor-element compositions of xenolith mineral grains and clinopyroxene xenocrysts were analysed using a JEOL 8900R electron probe micro-analyser (EPMA). All elements were measured with an accelerating voltage of 20 kV, beam current of 20 nA and $\leq 2 \mu\text{m}$ beam diameter. The typical total background counting times were 30 to 60 seconds equals the on-peak counting times. Elements were acquired using the following analysing crystals: LIFH for Fe-K α , Mn-K α , Ni-K α , TAP for Na-K α , Si-K α , Mg-K α , Al-K α , PET for K-K α , Ti-K α , Cr-K α and PETH for P-K α and Ca-K α . A range of mineral and synthetic reference materials used for calibration are in Table

A1 (see Appendix A). The CITZAF procedure of Armstrong (1995) was used for data reduction. For xenoliths, two to five grains were analysed per mineral (olivine, clinopyroxene, orthopyroxene, garnet, and spinel). In each grain, two to three spots were analysed, checked for homogeneity, and averaged after removal of outliers (e.g., low total sum of oxides). Accuracy of analyses was monitored using reference materials of similar composition. Detection limits typically are ≤ 0.02 wt% oxide.

Trace element concentrations for garnet and clinopyroxene in ten selected samples were measured using a Resonetics M-50 193 nm excimer laser coupled with a Thermo Element XR 2 sector-field inductively coupled plasma mass spectrometer (LA-ICP-MS). Mineral grains were ablated with a spot size of 130 μm at a laser frequency of 10 Hz and energy density of ~ 4 J/cm². For each mineral grain two or three spots were analysed. An average of 100 sweeps through the mass spectrum were made for each analysis. Measurement time comprised 40 seconds of background collection followed by 50 seconds of sample ablation. The ICP-MS was operated at low mass resolution mode ($M/\Delta M = \text{ca. } 300$). The ThO/Th signal was monitored to ensure that oxide production remained below 0.5 %. Calibration of relative element sensitivities was performed using the NIST SRM 612 glass reference material and ⁴³Ca (determined by EPMA) was employed as internal standard to normalise the signal intensities. Data processing was performed offline using Iolite v3 (Paton et al. 2011). Detection limits are ≤ 30 ppb for REE, Nb, Zr, Y, Sr, and ~ 1 ppm for Ti and Ni.

2.4 Petrography

Mineral proportions, texture, as well as shape and size of mineral grains were determined via petrographic examination of thin sections using a petrographic microscope. Thin sections were

scanned using a Nikon Super Coolsan 5000 ED. Scanned images were visualised in JMicroVision application software to estimate minerals modes (Roduite 2017). Uncertainties in modal abundances are associated with the coarse-grained nature and small size of the samples (average ~4.0 cm). Approximately 250 to 450 individual grains were counted per thin section. Based on the mineralogy, the xenoliths samples were classified into five groups; garnet-free spinel lherzolite, garnet-spinel lherzolite, garnet peridotite, pyroxenite/eclogite and olivine megacryst.

2.5 Results

From a total of 24 mantle xenoliths, 14 samples are classified as spinel lherzolites. They are texturally bi-modal containing both coarse (average >3 mm) and granuloblastic textures as classified using the nomenclature of Harte (1977). The samples are fresh and only show minor alteration along veins. Most olivines are large and fractured, with an average size range between 0.60 and 3.80 mm. They occasionally show undulatory extinction, but no evidence of neoblast formation was observed. Olivine grains (55 - 81 % modal abundance; see Table A2 in Appendix A) are anhedral and appear to be well-equilibrated with grain boundaries intersecting at nearly 120° triple junctions. Clinopyroxene ranges between 10 and 21 % in modal abundance. The grains are subhedral to euhedral measuring 0.4 to 3.5 mm in size. Coarse-grained sample AK6-03 contains clinopyroxene grains with exsolution lamellae. Orthopyroxene ranges from 6 to 21 % in modal abundance, grains are mostly tabular and subhedral (<4.0 mm along the longest dimension). Large orthopyroxenes are closely associated with spinel grains and contain exsolution lamellae of

clinopyroxene.

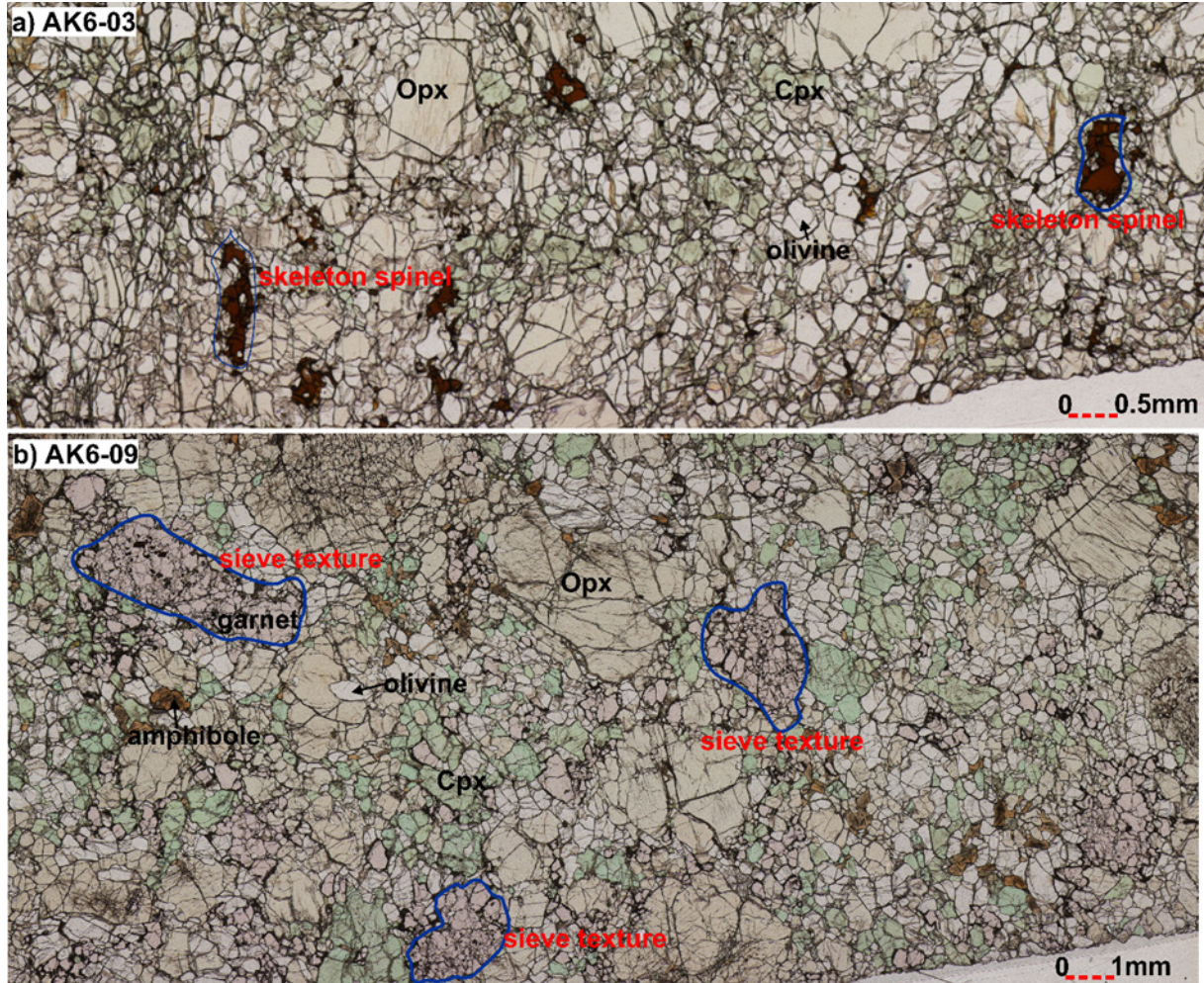


Fig. 2.0 Photomicrographs showing a) irregular shaped spinel and b) the textural relationship of spinel and garnet in the garnet-spinel lherzolite suite. In xenolith AK6-03 (a), spinels have a ‘skeletal’ appearance. In sample AK6-09 (b) numerous small spinel inclusions in garnets create a ‘sieve’ texture

Spinel occurs as irregular crystals, generally of skeletal shape and intergrown with orthopyroxenes (e.g., AK6-03 in Fig 2.0). They are mostly small (~0.2 mm) with few large crystals (up to 3.2 mm). Spinel constitutes 2 to 7 % in modal abundance, which is more abundant than in previously-described spinel facies peridotites (mean: 1.1%, median: 0.8 %; Pearson et al. 2003).

Four xenoliths classify as garnet-spinel lherzolite based on coexistence of garnet and spinel within the same sample. They have textures ranging from coarse-grained to granuloblastic

and consist of 49 to 70 % olivine, 14 to 33 % clinopyroxene, up to 11 % orthopyroxene, and 2 to 9 % garnet. Spinel modes are less than 3 %. Grain sizes for olivines, clinopyroxenes, and orthopyroxenes are approximately the same as those of the spinel lherzolite suite. Two samples have garnets intergrown as symplectites in distinct forms with spinels (e.g., “sieve” texture in sample AK6-09; Fig. 2.0). No spinel-orthopyroxene symplectite textures were observed in these xenoliths. The remaining samples have garnet with kelyphite rims. Sample AK6-18 also contains phlogopite and amphibole.

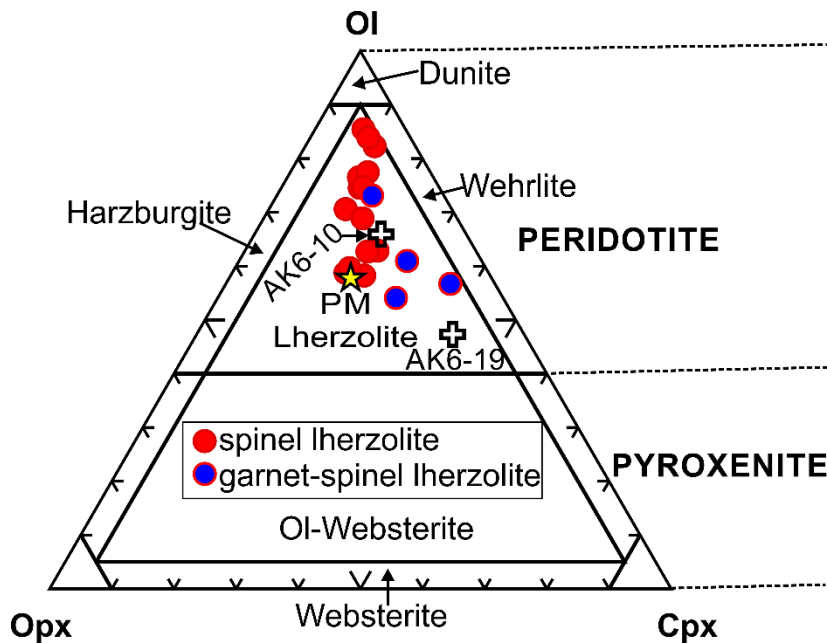


Fig. 2.1 Triangular diagram for the classification of ultrabasic rocks based on the proportions of olivine (ol), orthopyroxene (opx) and clinopyroxene (cpx) after Streckeisen (1976), showing garnet peridotites (AK6-10 and AK6-19) and spinel peridotites from Karowe. The other two garnet pyroxenites are not shown because they contain only clinopyroxene and garnet. Primitive Mantle (PM) for spinel facies (McDonough and Rudnick 1998)

The two granuloblastic samples described here consist of a garnet lherzolite (AK6-10) and a olivine-bearing garnet websterite (AK6-19). From the modal proportions of olivine (ol), orthopyroxene (opx), and clinopyroxene (cpx) normalized to 100% (Streckeisen 1976), the garnet websterite sample plots into the lherzolite field (Fig. 2.1). Further classification based on the

chemistry of garnet will however be carried out in the next section. In this sample, olivine occurs as small anhedral crystals ≤ 1.2 mm in size with a modal abundance of 39 %. The modal abundance of clinopyroxene and garnet is 34 and 17 %, respectively. Garnet in sample AK6-10 occurs as irregular, fractured, and rounded crystals (up to 1.0 mm in diameter) and constitutes up to 15 % in modal assemblage. The sample contains euhedral reddish-brown pleochroic phlogopite (~5.0 vol%). Phlogopite has been invoked as evidence for modal metasomatism in Letlhakane xenoliths (van Achterbergh et al. 2001). Clinopyroxene accounts for up to 22 % of the mode of the sample and commonly displays fine exsolution lamellae of orthopyroxene.

Three coarse-granuloblastic textured samples documented here are two garnet-clinopyroxenites and one eclogite (AK6-25). Both garnet clinopyroxenites display exsolution features in their clinopyroxenes (thin lamellae parallel to [100]), with the exsolution lamellae in sample AK6-15 being particularly prominent (Fig. 2.2a). The same specimen also contains chlorite. Phlogopite is present in the garnet clinopyroxenites but absent in the eclogite. Only one eclogite xenolith was found, despite a predominance of eclogitic inclusions in Karowe diamonds (Motsamai et al. 2018). The single coarse-grained eclogite (AK6-25) documented here, contains large fractured garnet grains (up to 6.0 mm) interlocking with altered clinopyroxenes (Fig. 2 2b). Texturally, the xenolith represents a Group II eclogite in the classification of MacGregor and Carter (1970).

A single olivine megacryst (AK6-07) was identified in the Karowe mantle samples studied here. The sample is pale brown and exhibits undulose extinction with serpentine infilled fractures and veinlets.

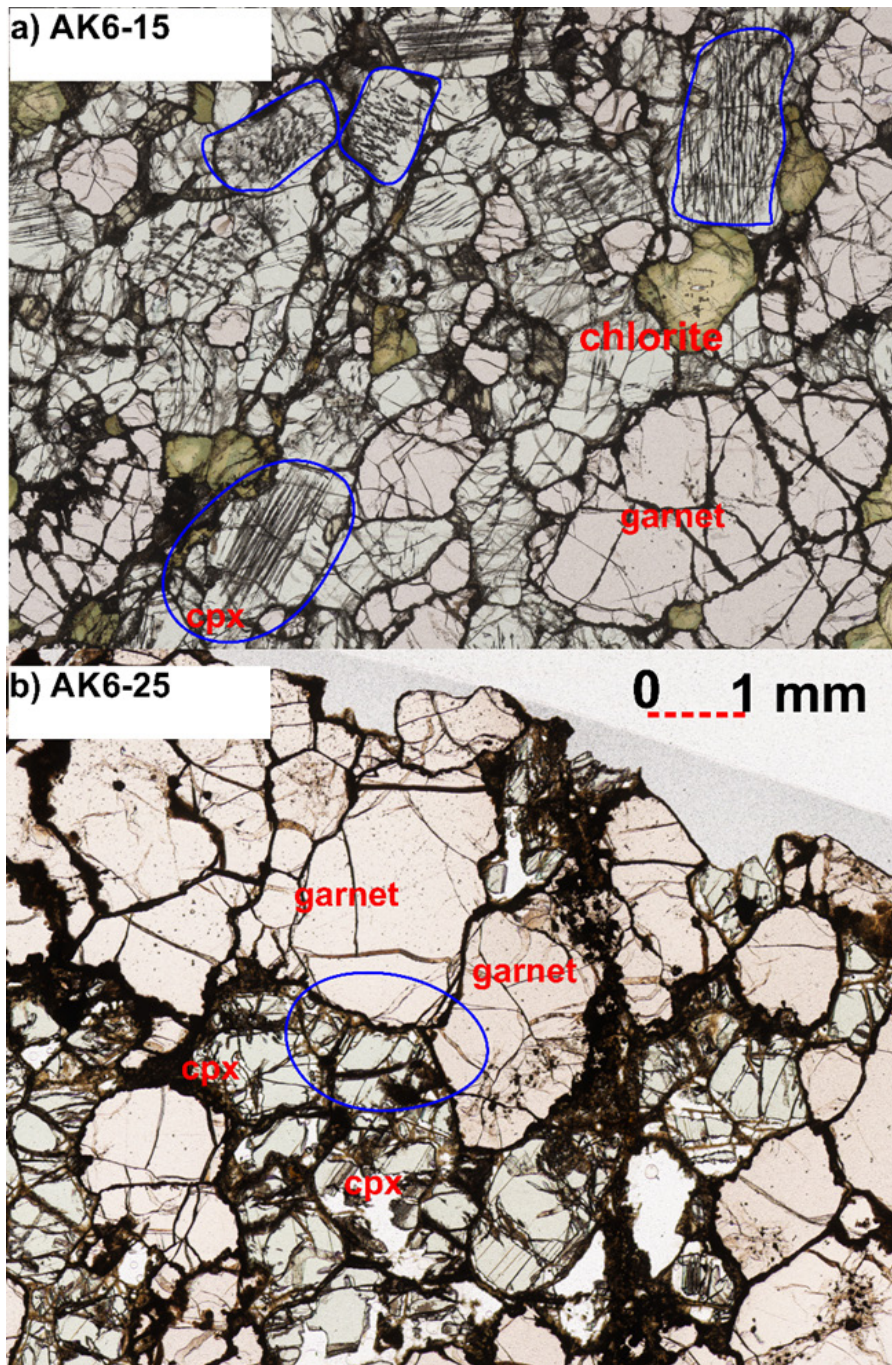


Fig. 2.2 Photomicrographs showing: a) exsolution textures in clinopyroxene from sample AK6-15 (circled area; above). b) Well equilibrated 120-degree grain boundaries defining an interlocking fabric characteristics for Group II eclogite in sample AK6-25

2.5.1 Major element compositions of the minerals

Olivine compositions in spinel lherzolites, garnet-spinel lherzolites, garnet lherzolite and garnet pyroxenite range from 89.4 to 92.6 in Mg# ($100 \times \text{Mg}/[\text{Mg}+\text{Fe}]$), with a mean and median of 92.0, when excluding Mg# of olivine in garnet pyroxenite from the calculations. This compares well with olivines from Letlhakane and Murowa-Sese peridotite xenoliths (Fig. 2.3). NiO contents vary from 0.37 to 0.43 wt% (Table A2). The single olivine megacryst has a low Mg# (83), low NiO content (0.16 wt%), and elevated concentrations of MnO (0.19 wt%) and CaO (0.51 wt%). This composition closely resembles those of the olivine megacrysts from Monastery and Jagersfontein in South Africa (Gurney et al. 1979; Hops et al. 1992).

The Mg# in orthopyroxenes ranges from 90.7 to 93.1, similar to that of coexisting olivines. The Al₂O₃ content in orthopyroxene varies between 1.5 and 3.3 wt % in spinel facies rocks and <1.0 wt% in garnet lherzolite (Fig. 2.4), while the TiO₂ content is less than 0.11 wt%, regardless of the facies. This compositional difference in orthopyroxenes from spinel and garnet peridotites is well known (Boyd et al. 1997 and 1999), with compositional overlap occurring at around the 2 wt% Al₂O₃ region (McDonough and Rudnick 1998). CaO content in orthopyroxene varies from 0.18 to 0.53 wt%, where spinel lherzolites are at the high end of the range (0.26 to 0.53 wt%) and the garnet facies at the lower end (≤ 0.25 wt%).

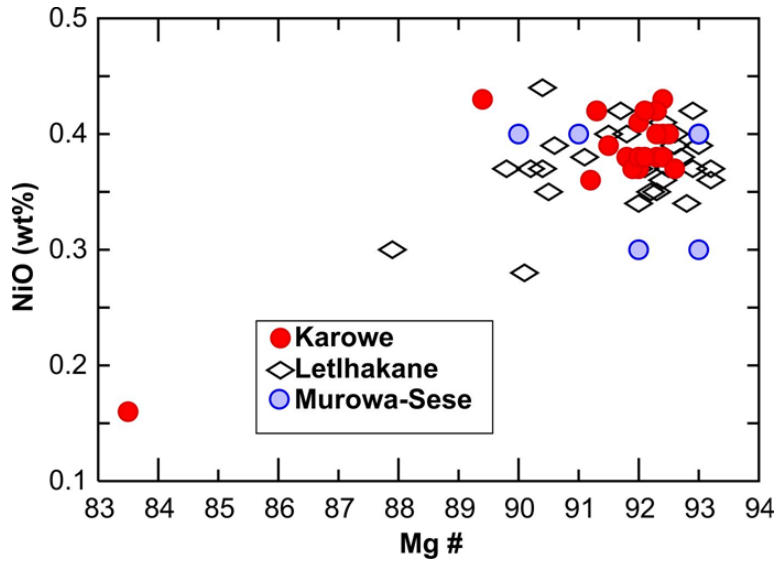


Fig. 2.3 Composition of olivines in xenoliths from Karowe and Letlhakane (western edge of the Zimbabwe craton; Stiefenhofer et al. 1997) and Murowa-Sese (southern part of the Zimbabwe craton; Smith et al. 2009)

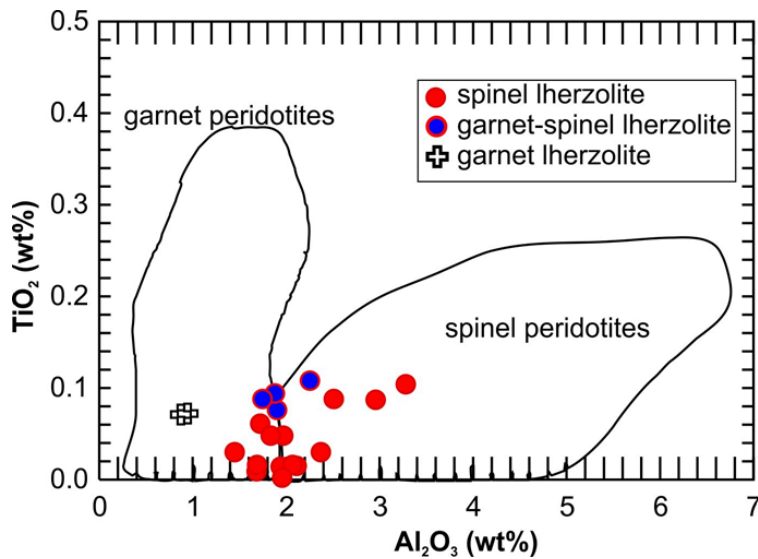


Fig. 2.4 Plot of TiO₂ vs Al₂O₃ for orthopyroxenes from spinel lherzolite, garnet-spinel lherzolite and garnet lherzolite xenoliths. Compositional fields for garnets and spinel peridotites are from McDonough and Rudnick (1988)

Clinopyroxenes are all Cr diopsides (Morimoto 1988). Cr₂O₃ contents vary from 0.16 to 1.83 wt% with molar Ca# ($100 \times \text{Ca}/[\text{Ca}+\text{Mg}+\text{Fe}]$) from 46.2 to 50.0. The lithological suites can

be divided on the basis of their Mg#: peridotitic clinopyroxenes have higher Mg# (93 to 95) than pyroxenitic (90.2 to 92.6) and eclogitic clinopyroxenes (85.6). Clinopyroxenes with abundant exsolution lamellae (sample AK6-03 and AK06-24 discussed above) have the highest Al₂O₃ contents (>5 wt%) and show excess Al over Na+K cation contents (Fig. 2.5 and Table A2), consistent with the presence of a Tschermaks component. For pyroxenitic clinopyroxenes, jadeite component ranges from 6 to 15 % (calculated as $100 \times 2\text{Na} / (2\text{Na} + \text{Ca} + \text{Mg} + \text{Fe})$; Morimoto 1988) and peridotitic clinopyroxenes contains between 9 and 19 % jadeite component.

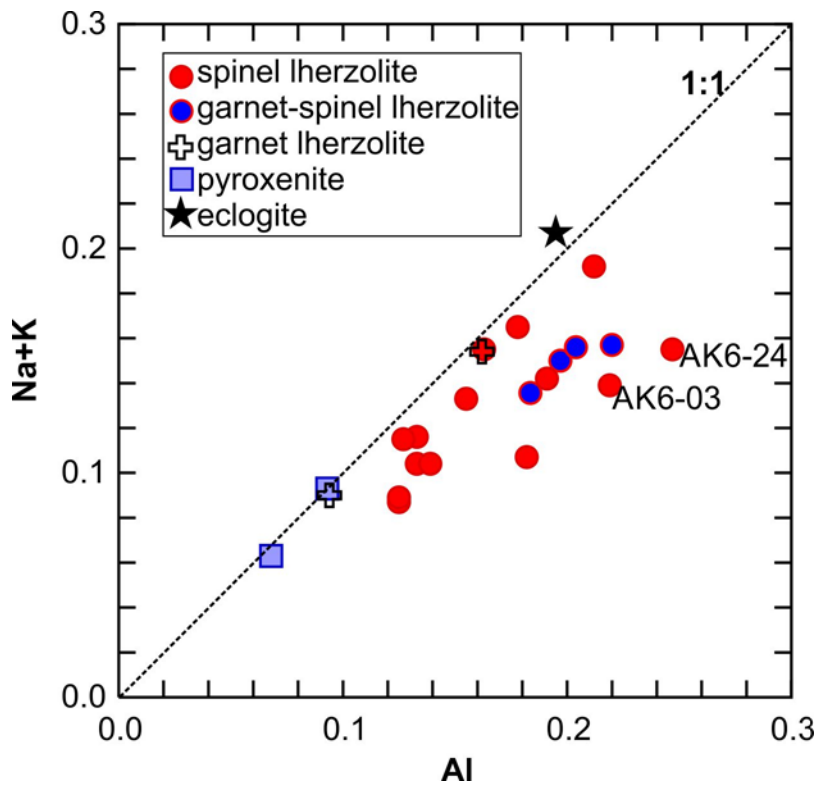


Fig. 2.5 Plot of Na+K versus Al cations for clinopyroxene from Karowe mantle xenoliths. Clinopyroxenes coexisting with spinel show excess of Al over Na indicative of the presence of a Tschermaks component. AK6-03 and AK6-24 are clinopyroxenes with exsolution lamellae. Dashed line indicates a 1:1 ratio between Na + K and Al

Garnets from the nine xenoliths studied here contain low CaO (<5 wt%) and Cr₂O₃ (≤1.5 wt%) as shown in Fig. 2.6. Five of the garnets, one from a garnet lherzolite and four from garnet-spinel lherzolites have high Mg# (77 to 82) and Cr₂O₃ content ranges from 1.0 to 1.5 wt%. These

values fall within the range of G9 garnets [$Mg\# (\geq 70 \text{ to } < 90)$ and $Cr_2O_3 (\geq 1.0 \text{ to } < 20 \text{ wt}\%)$]; Grütter et al. 2004]. In terms of garnet compositions, sample AK6-19 classified as garnet peridotite based on petrography but contains pyroxenitic garnet with TiO_2 and Cr_2O_3 contents of 0.12 wt% and 0.58 wt% respectively. This garnet belongs to the G4 category (Grütter et al. 2004) like the garnets from the two petrographic pyroxenites and the eclogite (Fig. 2.6).

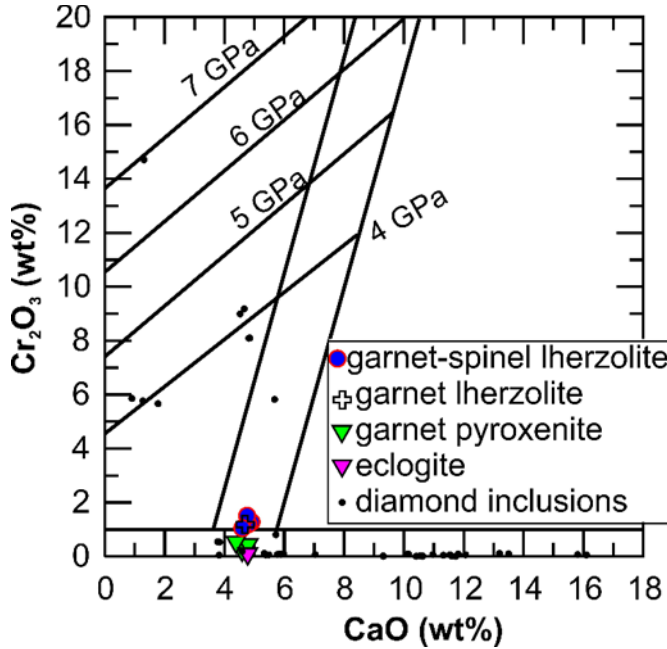


Fig.2.6 CaO vs Cr_2O_3 diagram with compositional fields from Grütter et al. (2004). Garnets from xenoliths are shown in comparison with the data from inclusions in Karowe diamonds (Motsamai et al. 2018)

Spinel grains contain variable concentrations of Al_2O_3 (30 to 56 wt%; median: 38), accompanied by a wide range of Cr# [13 to 47; median: 36; molar $100 \times Cr/(Cr+Al)$]. High Al contents (47 to 56 wt% Al_2O_3) are notable in four samples from the spinel lherzolite suite (AK6-03, AK6-08, AK6-22, and AK6-24). These samples contain orange-brown coloured spinels with the lowest Cr# (13 to 25). TiO_2 contents are all less than 0.20 wt%, but highest in spinels from the garnet-spinel lherzolite suite where TiO_2 concentrations are restricted to between 0.17 and 0.20 wt% (Fig. 2.7 and Table A2).

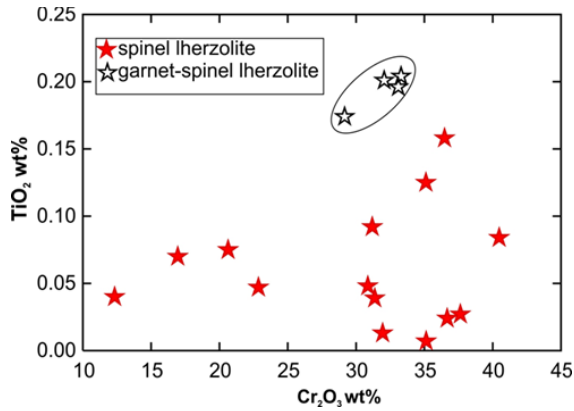


Fig. 2.7 Plot of Cr₂O₃ vs TiO₂ in spinel from Karowe xenoliths

2.5.2 REE and trace element compositions of clinopyroxenes and garnets

Trace element concentrations of clinopyroxenes and garnets from peridotite, pyroxenite, and eclogite xenoliths can be divided into five groups based on the rock types and REE_N patterns (Fig. 2.8, 2.9 and 2.10; see Table A4 for values). Two of the six clinopyroxenes from garnet-free spinel lherzolites show slightly depleted LREE_N ($La_N/Sm_N=0.24$ to 0.35) combined with flat MREE_N to HREE_N (Fig. 2.8). The remaining four clinopyroxenes display moderately LREE_N enriched patterns. With the exception of two samples showing relatively high LREE and MREE contents, the REE_N patterns are similar to those of Letlhakane spinel lherzolites (Fig. 2.8; Borst 2012) and those from cratonic lherzolites in general (Pearson et al. 2003). All clinopyroxenes in the spinel-facies peridotites have higher HREE_N (2 to $11 \times$ chondritic abundances) than those in garnet-bearing peridotites (0.2 to $1.0 \times$ chondritic abundances), irrespective of the degree of LREE enrichment. Five clinopyroxenes from garnet-bearing spinel lherzolites show strongly enriched LREE_N at ~ 20 to $80 \times$ chondritic abundances, then gradually decreasing in MREE_N and HREE_N towards Lu_N (Fig. 2.9a). The remaining four clinopyroxenes, three from pyroxenites and one from eclogite, show broadly similar REE_N patterns to those of garnet-bearing spinel lherzolites, but more enriched LREE_N (30 to $100 \times$ chondritic abundance) and depleted HREE (Lu_N ~ 0.2 ; Fig.

2.9b). All analysed clinopyroxenes here, exhibit strong negative Nb anomalies when chondrite normalised (not shown). Negative Nb anomalies are a common feature of mantle diopsides (Norman 1998).

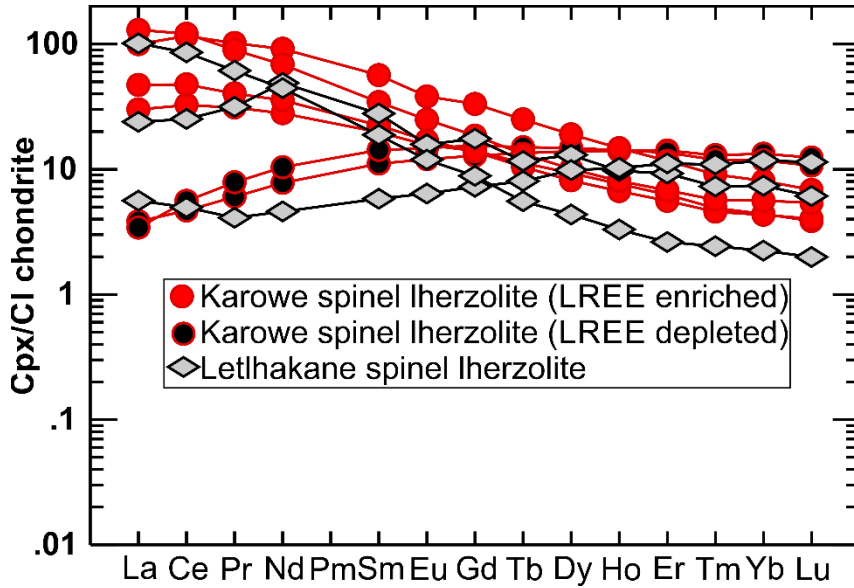


Fig. 2.8 C1 chondrite normalized (McDonough and Sun 1995) REE_N patterns of clinopyroxenes from the Karowe spinel lherzolite suite compared to Letlhakane samples (Borst 2012)

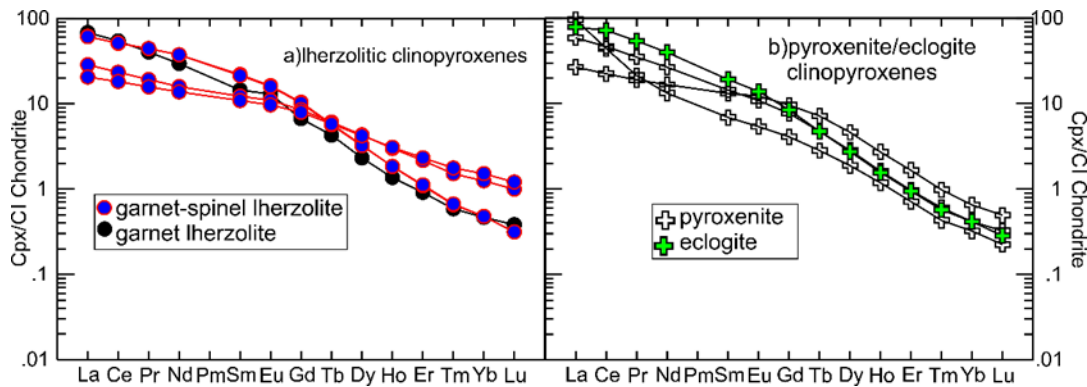


Fig. 2.9 C1-chondrite normalized (McDonough and Sun 1995) REE patterns in clinopyroxenes from (a) garnet/spinel facies and (b) pyroxenite/eclogite xenoliths

Five lherzolitic garnets, one from garnet lherzolite and four from garnet-spinel lherzolites have normal REE_N patterns with high HREE_N concentrations at about 10 to 60 × chondritic

abundance (Fig. 2.10a). The other four garnets belonging to the pyroxenitic (n=3) and eclogitic (n=1) suites, show typical patterns for eclogitic/pyroxenitic garnets with an increase from about ~ 0.3 chondritic LREE_N to ~ 30 chondritic HREE_N (Fig. 2.10b).

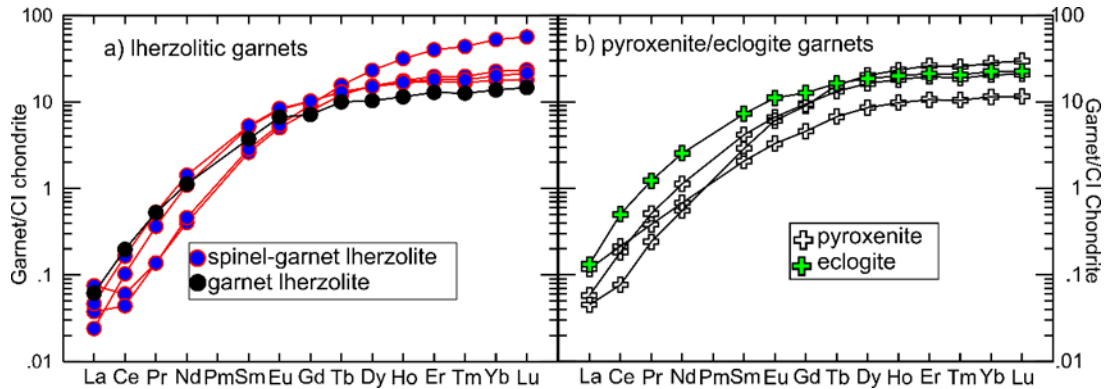


Fig. 2.10 C1-chondrite normalized (McDonough and Sun 1995) REE patterns of garnets from (a) garnet/spinel facies and (b) pyroxenite/eclogite xenoliths

2.5.3 Geothermobarometry

Estimation of the pressure-temperature (P-T) conditions of equilibration for mantle rocks requires equilibrium conditions between constituent mineral phases (i.e. garnet, spinel, clinopyroxene, orthopyroxene, and olivine). Chemical equilibrium within our spinel lherzolite and garnet-spinel lherzolite xenolith samples was checked by comparing thermometric results obtained using the independent thermometers of Taylor (1998; clinopyroxene-based) and Brey and Köhler (1990; based on Ca in orthopyroxene). At a pre-set pressure of 2 GPa (Table 2.0 and Fig. 2.11), the enstatite-in-clinopyroxene thermometer yields lower temperatures (557 to 804 °C) than those calculated using the Ca-in-orthopyroxene thermometer (681 to 931 °C), which translates into an average temperature difference of 83°C.

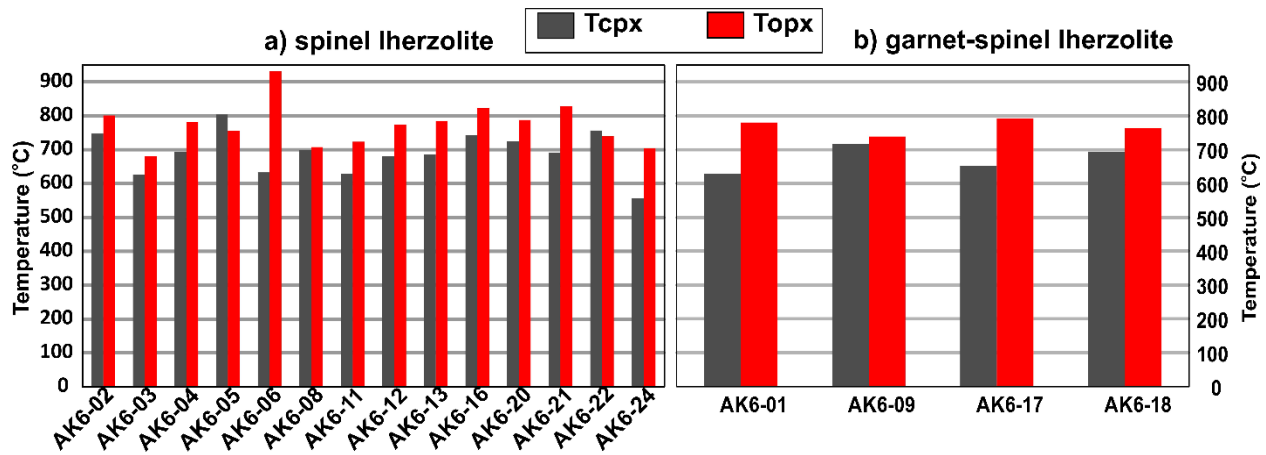


Fig. 2.11 Comparison of calculated temperatures for spinel lherzolite and garnet-spinel lherzolite xenoliths from Karowe using the clinopyroxene-based thermometer of Taylor (1998) in grey and the Ca in orthopyroxene thermometer of Brey and Köhler (1990) in red

The pressures and temperatures for clinopyroxenes from concentrate were determined by single clinopyroxene thermobarometry (Nimis and Taylor 2000). The thermobarometer utilises the Cr-in-clinopyroxene barometer and enstatite-in-clinopyroxene thermometer. From a total of 106 grains analysed (see Appendix A; Table A3), 25 samples with Cr# between 13 and 44 pass the compositional filters of Nimis and Grütter (2010) and Zibera et al. (2016). They yield temperatures between 700 and 1033 °C and pressures from 2.2 to 4.4 GPa, which correspond to ~69 to ~138 km depth. Excluding all samples falling below 2.5 GPa as potentially being derived from garnet-free assemblages, most of the low temperature clinopyroxene xenocrysts cluster near the 40 mW/m² model geotherm of Hasterok and Chapman (2011) with a maximum temperature of 840 °C and a maximum depth of approximately 100 km, overlapping with a single low-temperature garnet lherzolite (Table 2.0; Fig. 2.12). Conversely, those yielding high equilibration temperatures (900-1050 °C) form a separate cluster at greater depth (~120-140 km), falling between the 39 and 40 mW/m² model geotherms of Hasterok and Chapman (2011) and overlapping with one non-touching garnet-orthopyroxene inclusion pair from a Karowe diamond (Fig. 2.12). Overall, our

results are in good agreement with both the 40 mW/m² paleogeotherm derived for Letlhakane by Stiefenhofer et al. (1997) using garnet peridotite xenoliths data and Karowe peridotitic diamond inclusions results (Fig. 2.12). Due to lower temperatures yielded by spinel facies (557 to 804 °C), the values were not projected on the local paleogeotherm. In addition, all the four garnet-spinel lherzolite samples recorded pressures below 2.0 GPa (Table 2.0) and were not plotted in both Fig. 2.12 and Fig. 2.13.

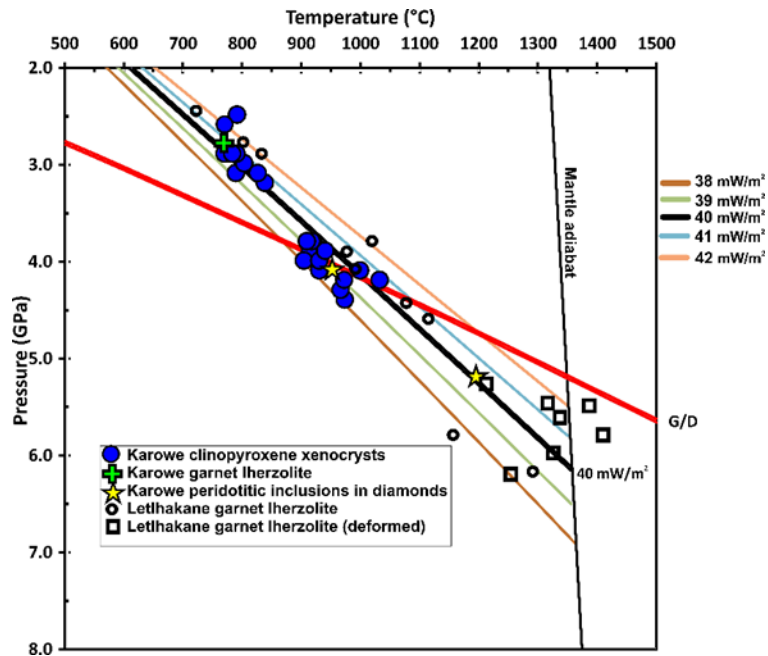


Fig.2.12 Cr-diopside single grain pressure-temperature (P-T) results obtained using Nimis and Taylor (2000) geothermobarometry compared with two non-touching garnet-orthopyroxene inclusions pairs from Karowe diamonds (Brey and Köhler 1990; Harley 1984) and from Letlhakane peridotitic xenoliths (Brey and Köhler 1990). Model geotherms for 38 to 42mW/m² surface heat flow are from Hasterok and Chapman (2011) while the graphite-diamond transition (G/D) is from Day (2012)

A model geotherm for the Karowe lithospheric mantle was constructed using the FITPLOT regression approach (Mather et al., 2011; Fig. 2.13) and data from Fig. 2.12, assuming a uniform crustal heat production of $\sim 0.86 \mu\text{W}/\text{m}^3$ in accordance with the models of Kramers et al. (2001) and a total crustal thickness of 40 km from Gore et al. (2009). The results show that the

lithospheric thickness of Karowe extends to a depth of 210 km, which is within error of the regional value of 220 km depth estimated by Miensoopust et al. (2011) using magnetotelluric methods.

The pressure and temperature estimates for the four garnet-spinel lherzolites and a single garnet lherzolite (Table 2.0) were calculated using garnet-orthopyroxene-clinopyroxene geothermobarometry (Nickel and Green 1985; Brey and Köhler 1990). The single garnet lherzolite yields a low temperature (768 °C), but falls within the low temperature end (750 to 800 °C) reported for Kaapvaal garnet peridotites (Boyd et al. 1999).

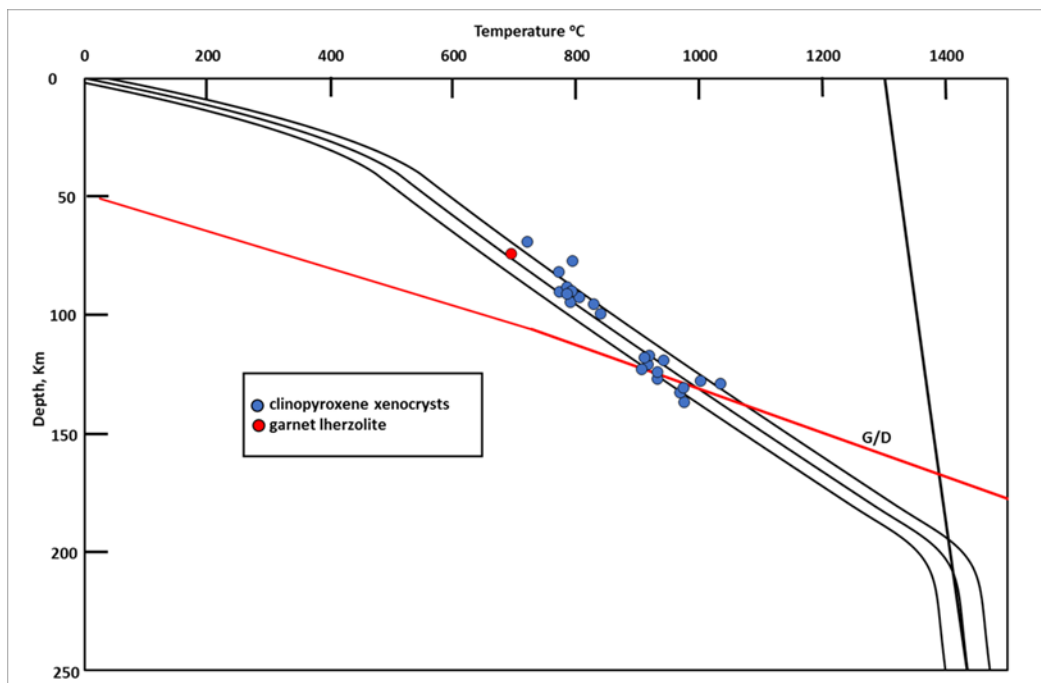


Fig. 2.13 FITPLOT geotherm regression showing the modelled geotherm for Karowe xenocrysts using the geothermobarometer of Nimis and Taylor (2000) and a single garnet lherzolite xenolith (Nickel and Green 1985; Brey and Köhler 1990). The model geotherm has crustal heat production of $0.86 \mu\text{W}/\text{m}^3$ in accordance with models of Kramers et al. (2001) while the graphite-diamond transition (G/D) is from (Day 2012). Error envelop denotes the 1-sigma uncertainty in the fit to the depth parameter

Application of the garnet/clinopyroxene Fe-Mg exchange thermometer of Krogh (1988) at a pre-set pressure of 5 GPa (Table 2.0) to the two garnet-clinopyroxenites yields temperatures of 803 and 855 °C while the single eclogite returns a temperature of 906 °C. These temperatures

are too low to be derived from such a high assumed pressure on a 40 mW/m^2 cratonic geotherm. For the third pyroxenite sample (AK6-19) which contains orthopyroxene, a combination of the Krogh (1988) thermometer and the barometer of Brey and Köhler (1990) gives an estimated equilibrium temperature of $766 \text{ }^\circ\text{C}$ at 2.6 GPa pressure, more in keeping with the geotherm structure.

Table 2.0: Equilibrium pressure and temperature estimates for Karowe xenoliths

Sample #	Rock type	Enstatite in cpx thermometer Taylor (1998) @ 2 GPa	Ca in opx thermometer Brey and Köhler (1990) @ 2 GPa with corrections of Nimis & Grütter (2010) for Temp <900 °C	Fe-Mg (cpx/gt) exchange thermometer Krogh (1988) @ 5 GPa	gt-opx barometer Nickel and Green (1985) combined with Ca in opx thermometer of Brey and Köhler (1990)		gt-opx barometer of Brey and Köhler (1990) combined with Fe-Mg (cpx/gt) exchange thermometer of Krogh (1988)	
		T°C	T°C	T°C	GPa	T°C	GPa	T°C
AK6-02	spinel lherzolite	747	801					
AK6-03	spinel lherzolite	627	681					
AK6-04	spinel lherzolite	695	782					
AK6-05	spinel lherzolite	804	756					
AK6-06	spinel lherzolite	633	931					
AK6-08	spinel lherzolite	689	708					
AK6-11	spinel lherzolite	629	724					
AK6-12	spinel lherzolite	680	774					
AK6-13	spinel lherzolite	686	785					

cpx= clinopyroxene; opx= orthopyroxene; gt=garnet

Table 2.0 continues....

Sample #	Rock type	Enstatite in cpx thermometer Taylor (1998) @ 2 GPa	Ca in opx thermometer Brey and Köhler (1990) @ 2 GPa with corrections of Nimis & Grütter (2010) for Temp <900 °C	Fe-Mg (cpx/gt) exchange thermometer Krogh (1988) @ 5 GPa	gt-opx barometer Nickel and Green (1985) combined with Ca in opx thermometer of Brey and Köhler (1990)		gt-opx barometer of Brey and Köhler (1990) combined with Fe-Mg (cpx/gt) exchange thermometer of Krogh (1988)	
		T°C	T°C	T°C	GPa	T°C	GPa	T°C
AK6-16	spinel lherzolite	743	823					
AK6-21	spinel lherzolite	691	828					
AK6-22	spinel lherzolite	757	740					
AK6-24	spinel lherzolite	557	704					
AK6-01	spinel-garnet lherzolite	629	712		1.3	674		
AK6-09	spinel-garnet lherzolite	717	654		1.2	609		

cpx= clinopyroxene; opx= orthopyroxene; gt=garnet

Table 2.0 continues....

Sample #	Rock type	Enstatite in cpx thermometer Taylor (1998) @ 2 GPa	Ca in opx thermometer Brey and Köhler (1990) @ 2 GPa with corrections of Nimis & Grütter (2010) for Temp <900 °C	Fe-Mg (cpx/gt) exchange thermometer Krogh (1988) @ 5 GPa	gt-opx barometer Nickel and Green (1985) combined with Ca in opx thermometer of Brey and Köhler (1990)		gt-opx barometer of Brey and Köhler (1990) combined with Fe-Mg (cpx/gt) exchange thermometer of Krogh (1988)	
		T°C	T°C	T°C	GPa	T°C	GPa	T°C
AK6-17	spinel-garnet lherzolite	652	727		1.7	710		
AK6-18	spinel-garnet lherzolite	694	689		1.6	666		
AK6-10	garnet lherzolite	683	724		2.8	768		
AK6-19	garnet-pyroxenite			852			2.6	766
AK6-14	garnet- clinopyroxenite			803				
AK6-15	garnet- clinopyroxenite			855				
AK6-25	eclogite			906				

cpx= clinopyroxene; opx= orthopyroxene; gt=garnet

2.6 Discussion

2.6.1 Comparison of xenoliths with inclusions in diamonds from Karowe

More than half of the inclusions in Karowe diamonds are derived from eclogitic sources (Motsamai et al. 2018), but only one eclogite (of non-diamondiferous nature) was found among the 24 xenoliths studied here. Therefore, little or no compositional relations are evident between our small xenolith population and inclusions in diamonds. However, the compositions of eclogitic garnet inclusions in Karowe diamonds are variable and at the low-CaO end of the population they compositionally overlap with those of the garnets in eclogite and pyroxenite xenoliths (Fig. 2.6). Pyroxenites are more abundant (n=3) than eclogites (n=1) in the Karowe mantle xenolith sample. For the peridotitic xenoliths, the kimberlites sampled abundant non-diamondiferous, low-temperature spinel peridotites and few garnet-spinel peridotites. The chemistry of garnets in the peridotite xenoliths are completely different from those of the garnet inclusions within diamonds. The latter are mostly depleted while the former are strongly melt-metasomatised (Fig. 2.14).

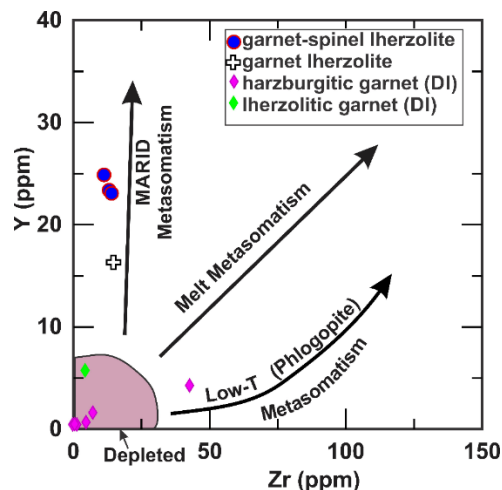


Fig. 2.14 Y versus Zr for garnets from peridotitic xenoliths and occurring as inclusions within diamonds (DI) from Karowe (Motsamai et al. 2018). Trends of melt- and fluid-style (phlogopite) metasomatism are for garnet xenocrysts from Griffin and Ryan (1995). MARID-like metasomatism (Creighton et al. 2009)

2.6.2 Equilibration conditions and textural relationships

It is apparent from Table 2.0 and Fig. 2.11 that application of the two-pyroxene thermometer of Taylor (1998) and the Ca-in-Opx thermometer of Brey & Kohler (1990) to coexisting clinopyroxene and orthopyroxene in spinel lherzolites, garnet-spinel lherzolites, and the single garnet lherzolite generally yields temperature estimates that agree within error (i.e., <100 °C difference at $T < 900$ °C Nimis and Grütter 2010). The spinel and garnet-spinel lherzolites all show almost identical enstatite-in-clinopyroxene temperatures (T_{cpx}) and for the Ca-in-orthopyroxene thermometer (T_{opx}), the spinel lherzolites record the highest temperatures (Table 2.0). Karowe spinel lherzolites have orthopyroxenes with higher CaO contents (up to 0.53 wt% max) than the garnet-bearing lherzolites and the CaO content of orthopyroxene increase with temperature (Brey and Köhler 1990). It is, therefore, likely that this counter-intuitive temperature increase is related to the exsolution observed in both pyroxenes or incomplete equilibration between coexisting orthopyroxene and clinopyroxene, e.g., during rapid cooling, but does not correspond to equilibration of spinel peridotites at greater depth.

A number of coarse-grained spinel lherzolites contain clinopyroxene and orthopyroxene grains displaying well developed exsolution features typical of slow cooling. The textures are generally similar to those observed in peridotite xenoliths from Letlhakane (Stiefenhofer et al. 1997) and the Kaapvaal Craton (Boyd et al. 1999; Grégoire et al. 2005). One of the garnet clinopyroxenite samples (AK6-15) exhibits multiple oriented exsolution lamellae with different thickness (i.e., thin vs thick; Fig. 2.2a), suggesting episodic cooling. Further evidence of cooling is given by the transition from garnet to spinel peridotite in Karowe peridotites, marked by a texturally distinct association of garnet grains with spinels in which large grains of garnet included

several small crystals of spinel, leading to the formation of sieve textures (Fig. 2.0a). This overgrowth of spinel by garnet is typically identified as the product of lithospheric cooling, probably under isobaric conditions, such that decreasing temperature conditions slowly favour garnet over spinel stability (Nixon and Boyd, 1979).

2.6.3 The Cretaceous mantle geotherm beneath Karowe and mantle sampling

Karowe is a productive diamond mine, but diamond-facies xenoliths, in particular garnet harzburgite and garnet dunite, the main host for diamonds (e.g., Sobolev 1977; Gurney et al. 1984; Pokhilenko et al. 1993) are absent in our sample. Xenoliths in Karowe kimberlites come from relatively low-pressure regions of the mantle, predominantly the spinel facies, and only few samples are garnet facies. The diamond host rocks are, therefore, not represented in the xenolith sample examined here. Clinopyroxene xenocrysts that pass the compositional filters of Nimis and Grütter (2010) and Zibera et al. (2016) show a larger range of depth derivation, from relatively shallow (~ 3.0 GPa and 800°C) to deeper mantle (~ 4.0 GPa and $900\text{-}1050^\circ\text{C}$) suggesting that the Karowe kimberlites sampled a small section of the diamond stability field (Fig. 2.12). The diamond inclusion sample at Karowe (Motsamai et al. 2018) indicates that a much larger portion of the lithospheric mantle in the diamond stability field was sampled. This suggests that both the available xenolith and xenocryst samples are representative of shallow lithospheric mantle, but not the deep lithosphere at Karowe. The scarcity of garnet harzburgites in the mantle xenolith suite could be because these xenoliths might have preferentially disaggregated within the kimberlite (Canil 1990).

The Karowe clinopyroxene xenocryst mantle samples cluster on a relatively cool mantle geotherm that is equivalent to that defined by mantle xenoliths derived over a larger depth range from the nearby Letlakane Mine. There is some evidence of temperatures above the general 40

mW/m² geotherm in the shallow xenocryst group; at these low temperatures, however, there are relatively large uncertainties related to the steepness of the 2-pyroxene solvus. More data is required to firmly establish the cause of this offset in the Karowe conductive geotherm.

Based on P-T results of garnet-spinel lherzolites (Table 2.0), the garnet-spinel transition in the lithospheric mantle beneath Karowe occurred between 38 and 53 km depths, which is below the experimentally determined stability depth (~50-60 km) of garnet formation (O'Neill 1981). This likely relates to a poor accuracy of geothermobarometric results at such low pressure and temperature conditions. The olivine megacryst recorded here has low Mg# (83) and Ni content (0.16 wt%) similar to the low-Cr megacryst of shallow origin reported by Gurney et al. (1979). The Karowe garnet clinopyroxenites appear to have been derived from similar depths to the eclogite if their calculated temperatures (800 to 900 °C; Table 2.0) are extrapolated to the local paleogeotherm.

The P-T results for both xenocrysts and mantle xenoliths produce a FITPLOT geotherm model for Karowe (Fig. 2.13), intersecting the mantle adiabat at approximately 210 km depth. This implies that the depth between the intersection of the graphite-diamond transition and the base of the lithospheric mantle at Karowe is ~90 km. This diamond window is equivalent to that beneath Letlhakane (Pearson et al., in press). Hence, despite the relatively sparse sampling evident in the small sample set examined here, a large diamond window beneath Karowe is consistent with the presence of economic diamond deposits in this region of the Zimbabwe craton.

2.6.4 Evidence for partial melting and metasomatic modification

The major and trace element compositions of minerals from Karowe spinel lherzolites reflect both partial melting and metasomatic processes within the upper mantle. The high Mg# in

olivines (median: 92.1) and orthopyroxenes (median: 92.4) are consistent with extensive melt depletion.

Spinel compositions can be a potential indicator of the extent of partial melting in mantle peridotites (Roeder 1994; Bernstein et al. 2006). Peridotite xenoliths derived from the Orapa-Letlhakane-Karowe kimberlite cluster show varied and complex spinel compositional variations. At Orapa, spinels have high Cr# of 56.4 to 77.5 (Meulemans et al. 2012), while in the Letlhakane xenoliths the spinels cover a wide range of compositions (Borst 2012), from low Cr# (21 to 41) and TiO₂ content (<1.0 wt%), comparable to Karowe spinels Cr# (13 to 47), to high Cr# (64.5 to 88.6) and TiO₂ content (3.21 wt%). High Cr# indicate that spinels crystallized in depleted source rocks or at high pressure in the garnet-facies (Roeder 1994; Barnes and Roeder 2001). The occurrence of very low Cr#s (13 to 25) likely relates to secondary events (refertilisation). Focussing on the upper range in Cr# (~50), the protoliths of Karowe spinel lherzolite xenoliths originated by partial melting at relatively low pressure.

More established relationships exist between the degree of partial melting and olivine compositions (Walter 1998; Bernstein et al. 2007; Pearson and Wittig 2008). The median value of olivine Mg# in Karowe peridotites (92.0) is consistent with between 27 and 36 % melt removal depending on whether the 3 GPa or 7 GPa melt depletion curves in Fig. 2.15 are employed. This degree of melt depletion is beyond the point of “clinopyroxene-out” in almost all experimental studies (Walter 1998). The estimates of melt fraction removed (~30 %) are in-line with previous estimates for the extent of melting experienced by cratonic peridotites (Walter 1998; Bernstein et al. 2007; Pearson and Wittig 2008). Olivine compositions do not constrain the melting pressure. A possible guide in this regard would be bulk rock compositions. While we did not analyse bulk compositions in this study, due to the small size of the samples, a simple consideration of mineral

compositions and modal abundances indicates that our samples have low bulk Al_2O_3 , likely less than 1.5%. Such low bulk rock Al contents are most easily reconciled with low pressure melt extraction, where most of the melt extraction occurs between 5 and 2 GPa, compatible, for instance, with polybaric melting beneath a hot Archean ocean ridge (Stachel et al. 1998; Herzberg and Rudnick 2012; Pearson and Wittig 2014).

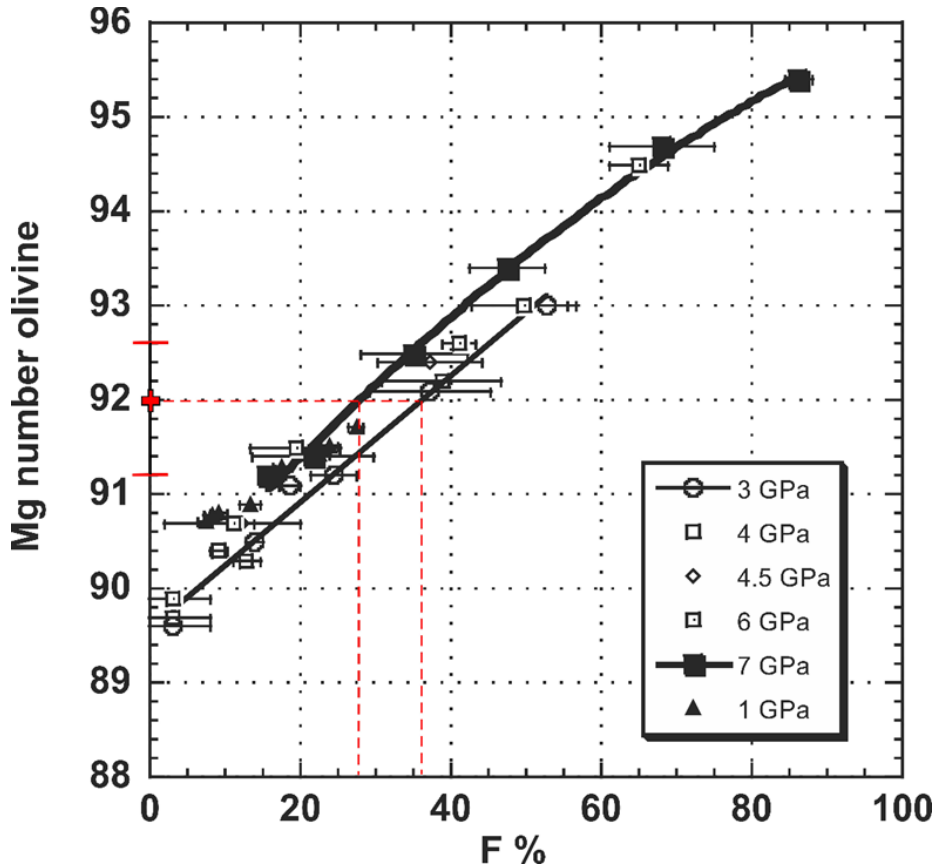


Fig. 2.15 Mg# of olivine vs percent melting (F) in residual peridotites from experiments at varying pressure (after Pearson & Wittig 2008). Based on the same mean and median value of olivine Mg# in Karowe peridotites, melt extraction between ~27 and ~36% is derived. The range of Mg# in Karowe olivines is represented with bars on the Y-axis

Rare earth elements provide another perspective on partial melting processes. Two of the clinopyroxenes show moderate LREE_N depletion relative to C1 chondrite ($\text{La}_N/\text{Sm}_N=0.24-0.35$) which is consistent with preferential LREE depletion during partial melting. Furthermore, the

HREE contents (e.g., Yb) decrease with increasing Mg# of the clinopyroxenes (Fig. 2.16), consistent with a control by partial melting. The varied enrichments of LREE_N in the other samples (Fig. 2.8) indicate subsequent re-introduction of such elements in originally depleted mantle rocks by metasomatic events (Simon et al. 2003). The clinopyroxenes have very high Y and Yb contents, which combined with their modest LREE depletions would indicate only very small degrees of partial melt extraction according to commonly used clinopyroxene melting models (Johnson et al. 1990; Norman 1998). This obviously conflicts with the degree of melting suggested by the olivine compositions and instead indicates a more complex origin for the clinopyroxene REE signatures that may involve metasomatic disturbance of originally residual clinopyroxene or an origin solely by metasomatism, from an unusual, low LREE melt.

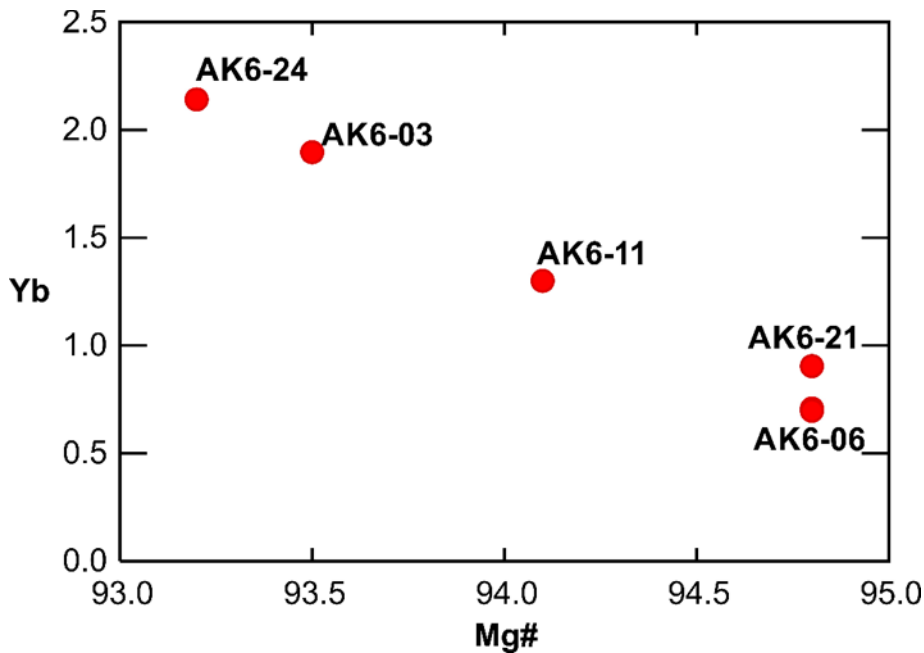


Fig. 2.16 Correlation of HREE contents (Yb) with increasing Mg# in clinopyroxenes

Garnet trace element systematics can also be used to examine melt depletion processes (Stachel et al. 1998). A plot of Y versus Zr in Karowe garnets (Fig. 2.14) indicates that their trace element systematics are dominated by MARID-style melt metasomatism (preferential enrichment

of Y; Creighton et al. 2009). The minor component of garnet peridotites sampled beneath Karowe consists of “refertilised” garnet-spinel lherzolites and melt-metasomatised garnet lherzolite. The REE_N patterns of garnets in garnet-spinel lherzolites resemble those of the garnet lherzolite showing HREE_N enrichment and LREE_N depletion, which is typical for lherzolitic garnets (Fig. 2.10). These garnets also contain almost identical CaO and Cr₂O₃ contents (Fig. 2.6). The Cr# of the spinels (33 to 38) and Al₂O₃ contents of orthopyroxenes (Fig. 2.4) in garnet-spinel peridotites also overlap with the ones from the melt depleted garnet free spinel peridotites. These similarities suggest that the garnet-spinel peridotites also initially experienced some form of melting event in the spinel stability field prior, to refertilisation. This lithospheric refertilisation through melt-related metasomatism, where lherzolitic garnets record high Y/Zr ratios (1.67-2.24; Fig. 2.14), might be related to either the intrusion of the Bushveld Complex at 2.054 Ga, which affected this portion of the lithosphere and is manifest as the Molopo-Farms complex this far NW, or to melt/fluids associated with formation of the Magondi Belt at around 1.8 Ga. This interpretation is consistent with the Re depletion ages for the xenoliths from Karowe, which tend to cluster between 2.0 and 2.3 Ga (Wudrick et al. 2017). Similar metasomatic refertilisation was observed in peridotitic xenoliths from the Premier mine (Viljoen et al. 2009), which is also known for producing large gem diamonds like Karowe.

Pyroxenite xenoliths recorded notable phlogopite modal metasomatism, with relatively high clinopyroxene modes (36 to 57%). This style of metasomatism is common in Letlhakane xenoliths (van Achterbergh et al. 2001) and widespread in the Kaapvaal craton (Griffin et al. 1999, Simon et al. 2007).

2.7 Conclusions

Mantle xenoliths from Karowe show petrographic characteristics and mineral compositions comparable to xenoliths from Letlhakane. Karowe xenoliths are mostly derived from shallow mantle (14 out of 24) and encountered variable degrees of partial melting and metasomatic processes. The abundant garnet-free spinel lherzolites have coarse-grained to granuloblastic textures with equilibration temperatures ranging from 630 to 800 °C. The Mg# in olivine grains range between 91.2 and 92.5 (median: 92.1), consistent with extensive melt depletion (about 30 % melt extracted). Clinopyroxenes show variable LREE_N enrichment (La_N/Yb_N=0.29-23). The small proportion of xenoliths sampled from the garnet facies is represented by garnet-spinel lherzolites (n=4), one spinel-free garnet peridotite, garnet clinopyroxenites (n=3) and a single eclogite. Garnet REE_N patterns reveal enrichment that is related to melt metasomatism and modal metasomatism, which is indicated by the presence of phlogopite in pyroxenites.

Clinopyroxene-based geothermobarometry on mineral concentrate and a garnet lherzolite xenolith define a 39 to 40 mW/m² (Hasterok and Chapman 2011) paleogeotherm, intersecting the mantle adiabat at about 210 km depth. This implies that the diamond window in the lithospheric mantle beneath Karowe is approximately 90 km thick, consistent with other estimates of the depth of the lithosphere in this region of the Zimbabwe Craton derived from petrology and geophysics.

Chapter Three

3.0 Mineral inclusions in diamonds from Karowe Mine, Botswana: super-deep sources for super-sized diamonds?

3.1 Introduction

The recent recovery of exceptionally large diamonds (including the 1,109 carats Lesedi la Rona) at the Karowe mine in north-eastern Botswana raises the question: what controls such an exceptionally coarse size-frequency distribution? To address this question we studied the mineralogy and chemistry of inclusions in a representative suite of diamonds from this mine. Based on recent conflicting views on the origin of very large (typically nitrogen-free) gem diamonds, invoking either a megacryst-like origin within the lithosphere (Moore 2014) or crystallization in the sublithospheric mantle (Smith et al. 2016), particular emphasis was placed on evaluating the presence or absence of inclusions indicative of a superdeep origin. A second goal of the study was to employ lithospheric inclusions in diamonds from Karowe to establish the compositional characteristics, the thermal conditions, and the thickness of the lithospheric mantle at the time of diamond formation.

3.1.1 Previous work in the Orapa cluster and Zimbabwe Craton

The Orapa, Letlhakane, Damtshaa, and Karowe mines form part of the Orapa kimberlite cluster, located in north-east Botswana, along the western edge of the Zimbabwe Craton. The lithospheric mantle beneath this region has been studied for the past three decades both through diamonds and their mineral inclusions and through mantle xenoliths collected from the Orapa, Letlhakane, and Damtshaa kimberlites (Shee and Gurney 1979; Gurney et al. 1984). Inclusion studies revealed that

the diamond sources beneath Orapa, Letlhakane, and Damtshaa are compositionally distinct (Deines and Harris 2004; Deines et al. 2009). At Letlhakane and Damtshaa, peridotitic inclusions are more common compared to a predominately eclogitic diamond association at Orapa. Peridotitic diamond substrates in the lithospheric mantle beneath Orapa were investigated by Stachel et al. (2004b), who found that inclusions in diamond reflect mild metasomatic overprint through CHO fluids compared to the extensive metasomatic modification observed in peridotite xenoliths (Griffin et al. 2003). The authors attributed this difference to peridotitic diamond formation that predated major modification of the lithosphere during Proterozoic rifting and compression.

Outside the Orapa kimberlite cluster, information about the lithospheric mantle of the Zimbabwe Craton is principally based on mantle xenoliths and inclusion-bearing diamonds from the Cambrian kimberlites at Murowa and Sese, located in the southern part of the craton. The present evidence indicates that the lithospheric mantle beneath the southern Zimbabwe Craton is exceptionally depleted with diamond substrates of harzburgitic-dunitic paragenesis (Smith et al. 2009). Similar strongly depleted harzburgitic diamond sources were also established for the River Ranch kimberlite, located in the Central Zone of the Limpopo Mobile Belt (Kopylova et al. 1997). The Zimbabwe Craton and parts of the Limpopo Mobile Belt are underlain by a thick (~225 to 250 km) mantle root, with lithosphere thickness increasing even further towards the south beneath the Kaapvaal Craton (~250 to 300 km; Fouch et al. 2004).

3.2 Samples and analytical techniques

A total of 120 inclusion-bearing diamonds was selected from run-of-mine production at the sorting office of Karowe Diamond Mine in Gaborone, Botswana. The collected diamonds range in size from about 2 to 3 mm (the equivalent to -7+5, -9+7, and -11+9 Diamond Trading Company sieve

classes). The diamonds were visually inspected under a binocular microscope and fully documented for shape, colour and surface features, before being photographed. Subsequently, inclusions were extracted by crushing of the diamonds in a purpose-built steel cracker, mounted individually in epoxy and polished to a 0.25 μm finish. The inclusions measured between 60 μm and 500 μm in longest dimension. From the initial 119 diamonds, 171 mineral inclusions were successfully recovered and prepared from 107 diamonds. For the remaining 13 diamonds, inclusions were either not recovered or lost during preparation.

Major and minor element compositions of mineral inclusions were analysed using a JEOL 8900R electron probe micro-analyser (EPMA). All elements were measured with an accelerating voltage of 20 kV, beam current of 20 nA and ≤ 2 μm beam diameter. The typical total background counting times were 30 to 60 seconds equals the on-peak counting times. Standards for the two light major elements Si ($\text{K}\alpha$) and Mg ($\text{K}\alpha$) were pyrope garnet, diopside or forsterite (Fo90.5), depending on the mineral analyzed. For the remaining elements, standards were albite (Na- $\text{K}\alpha$), pyrope garnet (Al- $\text{K}\alpha$), apatite (P- $\text{K}\alpha$), sanidine (K- $\text{K}\alpha$), labradorite (Ca- $\text{K}\alpha$), rutile (Ti- $\text{K}\alpha$), chromium oxide (Cr- $\text{K}\alpha$), spessartine (Mn- $\text{K}\alpha$), fayalite (Fe- $\text{K}\alpha$), nickel wire (Ni- $\text{K}\alpha$). The standards are described in more detail in Table A1 (see appendix A). The CITZAF correction (Armstrong 1995) was utilized for data reduction. Three to five spots were analysed on each sample depending on the size of the mineral grain. After assessing homogeneity, the oxide concentrations measured were then averaged for individual grains. The resulting detection limits typically are ≤ 0.02 wt% oxide.

Rare earth element (REE) and trace element concentrations for selected garnet and clinopyroxene inclusions were measured using a Resonetics M-50 193 nm excimer laser coupled with a Thermo Element XR 2 sector-field inductively coupled plasma mass spectrometer (LA-

ICP-MS). Grains were ablated with a spot size of 50 or 75 μm at a laser frequency of 10 Hz and energy density of $\sim 4 \text{ J/cm}^2$. For each sample two or three spots were analyzed and an average of 100 sweeps through the mass spectrum were made for each analysis. Measurement time comprised of 40 seconds background collection followed by 60 seconds sample ablation. The ICP-MS was operated at low mass resolution mode ($M/\Delta M = \text{ca. } 300$). The ThO/Th signal was monitored to ensure that oxide production remained below 0.5 %. Calibration of relative element sensitivities was performed using the NIST SRM 612 glass reference material and ^{43}Ca was employed as an internal standard to normalize the signal intensities. Data processing was performed offline using Iolite v3 (Paton et al. 2011). Detection limits are ≤ 30 ppb for REE, Nb, Zr, Y, Sr, and ~ 1 ppm for Ti and Ni.

3.3 Results

Most of the 107 diamonds contained a single mineral inclusion, commonly olivine ($n=23$; Table 3.0). Twenty-three diamonds hosted two-phase assemblages and one diamond a three-phase assemblage (Table 3.0). Inclusions were subdivided into the peridotitic (lherzolitic and harzburgitic), eclogitic, and websteritic suites based on mineralogy and major element composition (Grütter et al. 2004; Gurney et al. 1984; Meyer 1987).

Table 3.0 Summary of analysed mineral inclusions contained in 107 Karowe diamonds and their parageneses.

Mineral	No. of Diamonds	Number of inclusions	Inclusion assemblage	Paragenesis
Olivine (ol)	30	38	(ol)=23,(gt+ol)=3,(opx+ol)=1, (sulph+ol)=1,(chr+ol)=2, (ol+opx+gt)=1	peridotitic
Mg-Chromite (chr)	6	11	(chr)=6	peridotitic
Orthopyroxene (opx)	4	6	(opx)=3,(gt+opx)=1	peridotitic
Ca-rich orthopyroxene (opx)	1	1	(Ca-rich opx)=1	websteritic
Clinopyroxene (cpx)	24	40	(cpx)=17,(sulph+cpx)=2,(gt+cpx)=5	eclogitic
Cr-diopside (Cr-diop)	1	1	(Cr-diop)=1	peridotitic
P-garnets (P-gt)	2	9	(P-gt)=2	peridotitic
E-garnets (E-gt)	15	33	(E-gt)=15	eclogitic
Majorite garnet (maj)	2	3	(maj)=1,(maj+cpx)=1	sublithospheric
Kyanite (kyn)	3	3	(kyn)=2, (gt+kyn)=1	eclogitic
Coesite (coe)	4	4	(coe+sulph)=1,(coe+cpx)=1, (coe+gt)=1,coe+ol=1	E-type(n=3) P-type(n=1)
Sulphide (sulph)	15	22	(sulph)=15;	E-type(n=12) P-type(n=3)
Total	107	171		

P-gt=peridotitic garnet; Cr-diop=Chrome diopside; chr=chromite; ol=olivine; opx=orthopyroxene; E-gt=eclogitic garnet; coe=coesite; cpx= clinopyroxene; kyn=kyanite; maj=majorite; sulph=sulphide

3.3.1 Major element compositions of inclusions and paragenetic associations

3.3.1.1 Eclogitic suite

The 33 recovered eclogitic garnets can be divided into two groups on the basis of their CaO contents (Grütter et al. 2004): low-Ca (CaO <6 wt%; n=11) and high-Ca (CaO ≥6 wt%; n=22). As observed by Stachel and Harris (2008), there is a crude positive correlation between Na and Ca content (see Table B1 in Appendix B), both generally increasing from low- to high-Ca garnets and with the most Na₂O-rich garnet (0.54 wt%, diamond KW79) also having the highest CaO concentration (16.1 wt%). A similar crude positive correlation with Ca content exists for Ti, with the exception of unusually high TiO₂ (1.7 wt%) being observed in two garnets with intermediate CaO content (10.1 wt%) from diamond KW56. The two Ti-rich garnets show unusually low Al₂O₃ contents (average 19.9 wt%), with the typically six-fold coordinated cations Ti, Al, and Cr summing to 3.77 ([O]=24). As there is no excess of Si over the available tetrahedral sites in these garnets, this apparent deficiency can only be compensated through the presence of ferric iron (Canil and O'Neill 1996). In diamond KW36, a single garnet was associated with a deep blue kyanite (Table B1) and contained 7.0 wt% CaO, which is too low for derivation from typical grosspyrite (Sobolev et al. 1968). The three (low-Ca) garnets with the highest Mg# [~70; molar 100×Mg/(Mg+Fe)] also have elevated Cr₂O₃ contents (ranging from 0.52-0.80 wt%). These characteristics indicate an affinity to the websteritic inclusion suite (Deines et al. 1993) but fall in a compositional range where a clear distinction between low-Ca eclogitic and websteritic garnets is not possible (Stachel and Harris 2008).

The 40 analysed eclogitic clinopyroxene inclusions range in composition from augites (n=16) to omphacites [n=24; jadeite component calculated as 100×2Na/(2Na+Ca+Mg+Fe); Morimoto 1988]. The augites are unusual among eclogitic clinopyroxene inclusions worldwide

with Cr₂O₃ contents extending to high values (average 0.15 wt%, max 0.27 wt%), high NiO (average 0.10 wt%), high MgO (average 19.8 wt%), and low jadeite contents (14.2-16.3 mol%) plus very low CaO (average 10.3, minimum 9.3 wt%). Their extremely low molar Ca# [$100 \times \text{Ca}/(\text{Ca} + \text{Mg} + \text{Fe})$] of 23.3 (range 21.4-24.9) is unique among eclogitic inclusions worldwide, with the exception of inclusions from Letlhakane in the same kimberlite cluster (Deines and Harris 2004). For omphacites (25.8-48.2 mol% jadeite) there is a crude negative correlation between Mg# and Ti content. The two omphacites with the highest jadeite content (from diamond KW66) have an unusually high Mg# (91.4-91.7). With increasing Al content, Karowe omphacites deviate from the near 1:1 correlation between Al and Na cation content shown by eclogitic clinopyroxene inclusions worldwide towards excess Al (Fig. 3.0), suggestive of an additional, higher than normal Tschermaks component (Stachel and Harris 2008). Seven omphacites coexist with either low-Ca garnets (n=3 from one diamond) or high-Ca garnets (n=4 from two diamonds) garnets. For this sample set, clinopyroxenes associated with low-Ca garnet, compared to those occurring with high-Ca garnet, have a higher Mg# (average of 77.8 versus 71.7), Cr₂O₃ content (0.10 versus 0.04 wt%) and K₂O abundance (0.16 versus 0.06 wt%) at decreased CaO contents (12.2 versus 14.7).

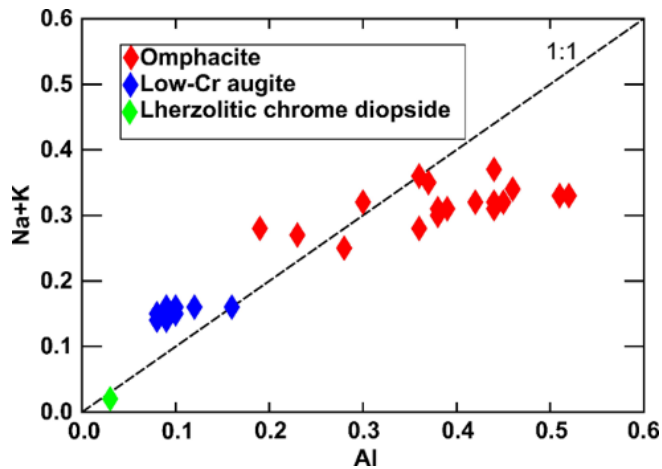


Fig. 3.0 Na+K versus Al cations for clinopyroxene inclusions from Karowe diamonds. Omphacitic clinopyroxenes show excess of Al over Na indicative of the presence of a Tschermaks component. Dashed line indicates a 1:1 ratio between Na and Al

Four SiO₂ (99.5-100.4 wt%) inclusions were recovered from four diamonds and are assumed to represent primary coesite. Of these, three co-exist with (1) a pair of low-Ca eclogitic garnets, (2) an omphacitic clinopyroxene, and (3) a low-Ni sulphide (monosulphide solid solution) inclusion, consistent with an eclogitic association. The fourth SiO₂ inclusion coexists with olivine (KW32e). Coesite may occur in peridotitic assemblages as a consequence of intense source carbonation (Wyllie and Huang 1976). As previously observed for inclusions in diamonds from the Renard Mine (Superior Craton; Hunt et al. 2012), the disequilibrium assemblage olivine + coesite requires continued diamond growth during progressive source carbonation, with the olivine inclusion representing an earlier growth stage. Two colourless and one deep blue kyanites inclusions were recovered. The latter coexisted with an orange garnet (KW36a; Table B1) and has elevated levels of TiO₂ (0.31 wt%), Cr₂O₃ (0.17 wt%), FeO (0.34 wt%), and MgO (0.18 wt%) compared to the two colourless kyanites that are ~99.8 % pure (Table B1).

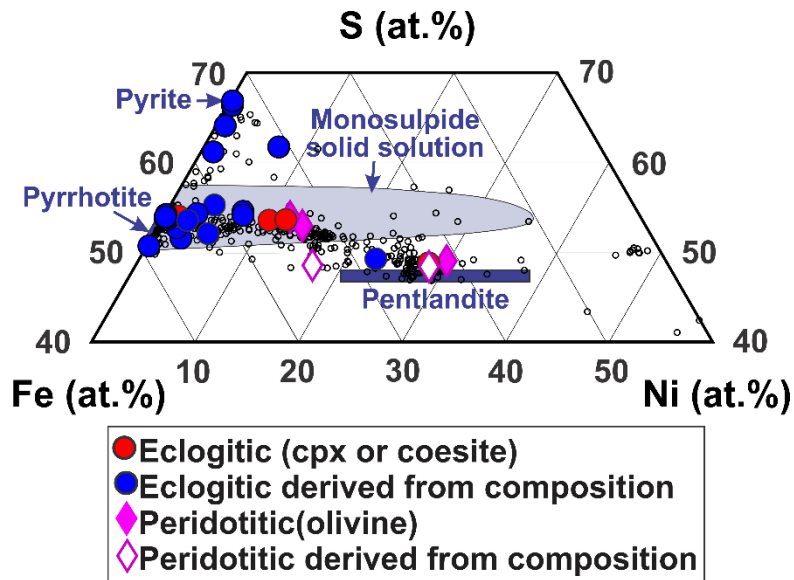


Fig. 3.1 Sulphide compositions in Fe-Ni-S quadrilateral (based on atomic percentages). Filled red circles indicate an eclogitic paragenesis based on coexisting silicate and oxide inclusions while filled blue circles reflect an eclogitic paragenesis inferred from sulphide compositions. Similarly, for the peridotitic suite filled and open symbols were used to reflect observed and inferred paragenesis. Compositional fields from Deines and Harris (1995) and small white circles from Stachel and Harris (2008)

Eighteen sulphide inclusions (12 single crystals and 6 polyphase grains; Table B2) are considered eclogitic. From the polyphase inclusions, five consist of two-phase and one of a three-phase assemblage. Inclusions were assigned an eclogitic paragenesis on the basis of co-existing eclogitic clinopyroxenes ($n=2$) and coesite ($n=1$) or <12 wt% Ni (Bulanova et al. 1996). A total of 25 sulphide phases were identified and plotted in a Fe-Ni-S quadrilateral diagram (Fig. 3.1). These include 12 occurrences of monosulphide solid solution (mss), of which 10 are Ni-poor (<10 wt%) and have a molar Ni/Fe ratio <0.2 . Two are associated with separate chalcopyrite phases. Two remaining mss are Ni-rich (13.9-16.1 wt%), exceeding the cut-off value for typical eclogitic sulphides. Both are, however, still considered eclogitic on the basis of coexisting clinopyroxene inclusions (omphacite and low-Cr augite). The mss occurring with low-Cr augite additionally coexists with pentlandite containing 16.1 wt% Ni. Furthermore, the mss and pentlandite inclusions

have detectable Cr contents (0.33 wt% and 0.29 wt%, respectively). Without the coexisting low-Cr augite inclusion, these two sulphides would have been assigned a peridotitic paragenesis (Stachel and Harris 2008), their compositions clearly reflect a chemically more depleted substrate than commonly observed for eclogitic inclusions. From the six low-Ni (<0.70 wt%) pyrrhotites, one coexisted with pyrite, one with a pyrite-chalcopyrite assemblage and one with pentlandite. This pentlandite is distinct with an elevated Co content (1.48 wt%) compared to all other eclogitic sulphide inclusions (<0.9 wt%). The remaining three inclusions mainly consist of pyrrhotite, with homogenous compositions. The Cu concentrations in chalcopyrite (n=3) range from 26.5 to 27.3 wt%.

3.3.1.2 Peridotitic suite

Of the nine peridotitic garnets recovered, eight are harzburgitic and one is lherzolitic (Fig. 3.2). Cr₂O₃ contents range from intermediate (5.7 wt%) to very high (14.7 wt%) and exceed the highest Cr₂O₃ concentrations previously recorded for a garnet inclusion from the Orapa kimberlite cluster (13.8 wt %; Deines and Harris 2004). Four garnets classify as low-Ca (CaO <1.8 wt%), indicative of derivation from extremely depleted, potentially dunitic sources (Grütter et al. 1999). Two of the harzburgitic and the one lherzolitic garnet have unusually high TiO₂ contents (0.19-0.24 wt%).

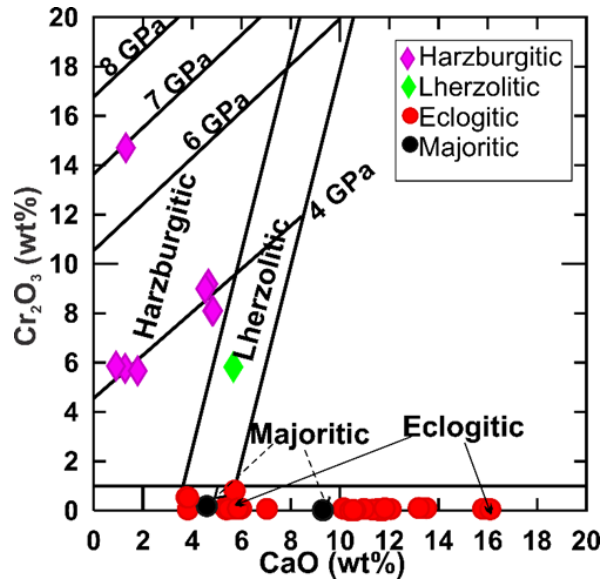


Fig. 3.2 Cr_2O_3 vs CaO diagram for garnets inclusions in Karowe diamonds. Isobars are from Grütter et al. (2006) and represent minimum pressures (as equilibrium with spinel is not established)

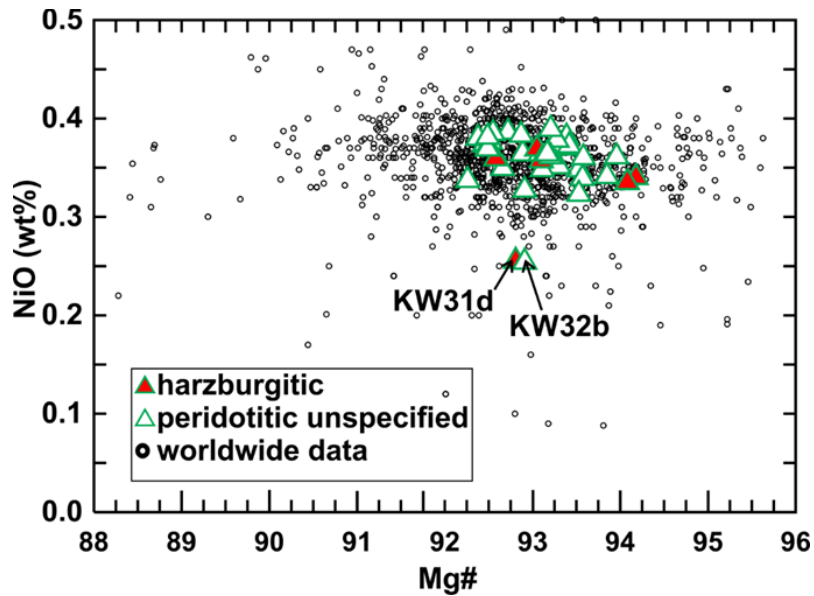


Fig. 3.3 NiO (wt%) versus molar Mg\# ($100 \times \text{Mg}/[\text{Mg} + \text{Fe}]$) in olivine inclusions from this study and localities worldwide ($n=1,306$; Stachel and Harris 2008)

Thirty eight olivine inclusions have a narrow range in Mg\# from 92.3 to 94.2 (Fig. 3.3), with a mean and median of 93.1. On the basis of coexisting garnets, six olivines can be assigned to the harzburgitic paragenesis with a Mg\# mean (93.3) and median (93.1), similar to the remaining

unassigned olivines, suggesting that all olivines may be harzburgitic. Karowe olivines fall into the normal ranges established for inclusions worldwide with the exception of three with unusual compositions: (1) two olivines have unusually low NiO (0.25 wt%; Fig. 3.3). One (KW31d) coexists with harzburgitic garnet and orthopyroxene and the other (KW32b) with coesite. (2) A single olivine in diamond KW111 has very high Cr₂O₃ (0.19 wt%), a feature that has been related to low Cr³⁺/Cr²⁺ in the growth environment associated with unusually reducing conditions (Li et al. 1995; Bell et al. 2014).

Six orthopyroxene inclusions have a narrow range in Mg# (93.6-94.5; mean and median of 94.0) and show high CaO contents (0.31-0.62 wt% CaO) relative to the more common Ca-depleted harzburgitic orthopyroxenes (CaO ≤ 0.16 wt%; Stachel and Harris 2008). They fall into a compositional range where harzburgitic and lherzolitic enstatites overlap; based on coexisting garnets, one inclusion is harzburgitic (KW31) and one lherzolitic (KW49). The lone recovered diopside inclusion recovered has a Mg# of 93.1, similar to the median value (92.9) for lherzolitic clinopyroxene inclusions worldwide but is unusually low in Al₂O₃ (0.67 wt%), Cr₂O₃ (0.55 wt%) and Na₂O (0.29 wt%) content (Fig. 3.0). Eleven Mg-chromites recovered show compositions typical for inclusions in diamond, with high Cr# [85.6-93.3; 100×Cr/(Cr+Al)] and generally low TiO₂ contents (0.06-0.40 wt%), with a single exception (KW5; 1.1 wt% TiO₂).

Four sulphide inclusions were classified as peridotitic. Of these, two are from a single diamond (KW101) where they co-existed with olivine, the other two are lone inclusions (Fig. 3.1). The two sulphides occurring with olivine are mss and have the elevated Cr contents (0.43 wt%) typically associated with a peridotitic paragenesis (Stachel and Harris 2008). The mss with the lower Ni content (16.3 wt%) shows exsolution of pentlandite around the edges and includes a platinum nugget (1 µm diameter; detected by EDS). Of the two remaining sulphides, one is mainly

composed of pentlandite (36.1 wt% Ni) and the other consists of pentlandite with a contact phase of Ni-Fe alloy (68.0 wt % Ni, 27.6 wt% Fe and 1.50 wt% Co; Table B2) approximating the chemical composition of awaruite (Ni_2Fe to Ni_3Fe). The whole inclusion measured 120 μm in diameter.

3.3.1.3 Websteritic suite

A single orthopyroxene inclusion (KW109b, Table B1) shows an exceptionally low Mg# (56.7), very high CaO (1.43 wt%), and elevated P_2O_5 (0.05 wt%; detection limit =0.02 wt%) and TiO_2 (0.21 wt%) concentrations. The inclusion falls far below the lower cut-off for peridotitic orthopyroxene inclusions at Mg# ~86 (Stachel and Harris 2008) and consequently is assigned to the websteritic suite.

3.3.1.4 Sublithospheric inclusions

Three “eclogitic” garnets recovered from two diamonds (KW50 and 57, Table B1) exhibit a variable majorite component. Based on 24 oxygens per formula unit, the single low-Ca eclogitic garnet contains 6.46 Si cations and has the high concentrations of TiO_2 (1.4 wt%) and Na_2O (0.77 wt%) often seen among majoritic garnets. The two high-Ca (9.3 wt% CaO) eclogitic garnets have a Si cation content of 6.12, which is only marginally elevated, but these garnets also contain high TiO_2 (1.0 wt%) and Na_2O (0.51 and 0.55 wt%). Their Mg# (42.6-42.8) is unusually low for garnets with a majorite component.

3.3.2 REE and trace element compositions of the inclusions

3.3.2.1 Eclogitic suite

For the eclogitic inclusion suite, trace element concentrations were determined on 13 garnets (12 diamonds; Fig. 3.4) and 13 clinopyroxenes (nine diamonds; Fig. 3.5). Three low-Ca garnets exhibit steep positive slopes within the LREE_N that become less steep within the MREE_N-HREE_N, rising from ~0.1-0.2 times chondritic abundance for La to about 20-40 times chondritic level for Lu (Fig. 3.4a). The REE_N patterns for six high-Ca garnets also show steep positive slopes within the LREE but become flat from MREE to HREE at about 10 to 40 times chondritic abundance (Fig. 3.4a). The same distinction in MREE_N-HREE_N slopes for low and high-Ca garnets was previously made by Beard et al. (1996) for eclogite xenoliths from the Mir kimberlite (Siberia). The remaining four high-Ca garnets (with the two garnets from KW81 being indistinguishable; Fig. 3.4b) have very unusual, flat REE_N patterns at about 2 to 20 times chondritic abundance. Mild positive Eu anomalies [geometric Eu/Eu* of 1.21-1.26; defined as $Eu_N / \sqrt{Sm_N \times Gd_N}$] are seen in high-Ca garnets KW79 (positive LREE_N slope and flat MREE_N-HREE_N), KW81a and b (flat REE_N). Similar REE_N patterns are documented for some eclogitic garnet inclusions from the Premier (Cullinan) Mine (Viljoen et al. 2010).

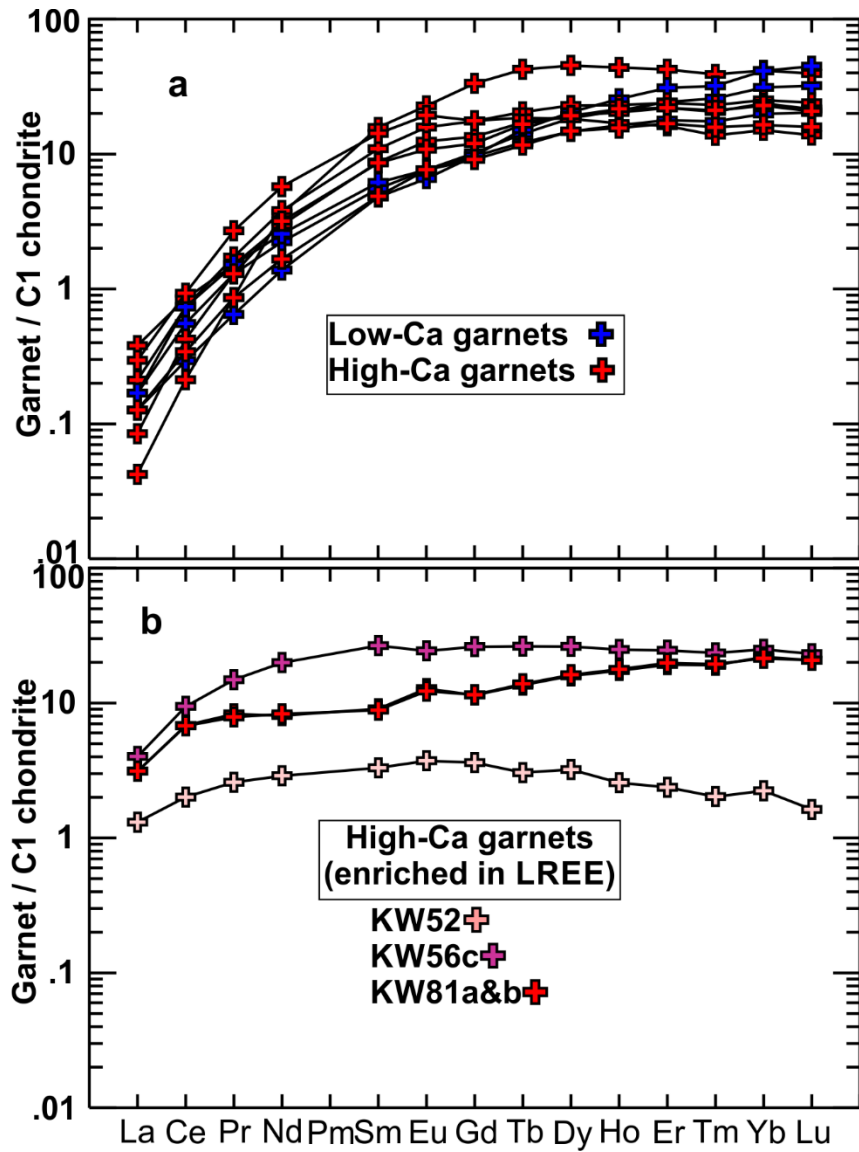


Fig. 3.4 Chondrite normalized (McDonough and Sun 1995) REE patterns for Karowe eclogitic garnet inclusions. **a:** Low-Ca garnets (n=3) and high-Ca garnets (n=6). **b:** Second group of high-Ca garnets with nearly flat REE patterns

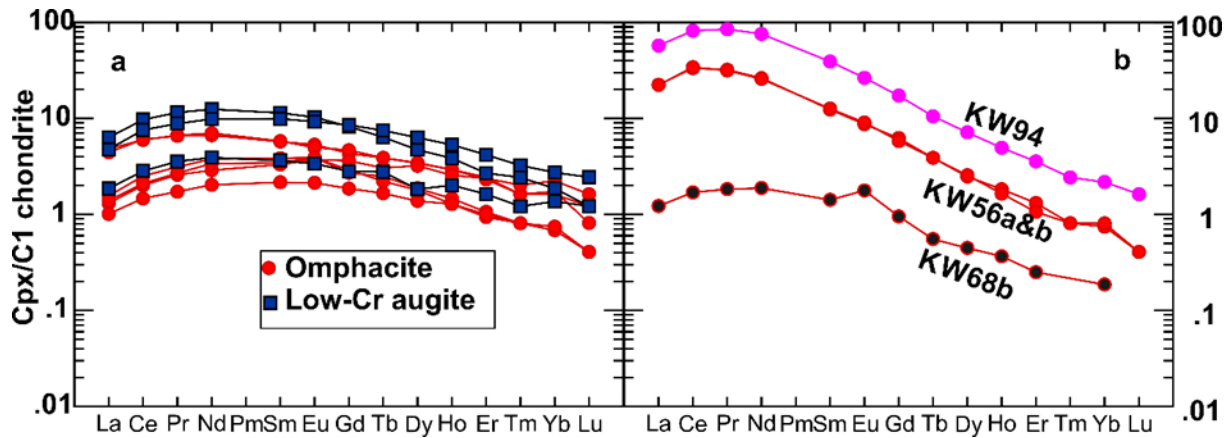


Fig. 3.5 Chondrite normalized (McDonough and Sun, 1995) REE patterns for Karowe eclogitic clinopyroxene inclusions. **a:** Similar, comparatively flat REE_N patterns for omphacites (n=6) and low-Cr augites (n=3). **b:** Four unusual (steeper MREE_N-HREE_N slopes) patterns for omphacitic samples

From the 13 REE_N patterns for clinopyroxenes, six omphacites and three low-Cr augites are characterized by a mild positive slope within the LREE_N and a steady decline within MREE_N-HREE_N from Nd at 2-10 and Lu 0.2-3 chondritic abundance (Fig. 3.5a). Of the remaining omphacitic clinopyroxenes, three have humped patterns, i.e. they show a more pronounced peak in the LREE_N at about 20-90 times chondritic abundances followed by steep negative slopes in MREE_N-HREE_N (Fig. 3.5b). The last omphacite (KW68b) shows the mild positive slope within the LREE_N, as characteristic for the first group, followed by steeply declining MREE_N-HREE_N like the second group (Fig. 3.5b). It is the only clinopyroxene to show a strong positive Eu anomaly (Eu/Eu*=1.51). Mild positive Eu anomalies (Eu/Eu*=1.21) are seen for the two omphacite inclusions from diamond KW65 (showing the mildly sloping REE_N patterns of the first group and coexisting with high-Ca garnet with Eu/Eu* of 1.15).

Eclogitic bulk rock REE_N patterns are calculated for five non-touching pairs of garnet and clinopyroxene (assuming a 1:1 modal abundance ratio; Table B3). Of the three bulk rocks calculated involving high-Ca garnets, two have REE_N patterns sub-parallel to N-MORB with

overall lower REE concentrations and more pronounced depletions in LREE (Fig. 3.6a). The third sample (KW56) shows similar HREE concentrations but is distinctly enriched in LREE (to concentrations greater than N-MORB; Fig. 3.6a). The two pairs involving low-Ca garnets exhibit a gradual increase from LREE_N to HREE_N with N-MORB like HREE (Fig. 3.6b). The overall REE depletion and, in two cases, low LREE/HREE for bulk rocks involving high-Ca garnets are all similar to the observations of Beard et al. (1996) for high-Ca eclogite xenoliths. The negative LREE_N-HREE_N slope for the KW56 bulk rock suggests that at Karowe the eclogitic substrates for the high-Ca group were locally affected by cumulate enriched protoliths with metasomatically added LREE.

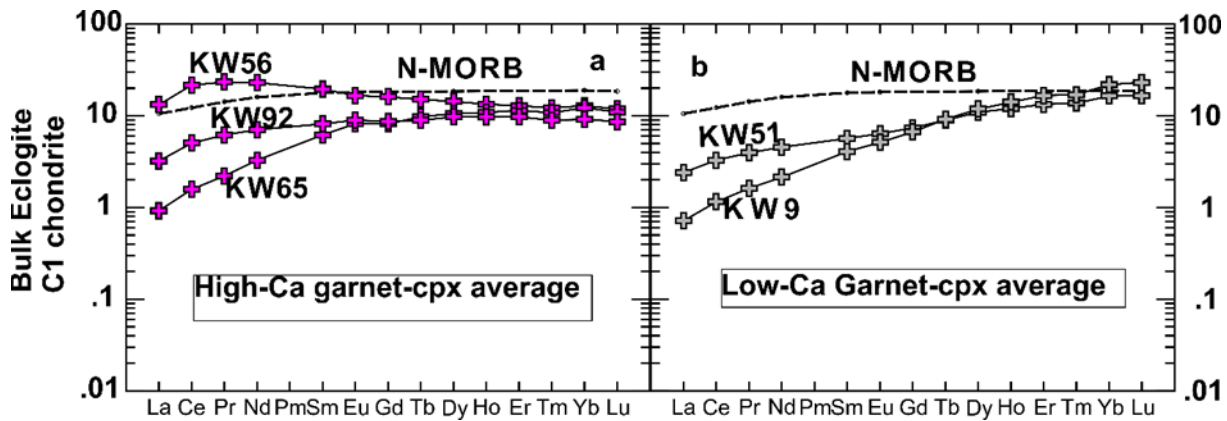


Fig. 3.6 Reconstructed whole-rock REE_N for eclogitic bulk rocks associated with high- and low-Ca garnets (assuming garnet:clinopyroxene=1:1). N-MORB composition is from Sun and McDonough (1989)

3.3.2.2 Peridotitic Suite

Six harzburgitic and one lherzolitic garnet were analysed for trace element contents. Three harzburgitic garnets show typical sinusoidal REE_N patterns peaking in the LREE (Ce-Nd), a low at Dy-Er and steep positive slopes towards Lu (Fig. 3.7a). A fourth sinusoidal pattern is unusual in peaking only in the MREE (at ~10 chondritic abundance for Eu) and having overall super-chondritic MREE and HREE (Fig. 3.7a). The remaining two harzburgitic garnets have

comparatively flat, slightly U-shaped REE_N patterns in the range of 0.3-4 times chondritic abundance (Fig. 3.7a). The single lherzolitic garnet has a normal REE_N pattern with LREE depleted and flat MREE_N-HREE_N at about 4 times chondritic abundance (Fig. 3.7b).

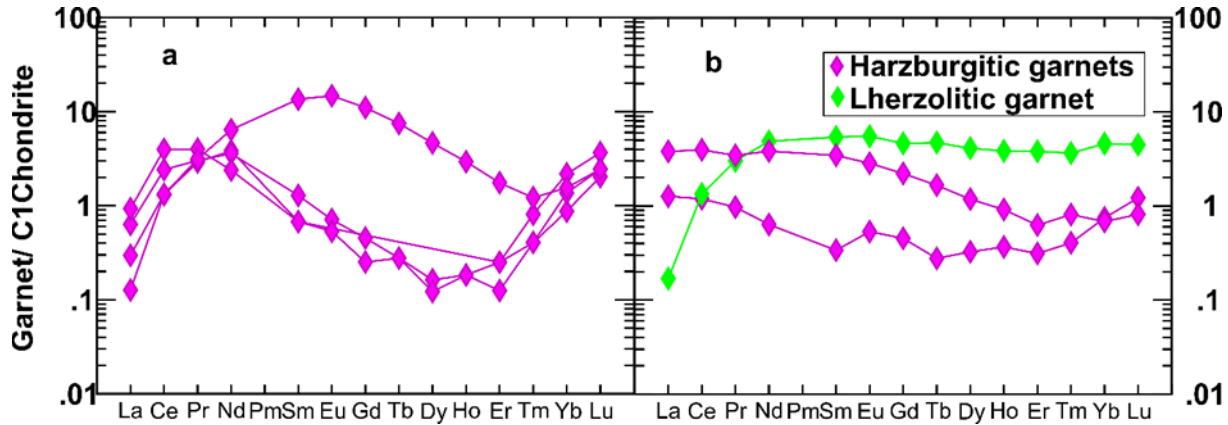


Fig. 3.7 Chondrite normalized (McDonough and Sun1995) REE patterns for Karowe peridotitic garnet inclusions. **a:** Sinusoidal REE_N patterns for harzburgitic garnets. **b:** Two harzburgitic garnets with fairly flat and slightly U-shaped REE_N patterns and a single lherzolitic garnet, showing a normal REE_N pattern

3.3.2.3 Sublithospheric inclusions

The two analyzed majoritic garnets show opposite REE_N patterns (Fig. 3.8): the low-Ca majorite displays a steep negative slope from LREE_N at ~100 times to HREE_N at ~1 times chondritic abundance. The high-Ca majoritic garnet rises from chondritic LREE_N abundance to 300 times chondritic HREE_N.

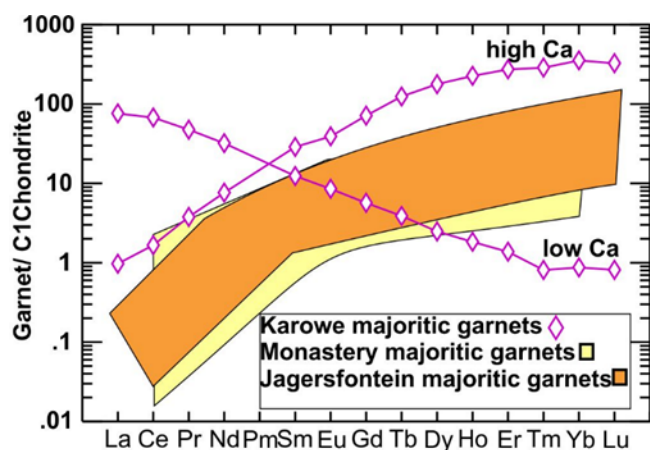


Fig. 3.8 Chondrite normalized (McDonough and Sun 1995) REE patterns of low- and high-Ca majoritic garnets from Karowe compared to majoritic garnets from Monastery (Moore et al. 1991) and Jagersfontein (Tappert et al. 2005)

3.4.3 Geothermobarometry

In ten diamonds two or more mineral inclusion species coexisted that are suitable for the calculation of equilibrium temperatures and/or pressures (Table 3.1). Five non-touching pairs of eclogitic garnet and clinopyroxene yield equilibrium temperatures of 1260-1480 °C, using the Fe-Mg exchange thermometer of Krogh (1988) at a pre-set pressure of 5 GPa. Two pairs involving low-Ca garnets give lower temperatures (1260-1270 °C), compared to three involving high-Ca garnets (1420-1480 °C; Table 3.1). A similar dichotomy is not observed for Orapa, where pairs of clinopyroxene and low-Ca (n=3) or high-Ca garnets (n=6) yield average equilibration temperatures of 1150 and 1160 °C, respectively (calculated from the dataset of Deines et al. 1993 and Gurney et al. 1984). For Letlhakane, only one pair of clinopyroxene and low-Ca garnet was analysed (yielding 1320 °C), the eight pairs involving high-Ca garnets yield an average of 1210 °C (calculated from the data set of Deines and Harris, 2004). A separation into cool (shallow) low-Ca and hot (deep) high-Ca eclogites, therefore, is not a general feature of the lithospheric mantle beneath the Orapa kimberlite cluster.

For the peridotitic suite, one touching (KW86) and three non-touching garnet-olivine pairs (KW31, 69 and 74) give a temperature range of 900-1245 °C (Table 3.1), based on the garnet-olivine thermometer of O'Neill and Wood (1979; calculated at 5 GPa). Diamond KW31, in addition to garnet and olivine, also hosted a non-touching orthopyroxene; application of the garnet-orthopyroxene Fe-Mg exchange thermometer of Harley (1984) yielded a temperature of 1180 °C at pre-set pressure of 5 GPa (Table 3.1), which is within error of the 1245 °C estimate obtained with the olivine-garnet thermometer (O'Neill and Wood 1979). This suggests that olivine, orthopyroxene and garnet in this diamond likely are in equilibrium. Simultaneous estimation of pressure and temperature using garnet-orthopyroxene geothermobarometry (Brey and Köhler 1990; Harley 1984) yields 5.2 GPa and 1200 °C as a condition of inclusion entrapment. Application of the same geothermobarometer combination to a second non-touching garnet-orthopyroxene pair in diamond KW49 gives 4.1 GPa at 950 °C (Table 3.1), resulting in the two samples plotting along a 39-40 mW/m² (Hasterok and Chapman 2011) model geotherm (Fig. 3.9). This result is in very good agreement with the 40 mW/m² paleogeotherm derived by Stiefenhofer et al. (1997) for peridotite xenoliths from the nearby Cretaceous Letlhakane kimberlite. The single lherzolitic clinopyroxene inclusion (KW 93) could not be used for geothermobarometric calculations as it fails the compositional filters of Grütter (2009).

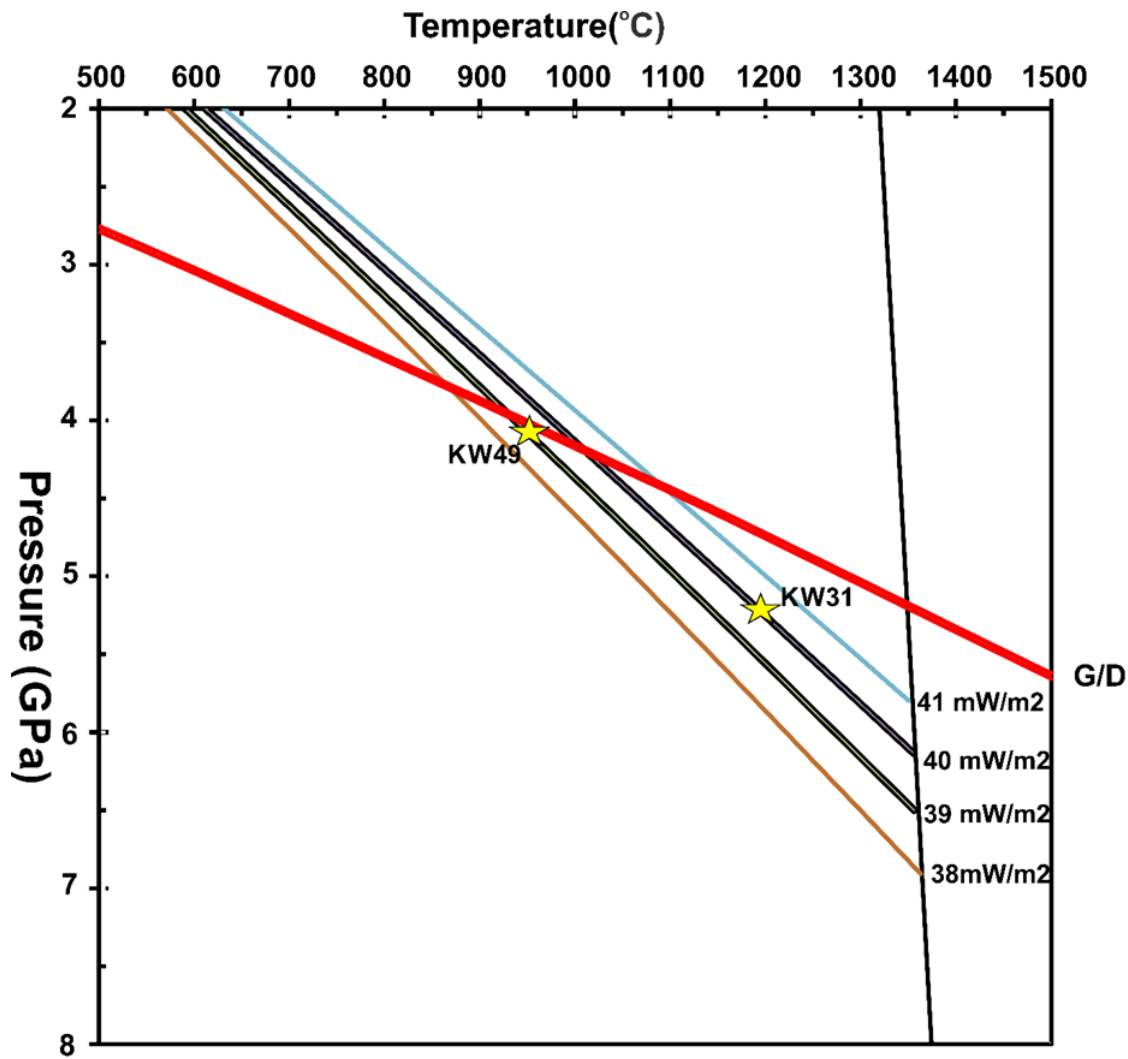


Fig. 3.9 Geothermobarometry results for two non-touching garnet-orthopyroxene pairs calculated using the barometer of Brey and Köhler (1990) barometer combined with thermometer of Harley (1984). Model geotherms for 38-41mW/m² surface heat flow after Hasterok and Chapman (2011), graphite-diamond transition (G/D) from Day (2012). A 40mW/m² Cretaceous paleo-geotherm was derived from mantle xenoliths at Letlhakane (Stiefenhofer et al.1997) and agrees well with the 39-40mW/m² geotherm indicated by Karowe peridotitic inclusions

Table 3.1 Estimated equilibrium pressures and temperatures for coexisting mineral inclusions in Karowe diamonds

Sample #	Paragenesis	Co-existing assemblage	Fe-Mg thermometer	Fe-Mg thermometer	Fe-Mg thermometer	Grt-opx- barometer of	
			Krogh (1988) @ (5GPa)	O'Neill & Wood (1979) @ (5GPa)	Harley (1984) @ (5GPa)	Brey & Köhler (1990) combined with Harley (1984) thermometer	
			T(°C)	T(°C)	T(°C)	P(GPa)	T(°C)
Kw9ab	eclogitic	Low-Ca gt,3cpx	1262				
KW51ab	eclogitic	Low-Ca gt,cpx	1268				
Kw56bc	eclogitic	High-Ca 2gt,2cpx	1480				
Kw65bc	eclogitic	High-Ca gt,2cpx	1420				
Kw92ac	eclogitic	High Ca gt,cpx	1463				
Kw31acd	harzburgitic	2gt,ol, opx		1245	1182	5.2	1196
Kw49ab	lherzolithic	gt,opx				4.1	953
Kw69bc	harzburgitic	gt,2ol		903			
Kw74ac	harzburgitic	gt,2ol		937			
Kw 86a	harzburgitic	2gt,ol		1033			

Based on the Ca-in-opx thermometer (Brey and Köhler 1990), the single websteritic inclusions last equilibrated at 1380 °C. Such a high temperature is not typically associated with diamond formation along steady state cratonic geotherms (Stachel and Luth 2015) but suggests either association with a thermal perturbation (magmatic intrusion) within the lithosphere or derivation from below the lithospheric mantle. Given that this temperature falls within the range observed for eclogitic (non-majoritic) garnet and clinopyroxene pairs from Karowe (see above), a

lithospheric origin appears plausible. Pressure determinations for the three majoritic garnet inclusions from Karowe using the barometer of Beyer and Frost (2017) range between 11 and 14 GPa, clearly implying a sublithospheric origin (Fig. 3.10).

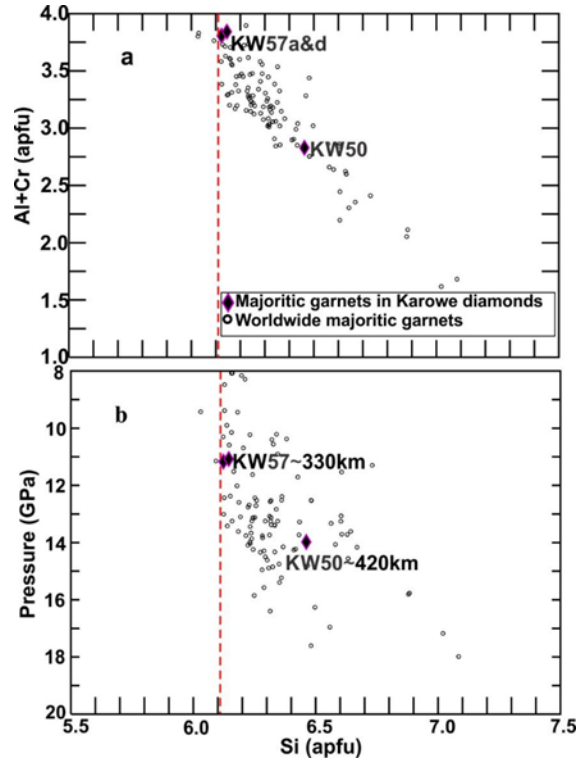


Fig. 3.10 a: Al+Cr versus Si as atoms per formula unit (apfu, with [O]=24) in majoritic garnets inclusions from Karowe and worldwide sources (n=69; database of Stachel and Harris 2008). Red dashed line indicates threshold value of > 6.12 apfu Si used to define majoritic garnets. **b:** Si apfu plotted against pressure (GPa), calculated using the barometer of Beyer and Frost (2017)

3.4 Discussion

Of the 107 inclusion-bearing diamonds studied here, 53 % are eclogitic, 44 % peridotitic, 2 % sublithospheric, and 1 % websteritic. This predominantly eclogitic diamond production at Karowe is similar to the Orapa mine but unlike the predominantly peridotitic productions of the adjacent Letlhakane and Damtshaa mines.

3.4.1 Origin and evolution of eclogitic and websteritic diamond substrates

Eclogitic garnet and clinopyroxene inclusions from Karowe are compositionally variable but for the most part, compare well to previous studies on inclusions in diamonds from the Orapa kimberlite cluster. A comparison of Karowe garnet compositions with other garnets inclusions from the Orapa cluster is shown in Figure 3.11. A websteritic inclusion suite was first recognized in diamonds from the Orapa kimberlite (Gurney et al. 1984) and documents the presence of an unusually wide spectrum of “mafic” diamond substrates in the local lithospheric mantle. This is also evident from the compositions of a large suite of eclogite and pyroxenite xenoliths from the Orapa (Aulbach et al. 2017). In Karowe, the presence of orthopyroxene-bearing (websteritic) substrates is evidenced by a single enstatite inclusion with low Mg# (57). Possible saturation in orthopyroxene may also be indicated by Ca# as low as 21.5 in augite inclusions with elevated Cr, Ni, and Mg contents. Mineralogical variability in the eclogitic substrates is also highlighted by the occasional presence of kyanite and coesite inclusions. Kyanite occurs in Group I diamondiferous eclogites from Orapa (Shee and Gurney 1979) and was recently described in Group II diamond-free eclogites by Aulbach et al. (2017). It is a characteristic phase of aluminous eclogites in general (Spetsius 2004; Shu et al. 2016).

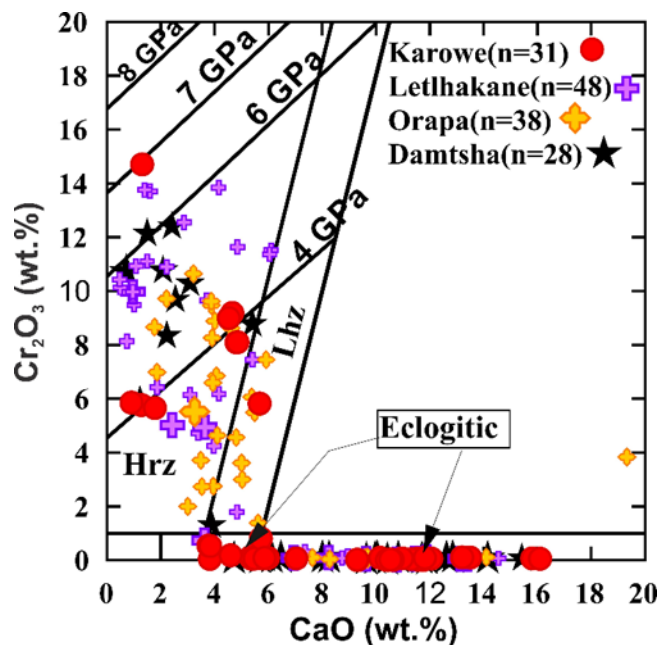


Fig. 3.11 Cr₂O₃ vs CaO diagram for garnets inclusions in diamonds from Karowe (n=31) and nearby localities (Deines and Harris, 2004; Deines et al.2009; Stachel et al.2004b). Isobars are from Grütter et al. (2006)

The REE characteristics (bulk rock LREE_N/HREE_N generally <1; presence of positive Eu anomalies in some high-Ca garnets and coexisting clinopyroxenes) are consistent with a derivation of Karowe low- and high-Ca eclogitic diamond substrates from subducted protoliths. Moderate positive Eu anomalies in two of the calculated bulk rocks involving high-Ca garnets (Fig. 3.12) suggest cumulate enriched protoliths for these samples (e.g., Aulbach and Viljoen 2015). The absence of distinct positive Sr anomalies for the same calculated bulk rocks (Fig. 3.12), however, indicates decoupling of Sr and Eu/Eu*. A decoupling of Sr content and Eu/Eu* is also observed for garnet inclusions in diamonds world-wide and was related to Sr depletion during secondary partial melting events (Stachel et al. 2015). Positive Sr anomalies without paired Eu anomalies in the two calculated low-Ca group bulk rocks (Fig. 3.12) again show decoupling of Sr content and Eu/Eu*. Positive slopes from MREE to HREE (Yb_N/Gd_N=2.2-3.3) indicate that the protoliths of

the low-Ca eclogitic diamond substrates likely experienced partial melting and associated depletion in LREE (Fig. 3.6), followed by metasomatic re-enrichment in Sr (Aulbach et al. 2017). Estimated bulk rock Mg# of 61-72 are on the high side of average present-day N-MORB (~60; Floyd 1991) and could be inherited from gabbroic protoliths (Aulbach and Jacob 2016) or again reflect a secondary melting extraction event.

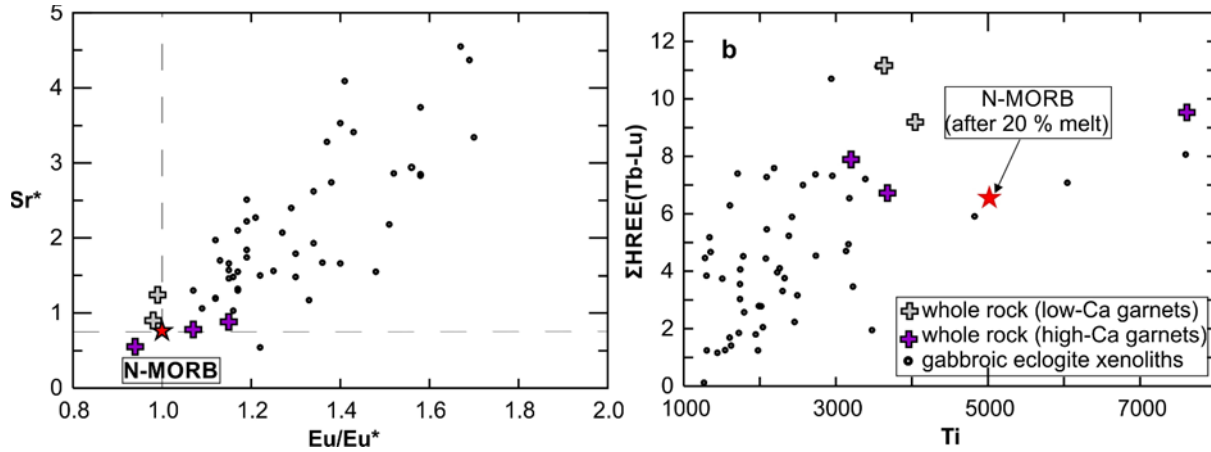


Fig. 3.12 The relationship between (a) Sr* and Eu/Eu* and (b) between Σ HREE (Tb-Lu) and Ti in eclogitic whole rock compositions reconstructed from Karowe inclusions and calculated whole rocks of gabbroic eclogite xenoliths from Orapa (Aulbach et al. 2017). The HREE concentrations of N-MORB after 20% melt extraction, calculated assuming a modal clinopyroxene-garnet ratio of 1:1 are from Stachel et al. (2004a), Ti was calculated using partition coefficients from Klemme et al (2002). Sr* is $Sr_N / (0.5 \times Pr_N + 0.5 \times Nd_N)$ and Eu/Eu* is $Eu_N / \sqrt{Sm_N \times Gd_N}$

Combining the observed variability in the major element compositions of garnet and clinopyroxene inclusions with the range of bulk rock REE_N patterns indicates that a large cross section of oceanic crust (not necessarily related to a single subduction event) was sampled. Beard et al. (1996) suggested an origin of high-Ca eclogites as cumulate-enriched rocks of the deeper oceanic crust (causing overall REE depletion increasing towards the LREE) and low-Ca eclogites as upper oceanic crust (with relatively unfractionated REE). At Karowe, the presence of positive

Eu anomalies only in high-Ca garnets and associated clinopyroxenes is consistent with this model. Subsequent modification during partial melting in the garnet stability field (LREE loss; Foley et al. 2002; Jacob 2004), metasomatic modification (LREE addition; Ireland et al. 1994) and interaction with mantle peridotite (adding Cr and Mg; Smart et al. 2009) may all have acted to increase the compositional variance further and, in combination, cause compositionally diverse eclogitic to pyroxenitic diamond substrates beneath Karowe.

3.4.2 Peridotitic diamond substrates in the lithospheric mantle beneath Karowe

Peridotitic olivine inclusions in Karowe diamonds have high Mg# with a mean and median of 93.1, comparable to olivine inclusions from elsewhere in the Orapa cluster (e.g., Deines et al. 2009) and harzburgitic olivine inclusions worldwide (mean: 93.2; Stachel and Harris 2008). Such high forsterite contents imply the presence of peridotitic mantle sources that experienced primary melt extraction approaching and exceeding the exhaustion of orthopyroxene (Bernstein et al. 2007). Two Karowe olivines with normal Mg# have unusually low NiO contents (mean of 0.26 wt% as opposed to 0.36 wt% worldwide; Fig. 3.3). Unusually low Ni contents were shown to occur in olivine inclusions that originated as ringwoodite in equilibrium with ferropericlasite in the lower transition zone (Brey et al. 2004). However, the two low-Ni olivines from Karowe have low P₂O₅, Cr₂O₃ and Na₂O, inconsistent with a superdeep origin, and in one case (KW31) occur in apparent equilibrium with normal lithospheric inclusions (harzburgitic garnet and orthopyroxene).

Peridotitic garnet inclusions from Karowe are dominantly (~90 %) harzburgitic and almost half have CaO contents < 1.8 wt%, i.e. likely originating from primary residues that were molten beyond the point of orthopyroxene exhaustion (Grütter et al. 1999). One of the low-Ca garnets has a very high Cr₂O₃ content (14.7 wt%) that implies that at the time of diamond formation

highly depleted cratonic lithosphere extended down to at least 220 km depth (equivalent to 7 GPa pressure; Fig. 3.2; Grütter et al. 2006) beneath Karowe. These observations establish that the lithospheric mantle beneath Karowe, at least at the time of peridotitic diamond formation, was strongly depleted in easily fusible components and very thick, similar to the southern part of the Zimbabwe Craton (Smith et al. 2009). REE_N patterns for harzburgitic garnets (sinusoidal to slightly U-shaped) and the one lherzolitic garnet (normal REE_N) are very distinct and imply different styles of metasomatic re-enrichment: fluid metasomatism for the harzburgitic and melt metasomatism for the lherzolitic substrates (Stachel et al. 2004a). The Y and Zr concentrations of these garnets (Fig. 3.13) are consistent with this conclusion: all but one harzburgitic garnet plot in the depleted field but clearly define a trend that leads into the field for low temperature, fluid-style metasomatism. Whereas the single lherzolitic garnet documents a much higher Y/Zr ratio, consistent with melt metasomatism. Very similar garnet REE_N patterns to those observed at Karowe (sinusoidal and slightly U-shaped for harzburgitic and normal for the one lherzolitic garnet) and metasomatic styles (fluid metasomatism for harzburgitic and melt metasomatism for lherzolitic garnets) were also documented for peridotitic garnet inclusions in diamonds from Orapa (Fig. 3.13; Stachel et al. 2004b).

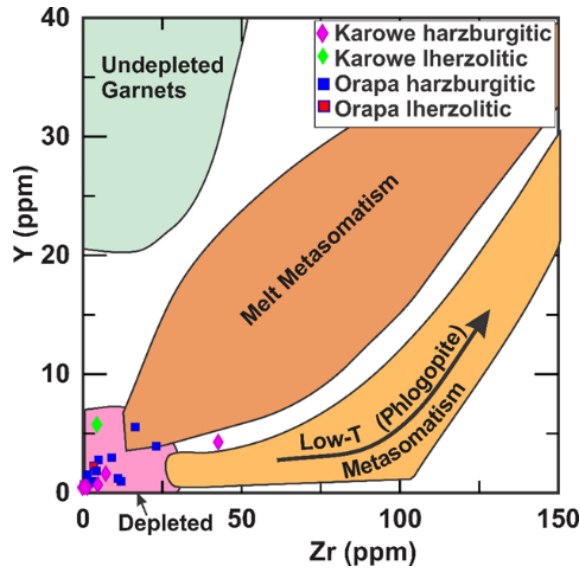


Fig. 3.13 Y versus Zr for harzburgitic and lherzolitic garnet inclusions from Karowe and from Orapa (Stachel et al. 2004b). Main compositional fields and trends shown are for garnet xenocrysts from Griffin and Ryan (1995)

The presence of a Ni-Fe alloy inclusion (intergrown with pentlandite) indicates that, at least locally, fO_2 conditions as reducing as the iron-wüstite buffer occurred in the peridotitic diamond substrates. Generally, such reducing conditions are not observed within lithospheric mantle, even for cratons of similar depth extent (Stagno et al. 2013), and hence are interpreted as a localized environment rather than widespread metal saturation in the deep mantle lithosphere below the Zimbabwe Craton.

3.4.3 Sublithospheric substrates

Pressure determinations for the three majoritic garnet inclusions from two Karowe diamonds place their origin in the deep asthenosphere and uppermost transition zone (between 330 and 420 km depth; Fig. 3.10b). Based on their low-Cr character (cut-off at $Cr_2O_3 < 1$ wt%; Schulze 2003), the majoritic garnets all derive from eclogitic substrates. Kiseeva et al. (2013) reported that despite

their overall eclogitic mineral compositions, such majoritic garnets can follow (1) a substitution mechanism ($2\text{Al}^{3+}=\text{Si}^{4+}+\text{M}^{2+}$) that is characteristic for peridotitic (and pyroxenitic) substrates or (2) a substitution mechanism (eclogitic trend) accommodating the jadeite component of omphacitic clinopyroxene ($\text{M}^{2+}+\text{Al}^{3+}=\text{Na}^{+}+\text{Si}^{4+}$). The first substitution (pyroxenitic trend) is interpreted to reflect sublithospheric diamond formation through interaction of slab-derived magnesio-carbonatitic melt and adjacent pyrolytic mantle (Kiseeva et al. 2016, Walter et al. 2008). At Karowe, the low-Ca majoritic garnet in diamond KW50 shows an excess in $\text{Mg}+\text{Ca}+\text{Fe}+\text{Mn}$ over the number of available X-sites in garnet and thus falls onto the pyroxenitic trend, while the two high-Ca majoritic garnets in KW57 fall onto the Na-majorite trend (Harte 2010; Kiseeva et al. 2013). The low-Ca majoritic garnet has an elevated Cr_2O_3 content (0.18 wt%) and $\text{Mg}\#$ (66.2), consistent with the pyroxenitic connection suggested by Kiseeva et al. (2013 and 2015), whilst the two high-Ca garnets contain Cr below the limit of detection and have low $\text{Mg}\#$ (average of 42.7), indicative of a typical eclogitic bulk rock composition (Harte 2010). This clear separation into two modes of majorite formation is reflected in highly distinct REE_N patterns for low- and high-Ca majoritic garnets (Fig. 3.8). The low-Ca garnet exhibits a melt-like pattern characterized by strong LREE enrichment and a steeply negative slope from LREE_N to HREE_N . Based on the majorite-melt partition coefficients of Yurimoto and Ohtani (1992), the REE_N pattern of a calculated melt in equilibrium with the low-Ca garnet would show a steep decline from 540 times chondritic La to chondritic Yb abundance. The high-Ca garnet has the reverse pattern with a steep positive LREE_N - HREE_N slope. Although more enriched in HREE, the high-Ca garnet REE_N pattern is similar to those displayed by eclogitic majoritic garnets from Monastery (Moore et al. 1991) and Jagersfontein (Tappert et al. 2005; Fig. 3.8). The strong HREE enrichment would be consistent

with the high-Ca garnet crystallizing in a residuum that yielded a melt similar to that forming the low-Ca majoritic garnets.

Karowe Mine produces large to extremely large gem-quality diamonds that are nitrogen “free” Type IIa or Type IaB containing low contents of completely aggregated nitrogen (D’Haenens-Johansson et al. 2017). Smith et al. (2016) studied large Type IIa diamonds from several sources and found that they exclusively contained inclusions of sublithospheric origin, including majoritic garnets. Inclusions of sublithospheric origin have not previously been reported in diamonds from the Orapa kimberlite cluster. The two majoritic garnet-bearing diamonds from Karowe reported here are not Type IIa but have very low to moderate nitrogen contents of highly aggregated nitrogen (30 and 250 at.ppm with 95 and 86 %B respectively). Nevertheless, their discovery shows that sublithospheric diamond sources were tapped by the Karowe kimberlite, an indication that the very large diamonds from this mine also formed at below the lithosphere, as observed elsewhere by Smith et al. (2016).

3.5 Conclusions

The major element composition of inclusions in Karowe diamonds establishes their derivation from four distinct mantle lithologies present below the western edge of Zimbabwe Craton. More than half of the diamond population is eclogitic (53 %), followed by peridotitic (44 %), sublithospheric (2 %) and websteritic (1 %). Overall, the composition of the eclogitic and peridotitic inclusions compares well with the results of previous studies conducted on other localities in the Orapa kimberlite cluster (on diamonds from Orapa, Damtshaa and Letlhakane). The eclogitic diamond substrates beneath Karowe are highly diverse, ranging from typical basaltic to cumulate-like protolith compositions. This variety is documented in the variance of calculated

bulk rock Mg# (61-72) and the broad range in the jadeite component (14-48 mol%) in eclogitic clinopyroxenes as well as the presence of three kyanite inclusions. In combination with calculated bulk rock REE patterns, the variable inclusion chemistry documents derivation of eclogitic diamonds from a range of protoliths that represent both shallow and deep oceanic crust, in part modified by partial melting during subduction and subsequent metasomatism. About 40 % of eclogitic clinopyroxenes are augites with elevated contents of Cr, Ni and Mg at unusually low Ca contents, which may represent an association transitional to pyroxenites. A single websteritic orthopyroxene inclusion confirms the presence of pyroxenitic diamond substrates beneath Karowe that were also recognized at Orapa.

The peridotitic inclusion suite documents a predominance of typical, highly depleted diamond substrates of harzburgitic to dunitic paragenesis along the western margin of the Zimbabwe Craton. Very high Cr₂O₃ in one of the low-Ca peridotitic garnets is indicative of a depth extent of this highly depleted cratonic lithosphere to at least 220 km depth at the time of diamond formation.

The discovery of sublithospheric (eclogitic majoritic garnet) inclusions in Karowe diamonds sets this mine apart from other deposits in the Orapa kimberlite cluster and may provide a key link to the regular recovery of exceptionally large diamonds at Karowe. Low-Ca and high-Ca majoritic garnets follow two distinct trends of majoritic substitution (pyroxenitic and eclogitic trend, respectively). These distinct origins are consistent with their REE_N patterns being mirror images: (1) high LREE and low HREE for the low Ca-garnet, suggested to relate to melt-aided slab-pyrolite interaction and (2) low LREE and high HREE for the high-Ca garnet, which formed in substrates representing basaltic protoliths that lost a partial melt similar to that reflected in the low-Ca majorites.

Chapter Four

4.0 Physical characteristics, nitrogen content and carbon isotope composition of diamonds from the Karowe Mine in Botswana

4.1 Introduction

The Karowe kimberlites, located in north-eastern Botswana, produce some of the world's largest diamonds, such as the 1,109 carat Lesedi la Rona and the 812 carat Constellation. Non-destructive gemmological and spectroscopic studies on the Constellation and two smaller Karowe diamonds weighing 296 and 183 carats, (D'Haenens-Johansson et al. 2017), showed that these diamonds had poor shape, exceptional colour (D-colour, the highest colour grade) and nitrogen contents ranging from below the limit of detection (Type II) to low concentrations of fully aggregated nitrogen (Type IaB).

These exceptional diamonds represent rare samples from the coarse end of the size-frequency distribution at Karowe and are not available for destructive scientific analysis. We therefore, focus on diamonds in the 1 to 3 mm size range, which represents the bulk of production, to study the characteristics of Karowe diamonds in the context of their parageneses, as determined via mineral inclusions by Motsamai et al. (2018). Based on this study, 53% of Karowe diamonds are derived from eclogitic sources, 44% are peridotitic, 1% are websteritic and 2% have a sublithospheric origin (Motsamai et al. 2018). The occurrence of superdeep mineral inclusions provides a possible link between the small diamonds studied here and the above mentioned very rare large diamonds, as it agrees with the recent observation that large Type II diamonds generally originate from the sublithospheric mantle (Smith et al. 2016). Here we analyse the crushed diamond fragments from the inclusion study of Motsamai et al. (2018) to determine their nitrogen contents and carbon isotope compositions, the main goal being to evaluate the nature of the

diamond-forming fluids, their possible sources and how the different fluids affect the growth history of Karowe diamonds.

4.1.1 Geological context

The Karowe Mine exploits three coalesced kimberlite pipes (north, central and south lobes) of Cretaceous age (Davis 1977) within the so-called Orapa kimberlite cluster. This cluster consists of more than 81 kimberlite bodies (Brook 2012) in northern Botswana, all situated along the western edge of the Zimbabwe craton.

The majority of studied inclusion-bearing diamonds from the principal mines in the Orapa cluster (Orapa, Letlhakane and Damtshaa) have previously been analysed for their nitrogen contents, nitrogen aggregation states as well as their carbon isotope compositions. Due to a high proportion of yellow/white cube diamonds with nitrogen concentrations above 1000 at.ppm (Deines et al. 1993; Deines et al. 2009), Orapa mine diamonds contain significantly higher nitrogen contents than diamonds at both Letlhakane and Damtshaa. The average degree of nitrogen aggregation (%B) for diamonds from the three mines is relatively small, Orapa 40 ± 20 %B, Letlhakane 43 ± 21 %B, Damtshaa 32 ± 20 %B, (Deines et al. 2009). The carbon isotope compositions of the diamonds from all three mines show broad ranges: Orapa ranging from -22.4 ‰ to -2.6 ‰ (Deines et al. 1993), Letlhakane varying from -21.0 ‰ to -3.0 ‰ (Deines and Harris 2004) and Damtshaa from -18.0 ‰ to -4.0 ‰ (Deines et al. 2009). In addition, distinct diamond growth events separated in time have been recognised through isotopic dating of eclogitic silicate inclusions and through cathodoluminescence (CL) images of diamonds from Orapa and Letlhakane (Timmerman et al. 2017; Chinn et al 2018).

4.2 Samples and Analytical Methods

The diamond chips analysed for this study are derived from 120 inclusion-bearing diamonds which were crushed in order to release mineral inclusions. Diamonds were selected from the run-of-mine production at the sorting office of the Karowe Diamond Mine in Gaborone, Botswana. The collected diamonds range in size from about 2 to 3 mm (equivalent to -7+5, -9+7, and -11+9 Diamond Trading Company sieve classes). The diamonds were visually inspected under a binocular microscope and fully documented for shape, colour and surface features before being photographed.

4.2.1 Fourier transform infrared (FTIR) spectroscopy

Infrared spectra were acquired for 240 diamond fragments, which were typically ~1 mm wide and 0.1 to 0.2 mm thick. Where possible, two diamond chips representing both the inner and outer regions of a single diamond were selected. These were analysed using a Thermo Scientific Nicolet FTIR spectrometer fitted with a Nicolet Continuum infrared microscope. Two hundred scans were collected for 120 seconds over the mid-infrared range (4000 to 650 cm^{-1}), with a spectral resolution of 4 cm^{-1} . The instrument was purged with a dry mixture of nitrogen and oxygen. In addition, a background spectrum (also 200 scans) was collected every two to three hours and subtracted from each measured spectrum. All spectra were first baseline-corrected, and then normalised to 1 cm sample thickness by subtracting a pure Type IIa diamond spectrum. Deconvolution into A, B, and D components was achieved using the Excel program CAXBD97, developed by David Fisher (De Beers Technologies, Maidenhead, UK). The concentration of nitrogen in A and B centers can be estimated from the absorption coefficients at 1282 cm^{-1} : $[\text{N}_A]=16.5\times\mu\text{A}$ (Boyd et al. 1994) and $[\text{N}_B]=79.4\times\mu\text{B}$ (Boyd et al. 1995). Nitrogen aggregation is expressed as $\%B =$

$100 \times [N_B] / ([N_A] + [N_B])$. The intensities of other peaks of interest (the platelet peak at 1358 to 1372 cm^{-1} and a hydrogen-related peak at 3107 cm^{-1}) were measured using the peak area tool of the OMNICTM software which involves a local baseline correction. Limits of detection for nitrogen vary but are generally in the range of 5 to 15 at.ppm, with errors typically in the range of 5 to 10 % of the total nitrogen concentration

4.2.2 Cathodoluminescence (CL) imaging and secondary ion mass spectrometry (SIMS)

Based on the quality of FTIR spectra (e.g. low spectral noise and a nearly straight baseline), 119 diamond fragments (mostly from the inner zones of individual diamonds) were selected for carbon isotope analysis and nitrogen abundance measurement using a multi-collector ion microprobe spectrometer (MC-SIMS). Samples were placed into three 25 mm mounts along with a natural diamond reference material (SO270) and a vitreous carbon reference material (SO233A). The mounts were coated with 5 nm of Au prior to imaging using a Zeiss EVO MA15 scanning electron microscope (SEM) operating at 15 kV and 3 – 5 nA beam current. CL images were obtained using a parabolic mirror coupled to a high-sensitivity and broadband photomultiplier detector. Subsequently, the mounts were coated with an additional 35 nm Au film for SIMS analysis.

Carbon isotope ($^{13}\text{C}/^{12}\text{C}$) compositions and nitrogen abundances were determined in separate sessions using a Cameca IMS-1280 multi-collector ion microprobe, following methods and reference materials detailed by Stern et al. (2014) with slight modifications as noted here. Primary beam conditions included the use of 20 keV $^{133}\text{Cs}^+$ ions focused to a beam diameter of $\sim 12 \mu\text{m}$ and beam currents of 1.0 - 1.75 nA. The primary beam was rastered across a $18 \times 18 \mu\text{m}$ area prior to analysis to clean the surface of Au contaminants and to implant Cs. Carbon isotope

ratios were analysed first followed by nitrogen abundance measurements on the same analytical spot.

MC-SIMS collection conditions for carbon isotope analyses included an entrance slit width of 110 μm , field aperture of 5 x 5 mm, a field aperture-to-sample magnification of 100 x, and a fully-open energy slit. Both $^{12}\text{C}^-$ and $^{13}\text{C}^-$ were analysed simultaneously in Faraday cups (L'2 using $10^{10} \Omega$ amplifier, and FC2 with $10^{11} \Omega$) at mass resolutions of 2000 and 2900, respectively. Mean count rates for $^{12}\text{C}^-$ and $^{13}\text{C}^-$ were typically 1.0×10^9 and 1.0×10^7 counts per seconds, respectively, collected over a 75 seconds counting interval. Total spot-to-spot analysis time (including pre-analysis raster, automated secondary ion tuning and peak counting) for each measurement was 220 seconds. The analytical sequence for carbon isotope measurements interspersed measurements of unknowns with analyses of the diamond reference material S0270, having a $\delta^{13}\text{C}_{\text{VPDB}} = -8.88 \pm 0.10 \text{ ‰}$ in a 4:1 ratio. Instrumental mass fractionation (IMF) for $^{13}\text{C}^- / ^{12}\text{C}^-$ was determined from utilizing all the replicate analyses of S0270 for three sessions (N= 56, 57, 60), where the standard deviation of the $^{13}\text{C}^- / ^{12}\text{C}^-$ values was 0.04 ‰ – 0.07 ‰, after corrections for systematic within-session IMF drift of $\leq 0.3 \text{ ‰}$ over several hours. Uncertainties of individual $\delta^{13}\text{C}_{\text{VPDB}}$ analyses propagate within-spot ($\sim 0.05 \text{ ‰}$, 1σ), between-spot (0.05 ‰, 1σ , blanket assigned), and between-session errors (0.01 ‰, 1σ), and are typically $\pm 0.14 \text{ ‰}$ (2σ). The spot uncertainties exclude the error in the value of the reference material reported above, which can be added as appropriate for comparisons with other data, but which would otherwise mask real differences among the diamonds analysed here.

For nitrogen abundances, secondary ion collection conditions utilized a field magnification of 133 times, an entrance slit width of 45 μm , field aperture of 3 x 3 mm, and energy slit width of 40 eV transmitting low-energy ions. The molecular ions [$^{12}\text{C}^{13}\text{C}^-$] and [$^{13}\text{C}^{14}\text{N}^-$] were

measured simultaneously using a Faraday cup–electron multiplier combination (L'2 using $10^{10} \Omega$ amplifier and EM axial detector, respectively) at mass resolutions of 5800 and 5500, respectively, sufficient to resolve any potential spectral interferences. Electron multiplier counts were corrected for background and dead-time (46 ns). The $[^{13}\text{C}^{14}\text{N}]^-/[^{12}\text{C}^{13}\text{C}]^-$ ratios in unknowns and S0270 diamond reference material were analysed in the same sequence as for C-isotopes. The sensitivity factor for $[^{13}\text{C}^{14}\text{N}]^-/[^{12}\text{C}^{13}\text{C}]^-$ was determined from analysing diamond reference material S0280E, having a N abundance of 1670 at.ppm ($\pm 5 \text{ ‰}$ absolute, 2σ), located on a separate mount. The uncertainties in the N abundance measurements include within-spot, between-spot, and between-session errors, but exclude the absolute error, which can be added as required for external comparisons.

4.3 Results

4.3.1 Physical characteristics

Table 4.0 outlines the relationship between shape and colour for the 120 studied diamonds. One hundred four diamonds are classified as colourless covering the whole range of diamond shapes noted. Only octahedra, transition forms and aggregates have a light brown component. Transparent green coated diamonds have a higher abundance of macles ($n=3$) and a single pseudo-hemimorphic diamond being involved. Nothing unusual is noted in the shape versus colour relationship.

The octahedral population is dominated by sharp-edged or slightly rounded regular crystals (75 %), with the remaining 25 % consisting of broken octahedral shapes. Surface features for both groups consist of slightly resorbed growth forms such as shield-shaped and serrate laminae, imbrication patterns as well as etch features such as negative flat bottomed trigons and etch pits (Fig. 4.0). In addition, a unique surface texture sometimes occurs among the Karowe

diamonds: an imbricated pattern intermediate between terraces and hillocks that results from the resorption of stacked growth layers (Fig.4.0 e and f).

Table 4.0 Morphologies and colours observed in inclusion-bearing diamonds from Karowe.

Morphology	Number of diamonds		
	Colourless	Light brown	Transparent green coated
Octahedra	32	2	2
Rounded dodecahedra	12		
Transitional habit between octahedra and rounded dodecahedra	18	2	1
Cubo-octahedra	5		
Macles	21		3
Aggregates	15	2	2
Pseudo-hemimorphic	1		1
Total	104	6	9

A significant proportion (18 %; Fig. 4.1) of formerly octahedral diamonds exhibit resorption, resulting in a habit transitional between octahedra and rounded dodecahedra (e.g., Robinson 1979; Tappert and Tappert 2011; Stachel 2014). In the present case, the transition is defined by the relative proportion of residual octahedral (o) and resorbed dodecahedral (d) faces on a diamond (o/d =moderately resorbed, d/o strongly resorbed; see Table C1 in Appendix C). Surface features present depend on where the diamond is in the octahedral-dodecahedral transition. Octahedral faces show shield shaped laminae due to the rounding of originally stacked growth layers and also flat bottomed trigons. Nearer the dodecahedral end of the transition, plastic deformation lines, terracing, shallow depressions and hillocks are evident.

Macles (spinel-law octahedral twins) make up 20 % of the inclusion-bearing diamonds at Karowe (Fig. 4.1). A triangular shape and the presence of a visible twin plane were used to distinguish them from flattened octahedral crystals. Most crystals have rounded edges, due to resorption, a process whereby primary octahedral macles become rounded dodecahedra or so-called dodecahedral macles (see Tappert and Tappert 2011). Surface features on the complete or partial octahedral macle faces include serrate or simple shield shaped laminae and trigons. The resorbed parts of these macles exhibited terraces, hillocks and shallow depressions (see Tappert and Tappert 2011). Some broken macles have irregular shapes but, in general, showed similar surface patterns as described above for both macles and octahedral surfaces.

The 16 % of aggregated diamonds consist of two to three intergrown crystals with either octahedral or dodecahedral morphologies. They display the same surface features as the single crystals described above.

Five diamonds were identified as cubo-octahedra on the basis of rounded cube faces with tetragons and rounded octahedral extensions emanating from some cube corners. The cube and octahedral faces grew simultaneously and similar diamonds have been described by Welbourn et al. (1989) from the Jwaneng mine in Botswana.

Two diamonds show rounded dodecahedral morphologies on one side of the crystal while the other side exhibits an octahedral shape with minor resorption (rounded edges). Such uneven resorption is termed pseudo-hemimorphism (Robinson 1979) and relates to partial enclosure and protection of diamonds in mantle xenoliths

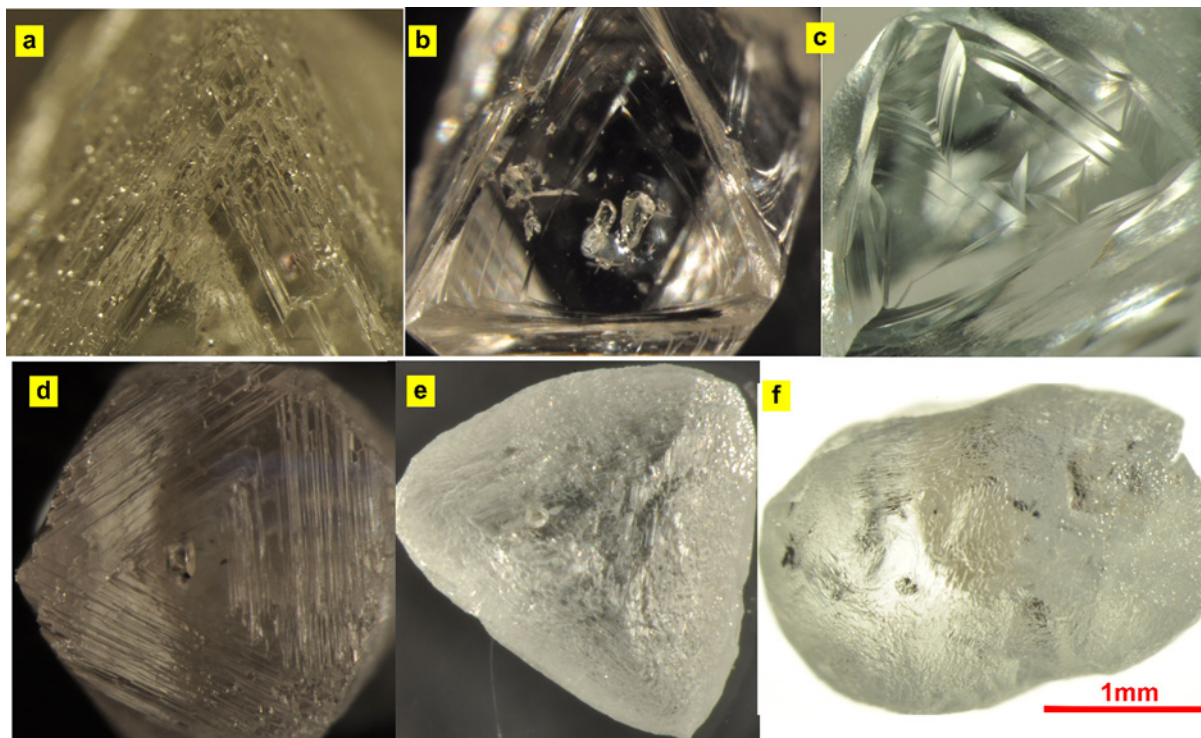


Fig. 4.0 Some of the surface features on octahedral crystal faces of Karowe diamonds: (a) serrate laminae, (b) shield-shape laminae, (c) shield-shape laminae and pyramidal trigons as well as flat-bottomed negative trigons (d) stacked octahedral growth layers pattern, and (e, f) due to resorption intermediate patterns are formed, causing the development of a unique surface texture transitional between terraces and hillocks

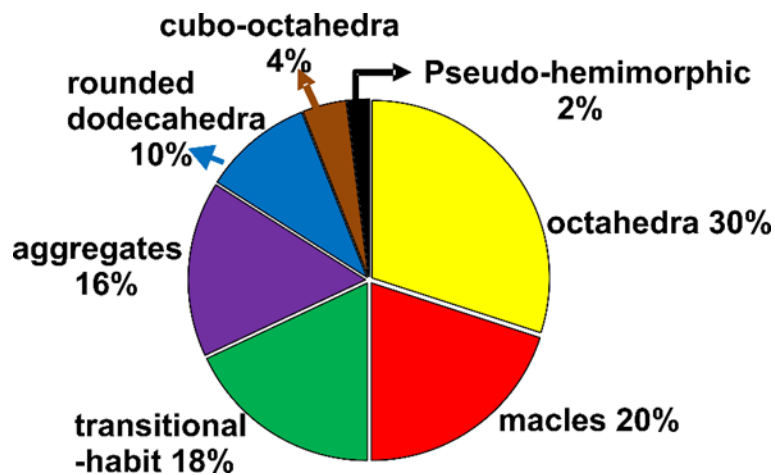


Fig. 4.1 Pie chart showing the relative proportions of diamond habits among Karowe diamonds

4.3.2 Nitrogen contents and nitrogen aggregation states

Based on the presence or absence of nitrogen detectable with FTIR, diamonds are divided into Type I and II (Robertson et al. 1934; Breeding and Shigley 2009). Type I diamonds are further subdivided into Type Ib, containing single substituted nitrogen atoms (C-centers), and Type Ia containing aggregated nitrogen in two forms, the A-centre (two nitrogen and known as Type IaA) and B-centre (four nitrogen around a lattice vacancy and known as Type IaB).

FTIR analysis of the nitrogen concentrations in 119 broken Karowe diamonds varies from below the limit of detection (~ 15 at.ppm), for three Type II diamonds (2 %) up to 1217 at.ppm, for the remainder (Table C1). The average nitrogen content is 378 at.ppm with a median of 291 at.ppm. Figure 4.2a shows the nitrogen distribution to be polymodal, with a main concentration mode at <100 at.ppm and minor modes at ~ 700 and 900 at.ppm. A comparison with Fig. 4.2b, which outlines the nitrogen distribution for the inclusion-bearing diamonds in the Orapa cluster (Orapa, Letlhakane and Damtshaa), shows a similar distribution to that of Karowe. The two pieces analysed for most broken diamonds typically recorded similar average nitrogen contents, with average nitrogen concentrations from the innermost part [400 ± 315 at.ppm (1σ)] being slightly higher than those from the outer part [372 ± 293 at.ppm (1σ)]. Significant decreases in nitrogen concentration from core to rim have been reported previously for other locations (Bulanova et al. 2002; Smart et al. 2011). As our goal was to characterise the diamond-forming medium, we focussed our SIMS analyses on the innermost fragments, but in a few cases where this was not possible an outer part of the diamond was used. The SIMS results gave nitrogen concentrations between 2 and 1681 at.ppm, within this range only three diamonds exceeded the upper nitrogen value (1217 at.ppm) from the FTIR analyses. Considering the focus on the inner diamond zones for SIMS analyses and the different spatial resolution of the two methods – SIMS samples a volume of $15 \times 15 \times 1 = 225 \mu\text{m}^3$ and FTIR on cleavage fragments typically samples

100x100x200=2x10⁶ μm³ – the agreement of the two concentration ranges is satisfactory. Karowe eclogitic diamonds tend to have higher nitrogen contents (median value of 513 at.ppm; Fig. 4.2c) than peridotitic diamonds (median value of 129 at.ppm; Fig. 4.2d). From worldwide sources, the median nitrogen abundances of 494 at.ppm for eclogitic diamonds and 82 at.ppm for peridotitic diamonds (Stachel 2014), are close to those at Karowe. The two sublithospheric diamonds at Karowe with majoritic garnet inclusions (Motsamai et al. 2018) have nitrogen concentrations of 30 and 250 at.ppm.

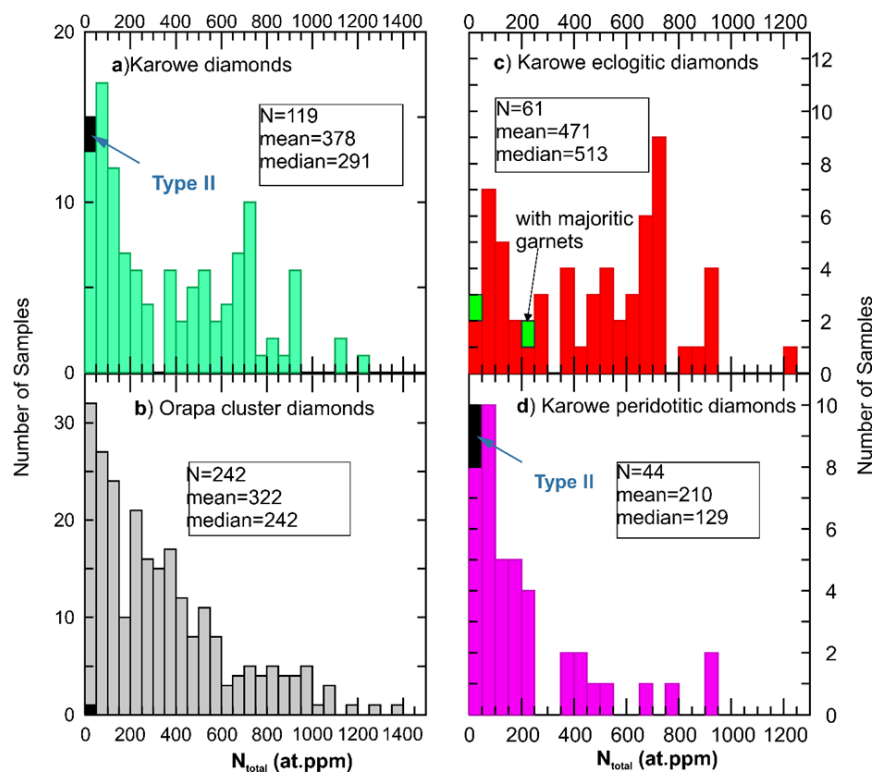


Fig. 4.2 Histograms comparing the nitrogen content in diamonds from Karowe (a) and the Orapa kimberlite cluster (b); Karowe eclogitic (c) and peridotitic (d) diamonds are also shown separately. Data for diamonds from the Orapa kimberlite cluster are from Deines et al. (1993), Deines and Harris (2004) and Deines et al. (2009)

Nitrogen aggregation in Karowe diamonds ranges between 0 and 100 %B, with a mean of 43 %B and a median of 39 %B. Similar average nitrogen aggregation states were reported for

diamonds from the three principal mines of the Orapa kimberlite cluster: Orapa 40 %B; Letlhakane 43 %B; Damtshaa 32 %B (Deines et al. 2009). From Fig. 4.3 the nitrogen aggregation state of Karowe diamonds can be divided into two groups: low to intermediate aggregation states (<70 %B) and high aggregation states (>80 %B). The two sublithospheric diamonds with 86 and 95 %B, fall into the highly aggregated group, similar to nitrogen-bearing diamonds of sublithospheric origin from other localities (Kaminsky and Khachatryan 2001).

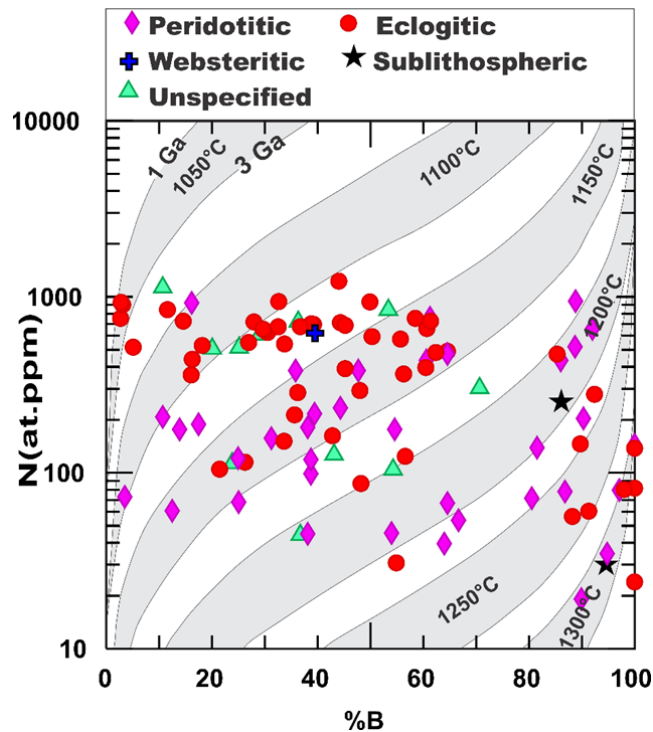


Fig. 4.3. Total nitrogen concentration (at.ppm) versus relative percentage of nitrogen in B centers for Karowe inclusion-bearing diamond fragments. Isotherms shown are calculated for mantle residence times of 1 and 3 Ga after Leahy and Taylor (1997)

4.3.3 Platelet defects and hydrogen-related absorption peaks

Platelets are planar defects found in Type Ia diamonds that form parallel to {100} lattice planes (Kiflawi et al. 1998, Sobolev et al. 1969). The creation of vacancies during advanced nitrogen aggregation gives rise to their formation (Woods 1986) and they generally produce a sharp

absorption peak approximately between 1358 and 1372 cm^{-1} . The exact position of the platelet peak (B') is dependent on the size of the platelets (nanometer to micrometer), where large platelets are observed at lower wave numbers (Clackson et al. 1990; Mendelssohn and Milledge 1995; Speich et al. 2017).

Excluding all pure Type IaA samples and all samples with less than 50 at.ppm nitrogen, which leads to poor precision in the determination of both the concentration of nitrogen in B-centers (N_B) and the platelet peak area, a total of 61 samples have platelet peak positions between 1361 and 1372 $\pm 2 \text{ cm}^{-1}$ with integrated peak areas ranging from 3.1 to 517 cm^{-2} . Both platelet peak positions and integrated areas were measured using the OMNIC spectra software. The platelet diameters in Fig. 4.4 were calculated using an equation from Speich et al. (2017) and vary between 19 and 200 nm. Larger platelet diameters ($>120 \text{ nm}$) occur at a lower average peak position of 1361 $\pm 2 \text{ cm}^{-1}$, which agrees well with previous findings (Clackson et al. 1990; Mendelssohn and Milledge 1995).

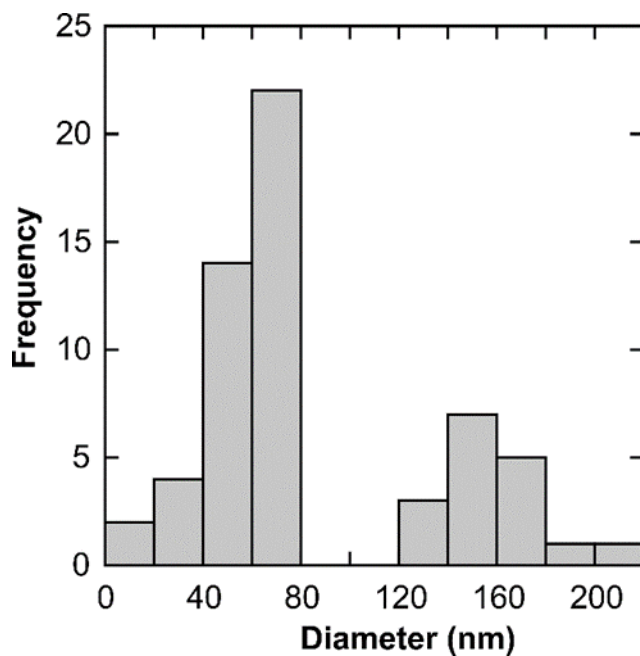


Fig. 4.4 Histogram showing calculated platelet diameters (Speich et al. 2017) for Karowe diamonds

Table 4.1 Integrated platelet peak areas, concentrations of nitrogen in B-centers and model temperatures for selected samples processed with the Speich et al. (2018) program and derived using a manual approach (*)

Sample ID	Integrated peak area (cm ⁻²)		Concentration of nitrogen in B-center (ppm)		Model temperatures derived from nitrogen aggregation at 1 Ga (°C)	Calculated platelet temperatures for 1 Ga (°C)	
KW39	76.9	*108	155	*146	1130	1241	*1197
KW55	70.3	*82.8	189	*180	1129	1254	*1254
KW80	102	*166	222	*270	1130	1245	*1228
KW81	116	*163	267	*270	1136	1248	*1228
KW82	80.8	*117	180	*175	1157	1246	*1217
KW83	209	*278	480	*462	1139	1248	*1228
KW85	192	*273	422	*439	1145	1249	*1225
KW89	122	*171	280	*246	1136	1248	*1211

Based on the genetic association between the formation of platelets and B-centers, Woods (1986) derived a linear relationship between the integrated platelet peak area [I(B^{''})] and the absorption due to nitrogen B-centers (μ_B) for “regular” diamonds. This linear trend breaks down for “irregular” diamonds because they experienced catastrophic platelet degradation related to deformation (Woods 1986) or short-lived heating (Evans et al. 1995). More recently, Speich et al. (2018) recognised a third category, “subregular” diamonds, where low mantle residence temperatures (≤ 1120 °C) result in development of small platelets (see Fig. 9 of Speich et al. 2018). A few of the Karowe samples (n=8) with very good to excellent spectra were re-processed using the QUIDDIT program of Speich et al. (2018), which automates the processing and deconvolution of infrared spectra of diamonds. For the platelet peak area, the program gives lower values than our “manual” assessment using the OMNIC software (Table 4.1; an average relative percentage

difference of 34 %). The peak positions have an offset of up to 1.6 cm^{-1} , which is within error, considering that our spectra were recorded with measurement spacing of 1.9 cm^{-1} .

Using our results, most of the Karowe diamonds studied here are considered “regular” and fall more closely to the original trend of Woods (1986) than to the modelled regression lines of Speich et al. (2018). The exceptions are four eclogitic diamonds, which clearly show “irregular” behaviour, one containing majoritic garnet as inclusion (i.e., being sublithospheric) and one being plastically deformed (Fig. 4.5a). Due to the low resolution of our spectral data (measurement spacing of 1.9 cm^{-1}), platelet peak positions are considered accurate within $\pm 2 \text{ cm}^{-1}$ (Fig. 4.5b), precluding the distinction between regular/irregular and subregular behaviour (Speich et al. 2018) for a large proportion of our samples.

A high hydrogen-related absorption peak at 3107 cm^{-1} is observed in many diamonds ($n=58$). This peak has originally been linked to a C-H stretching vibrational mode (Fritsch et al. 2007, Woods and Collins 1983) but is now attributed to VN_3H defects (Goss et al. 2014). The integrated 3107 cm^{-1} peak area ranges from 0.98 to 30.5 cm^{-2} , but the distribution is skewed towards lower values (median= 3.8 cm^{-2}). The 3107 cm^{-1} absorption peak is mostly associated with Type IaAB diamonds (79 %), but is also observed in some Type IaA and IaB diamonds and in one case in a Type II diamond.

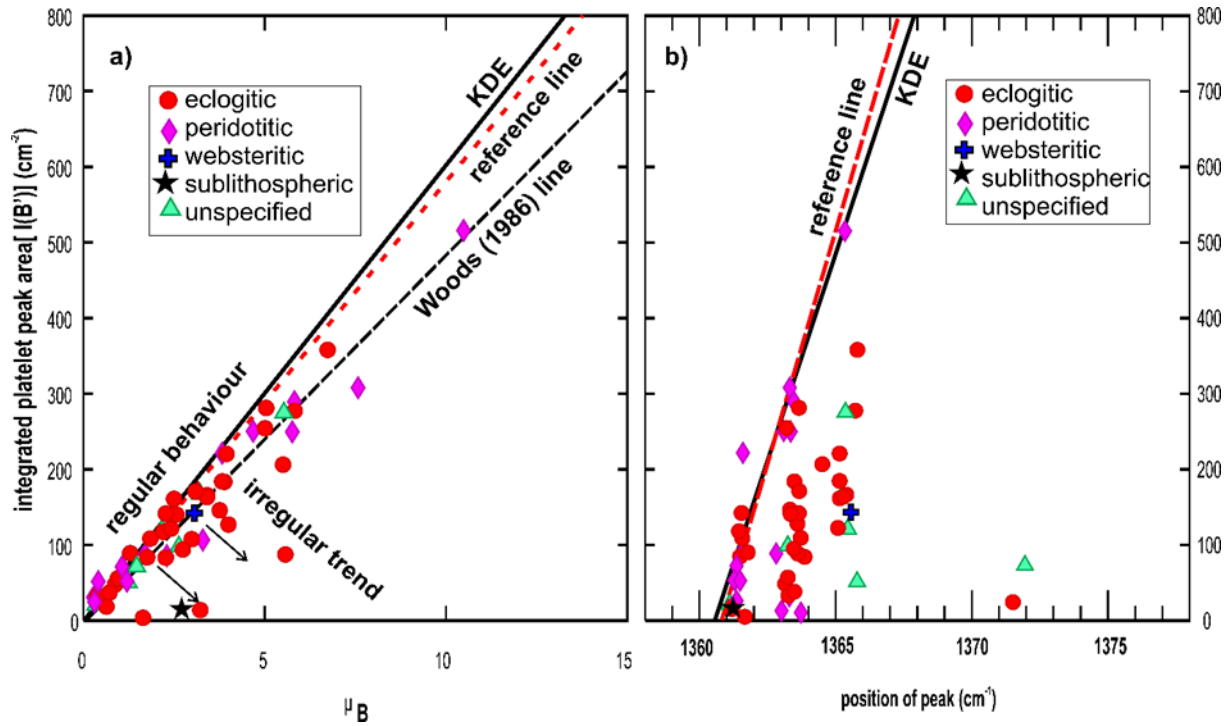


Fig. 4.5 a) The relationship between integrated platelet peak area $[I(B')]$ and absorption due to nitrogen B-centers (μ_B). The kernel density estimation (KDE) and the reference line defining regular behaviour are from Speich et al. (2018). Also shown is the regularity trend of Woods (1986) Samples plotting to the right of these lines are considered “irregular” and experienced platelet degradation. b) The relationship between platelet peak area and the position of platelet peak

4.3.4 Carbon isotope composition

The carbon isotope compositions ($\delta^{13}C$) measured for 119 Karowe diamonds range from -34.5 ‰ to -2.0 ‰, with a main mode between -6.0 and -3.5 ‰ and a small mode between -9.0 to -7.0 ‰ (Fig. 4.6a). This overall distribution and range is in good agreement with carbon isotope compositions of diamonds from other localities in the Orapa kimberlite cluster (Fig. 4.6b). Excluding two diamonds with unusually low $\delta^{13}C$ values (KW 32=-34.5 ‰ and KW 74=-14.9 ‰), peridotitic diamonds fall between -8.6 to 2.0 ‰. In a cumulative probability plot (Isoplot, Ludwig 2003), the main mode for peridotitic diamonds can be determined as -3.8 ‰ (Fig. 4.7). Eclogitic diamonds range from -21.6 to -2.5 ‰, with six samples falling below -10 ‰, and show a sharp

peak in class -5.0 to -4.5 ‰. In a cumulative probability plot, the eclogitic mode is at -4.8 ‰, which is offset by -1 ‰ relative to the peridotitic sample suite (Fig. 4.7).

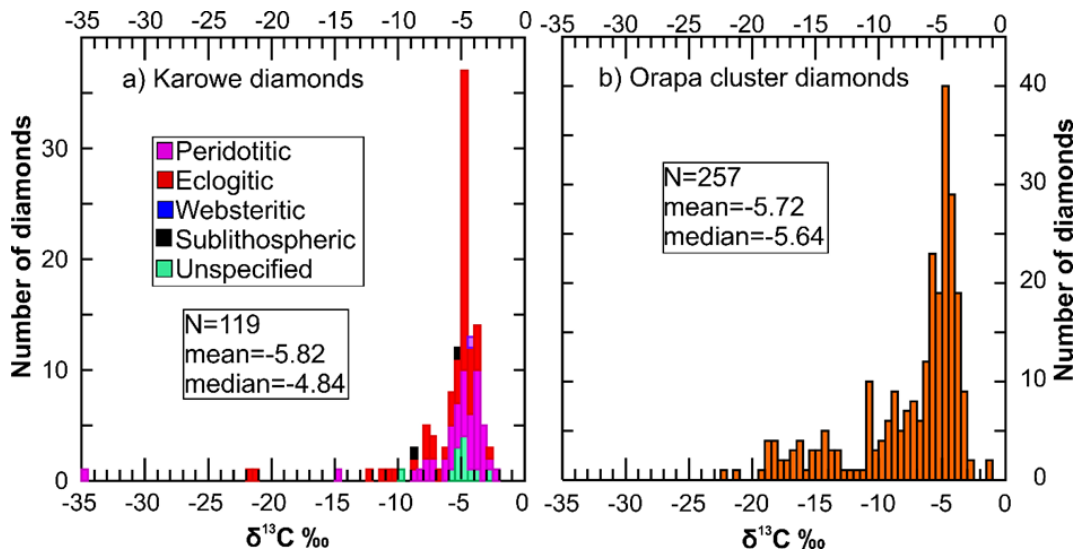


Fig. 4.6 Histograms comparing the carbon isotope compositions of diamonds from Karowe and other Orapa cluster kimberlites (a, b). Data for diamonds from the Orapa kimberlite cluster are from Deines et al. (1993), Deines and Harris (2004) and Deines et al. (2009)

A plot of nitrogen content vs $\delta^{13}\text{C}$ (Fig. 4.8) shows the relationship of decreasing maximum nitrogen content with decreasing $\delta^{13}\text{C}$ values previously observed for diamonds worldwide (Stachel and Harris 1997) and formalised as the limit sector curve by Cartigny et al. (2001). Ten of the 119 diamonds analysed show significant internal variations of carbon isotopic composition and nitrogen content, with representative examples shown in Fig. 4.9. The maximum internal variation in $\delta^{13}\text{C}$ measured was 10 ‰ (from -14.8 in the central region to -4.8 ‰ in the rim zone; diamond KW24 in Fig. 4.9).

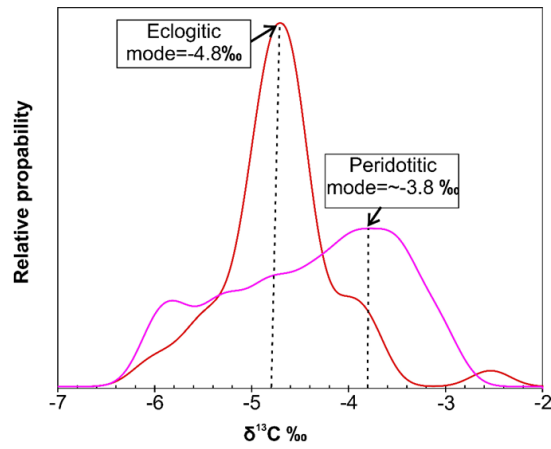


Fig. 4.7 Cumulative probability plot (Ludwig 2003) showing the main modes for peridotitic and eclogitic diamonds from Karowe

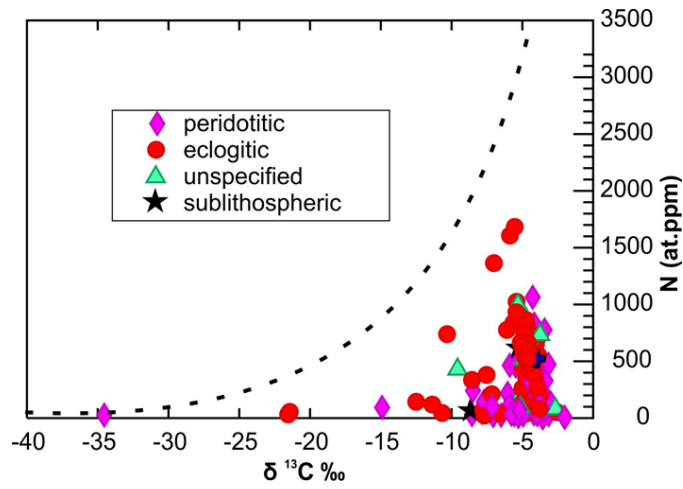


Fig. 4.8 Co-variations between nitrogen content and carbon isotopic composition (both measured via SIMS) of Karowe diamonds. The dotted line represents the limit sector curve of Cartigny et al. (2001)

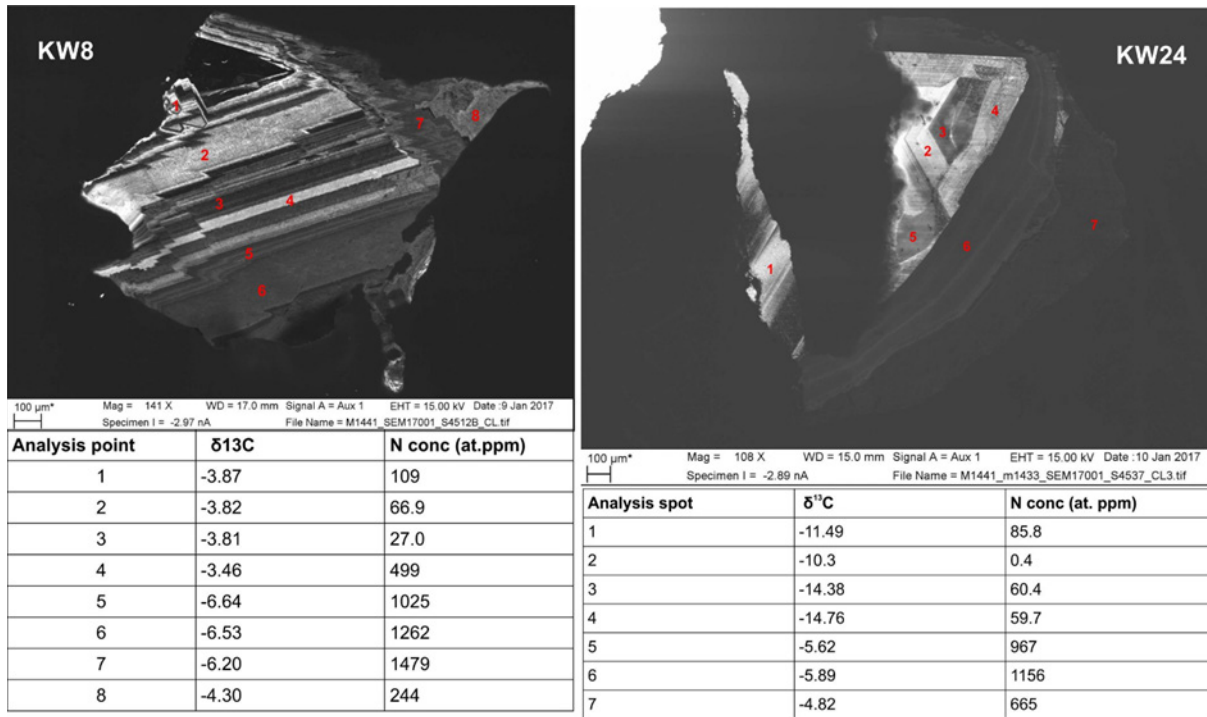


Fig. 4.9 Examples of the internal growth structures of Karowe diamonds as seen in CL images, together with locations of SIMS analyses. The corresponding data are given in the tables below the figures. Left: Diamond KW8 shows nearly planar octahedral growth that appears to be resorbed on the right before being overgrown by the poorly luminescent layers containing spots 7 (likely equivalent to the layer with spot 6) and 8. Spot 5 marks the arrival of a new pulse of fluid with lower $\delta^{13}\text{C}$ and higher N content. Right: Diamond KW24 shows a jump from strongly ^{13}C depleted, low-nitrogen growth to mantle-like $\delta^{13}\text{C}$ and high nitrogen. Whilst in the CL image the main discontinuity seems to occur between the growth phases containing points 5 and 6, compositionally point 5 actually is already part of the mantle-like growth phase

4.4 Discussion

4.4.1 Diamond characteristics in comparison with those from the Orapa cluster

Apart from the large scale classification of the shape and colour of diamonds from the Orapa mine (Harris et al.1986), the only other diamonds which have been examined for these two physical characteristics in the Orapa kimberlite cluster are those which formed part of inclusion studies (Deines et al. 1993; Deines and Harris 2004). Assuming that the studied diamonds from Karowe are representative of the smaller size range (-11+5 Diamond Trading Company sieve classes) of general diamond production, their morphology and colour can be compared to the Orapa data for similar sized diamonds (-7+5). For the studied size range, combined octahedra, transitional-habit, and rounded dodecahedra diamonds at Karowe are approximately 60 %, which is much more abundant than at Orapa (~20 %), the macles are the same (~20 %), and the aggregated diamonds are more common at Orapa (60 %), (Harris et al.1986).

It is not meaningful to compare colour in the same way as done above for shape, as the colour assessment is based on diamonds recovered from different levels in the two kimberlites. Normally this would not be a problem, but at Orapa in 1983 (Harris et al. 1986) mining operations were in the crater-lake facies kimberlite where a significant proportion of the production, irrespective of the original colour of the diamond, was transparent green coated due to α -particle irradiation related to the mildly radioactive groundwater in this kimberlite zone. Accordingly, the colours of the studied Karowe diamonds should be considered more representative of primary (pre-eruptive) colourations, being dominantly colourless, with minor brown and transparent green coated stones. Of the seventeen plastically deformed diamonds identified, four diamonds were

brown, which is specifically consistent with the origin of that colour, eleven were colourless and two were transparent-green coated.

4.4.2 Diamond-forming fluids and carbon sources

The carbon isotope compositions of the 119 analysed Karowe diamonds range from -34.5 to -2.0 ‰ with a mean $\delta^{13}\text{C}$ value of -5.8 ‰ and a median at -4.8 ‰ (Fig. 4.6a). The majority of the diamonds (both eclogitic and peridotitic) have $\delta^{13}\text{C}$ values in the range -6.0 to -3.5 ‰, indicating that they are derived from sources with mantle-like (-5.0 ± 3 ‰; Cartigny 2005) isotopic characteristics. Despite this strong predominance of carbon with mantle-like isotope composition, the mode for diamonds with peridotitic inclusions is offset from the mode for diamonds with eclogitic inclusions by 1 ‰ (peridotitic mode: -3.8 ‰; eclogitic mode: -4.8 ‰). Such a shift may indicate the tapping of separate carbon reservoirs. For example, fluids derived from the convecting mantle and from altered oceanic crust in subducting slabs, may both have mantle-like compositions (Shilobreeva et al. 2011) which could readily differ by 1 ‰. Alternatively, subtle variations in the carbon speciation in diamond-forming fluids could be responsible for this 1 ‰ shift in $\delta^{13}\text{C}$ mode. As modelled by Stachel et al. (2017), a decrease in X_{CO_2} ($\text{CO}_2/[\text{CO}_2+\text{CH}_4]$) in the diamond-forming fluid by 0.2 would produce a 1 ‰ increase in the $\delta^{13}\text{C}$ values of precipitated diamond. Another possibility, during isochemical precipitation from ascending or cooling fluids, a switch in diamond precipitating mode from the reaction $\text{CO}_2 + \text{CH}_4 = 2\text{H}_2\text{O} + 2\text{C}$ for a water maximum fluid (with an X_{CO_2} of ~ 0.2) for eclogitic diamonds to $2\text{C}_2\text{H}_6 = 3\text{CH}_4 + \text{C}$ for a more reduced fluids (Luth and Stachel 2014) for peridotitic diamonds could also explain this approximately +1 ‰ shift in mode.

A small proportion of diamonds show strong ^{13}C depletion outside the range of typical mantle carbon, six eclogitic ($\delta^{13}\text{C}$ -21.4‰ to -10.3‰) and two peridotitic ($\delta^{13}\text{C}$ -34.5‰ and -14.9‰). High temperature isotopic fractionation processes occurring during CO_2 escape from a diamond-forming mantle-derived melt/fluid (Cartigny et al 2001) have been suggested as the cause of such strong ^{13}C depletions. Co-variations of $\delta^{13}\text{C}$ and nitrogen content (Fig. 4.8) obeying the limit sector curve of Cartigny et al. (2001) are consistent with this interpretation, as in the model nitrogen is lost together with CO_2 during separation of a fluid phase from a carbonate-bearing melt before diamond precipitation. However, starting from the mantle value ($\delta^{13}\text{C}$ of -5‰; Cartigny 2005), realistic degrees of Rayleigh fractionation during CO_2 escape are unlikely to cause $\delta^{13}\text{C}$ values below about -11‰ (Smart et al. 2011). The majority of the strongly ^{13}C -depleted Karowe diamonds, therefore, must have originated from a fluid/melt carrying carbon of non-mantle origin. Indeed, the origin of strongly ^{13}C -depleted diamonds has long been linked to the subduction of former organic matter (Kirkley et al. 1991; Sobolev and Sobolev 1980). Overall, Karowe eclogitic diamonds cover a $\delta^{13}\text{C}$ range from -21.6 to -2.5‰ and thus fall within the typical range of eclogitic diamonds worldwide (-38.5 to 2.7‰, Cartigny 2005). From the large variability in both the eclogitic mineral inclusion chemistry (Motsamai et al. 2018) and the carbon isotope composition of the host diamonds, we propose that both subduction- and mantle-derived carbon was involved in the formation of Karowe eclogitic diamonds. Ickert et al. (2013) suggested that the carbon content in eclogitic diamond substrates from the Damtshaa mine (<30 km from Karowe) is generally so low that its isotopic compositions was completely overwhelmed during infiltration of mantle-derived diamond-forming fluids. Only for highly altered, shallow portions of former oceanic crust is the content of organic matter-derived carbon sufficiently high enough to cause

precipitation of diamonds with low to very low $\delta^{13}\text{C}$ values during influx of external fluids (Ickert et al. 2013).

Two peridotitic samples have very low $\delta^{13}\text{C}$ values (KW32=-34.5 ‰ and KW74=-14.9 ‰) with one being clearly outside the worldwide range of peridotitic diamonds (-26.4 to +0.2 ‰; Cartigny 2005). KW32 is the most ^{13}C -depleted peridotitic diamond observed so far. This diamond hosts a disequilibrium assemblage of olivine + coesite and has a low nitrogen content (<67 at.ppm). The presence of olivine and SiO_2 in the same diamond may relate to intense progressive carbonation reactions involving free CO_2 fluids (Wyllie and Huang 1976), as previously described, e.g., by Hunt et al. (2012) for diamonds from Renard (Superior Craton). Extreme local CO_2 fluxing of the substrate for diamond KW32 likely involved a subduction-related fluid source.

When comparing the Karowe diamonds with other diamonds from the Orapa kimberlite cluster (Fig. 4.6b), they have an overall similar $\delta^{13}\text{C}$ distribution. This suggests that the formation of Karowe eclogitic and peridotitic diamonds may have occurred during the same growth episodes and from carbon with similar mantle-derived and subduction-related sources to those observed elsewhere in the Orapa cluster.

4.4.3 Nitrogen thermometry

The interrelationship of the content and aggregation state of nitrogen in diamond with its mantle residence time and time-averaged residence temperature can be employed as a thermochromter (Evans and Harris 1989; Taylor et al. 1990). The stronger dependence of nitrogen aggregation on residence temperature (see Fig. 4.3) compared to residence time makes nitrogen-in-diamond a robust geothermometer and a poor geochronometer.

Calculated for 3 Ga mantle residence, nitrogen-in-diamond based thermometry (Taylor et al. 1990; Leahy and Taylor 1997) yields residence temperatures between 1033 and 1283 °C for Karowe Type Ia diamonds. A few samples (n=19), mostly pure Type IaA (0 %B) and pure Type IaB (100 %B) diamonds were excluded from the calculations. The two main parageneses (eclogitic and peridotitic) show overlapping distributions in their mantle residence temperatures (Fig. 4.3). Karowe eclogitic diamonds, based on an average mantle residence of 1 Ga derived for eclogitic diamonds from southern African kimberlites (Richardson et al. 1990), yield a mean of 1160 °C and a median of 1155 °C (Fig. 4.10a), values that are within error (about ± 50 °C of Taylor et al. 1990) of eclogitic diamonds worldwide (mean=1170 °C; median=1162 °C; Stachel and Harris 2008). The Fe-Mg exchange equilibration temperatures (Krogh 1988) calculated for five non-touching pairs of eclogitic garnet and clinopyroxene are significantly hotter (1260 to 1480 °C). This implies that there is disequilibrium between eclogitic garnet and clinopyroxene inclusions, which is widespread and systematically biased to Mg-enrichment for garnets and/or Fe-enrichment for clinopyroxene (Ai 1994). Alternatively, formation of Karowe eclogitic diamonds occurred at temperatures that were 100 to 300 °C higher than time averaged residence temperatures.

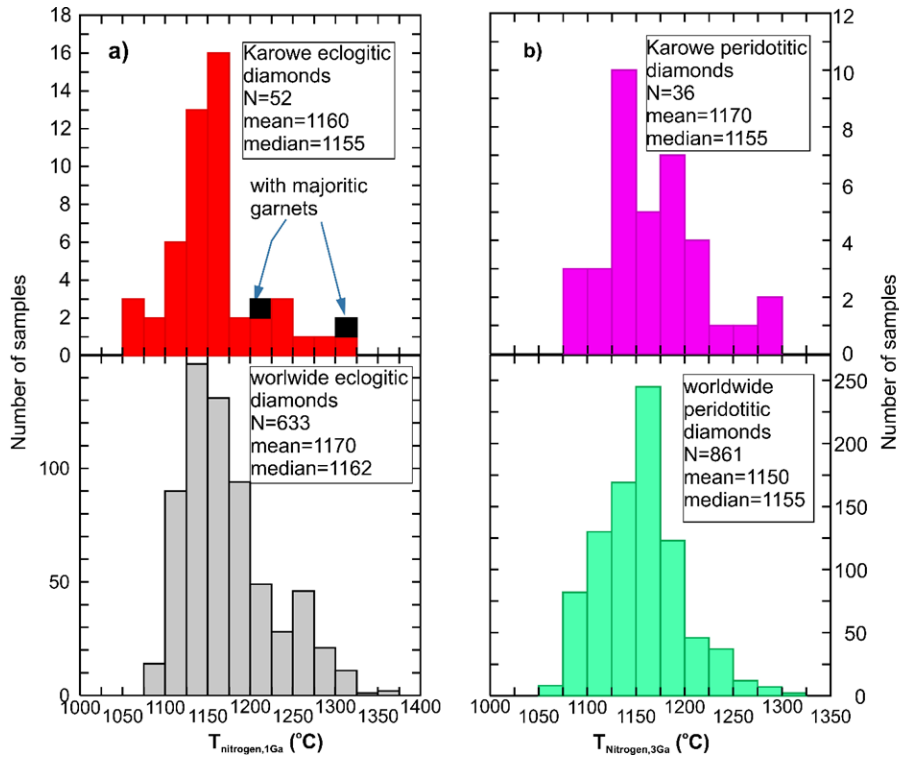


Fig. 4.10 Histograms showing calculated mantle residence temperatures for diamonds from Karowe (top) and worldwide (bottom) assuming mantle residence for a period of 1 Ga for eclogitic diamonds (a) and 3 Ga for peridotitic diamonds (b). Diamonds containing majoritic garnets are shown in black

Based on 3 Ga mantle residence (e.g., Gurney et al. 2010) for peridotitic diamonds temperatures (mean=1170 °C and 1155 °C; Fig. 4.10b) are almost identical to those for eclogitic diamonds with 1 Ga mantle residence temperatures (mean=1160 °C and median=1155 °C; Fig. 4.10a). Mineral exchange thermometry estimates (Motsamai et al. 2018) from one touching (1033 °C) and three non-touching (903-1245 °C; mean 1028 °C) garnet-olivine pairs indicate derivation from lower temperatures. However, the 130 °C difference between mineral exchange and nitrogen-in-diamond based temperature estimates is within error of the two methods, with garnet-olivine thermometry being considered accurate but imprecise (about ± 100 °C; Brey and Köhler 1990). If real, the systematically lower temperature of diamond formation derived from garnet-olivine pairs may relate to thermal pulses occurring during subsequent mantle residence.

4.4.4 Platelet behaviour and platelet degradation thermochronometry

Diamonds can be classified as regular, subregular and irregular based on their platelet behaviour as summarised by Speich et al. (2018). In irregular diamonds platelet degradation is associated with the breakdown of the linear relationship between integrated peak area $[I(B')]$ and the absorption due to nitrogen in B centers (μ_B). It may occur due to transient exposure to a thermal pulse (Evans et al. 1995) or during plastic deformation of diamonds (Woods 1986). Our results show a better fit with the linear trend established by Woods (1986) compared to the Speich et al. (2018) regression lines (Fig. 4.5a). This might be attributed to the procedures employed for processing spectra and baselining of the platelet peak (i.e., manual vs automatic). Samples falling on the regular trend in $[I(B')]$ versus μ_B space (Fig. 4.5a), but plotting off the regular trend in $[I(B')]$ versus platelet peak position space (Fig. 4.5b) are defined as “subregular” by Speich et al. (2018). The spectral resolution of our measurements is insufficient for reliable application of this approach and following Speich et al. (2018: their Fig. 9 and Fig. 14) we, therefore, use nitrogen-in-diamonds based temperatures below 1120 °C to define subregular samples. Of the Karowe samples, only one sample (KW119) yields nitrogen-in-diamond temperatures below 1120 °C and consequently classifies as subregular. As platelet thermochronometry must not be applied to subregular samples (Speich et al. 2018), this sample was excluded from the platelet temperature calculations. For eight spectra (Table 4.1) of very good quality we used the QUIDDIT program of Speich et al. (2018), which automatically fits a background and retrieves the platelet peak intensity. This program yields systematically smaller peak areas leading to platelet degradation temperatures that are on average 24 °C higher than our calculated values. However, both approaches (manual measurements using the OMNIC software and automated measurements with QUIDDIT) yield temperatures that are hotter compared to nitrogen-in-diamond based temperatures, calculated at 1

Ga mantle residence (Table 4.1 and Fig. 4.11); the average temperature difference between platelet and nitrogen based estimates is slightly higher (109 °C) for automated processing (QUIDDIT) compared to manual determinations (86 °C). Most likely this difference in platelet temperatures relates to how the local background below the platelet peak is fitted.

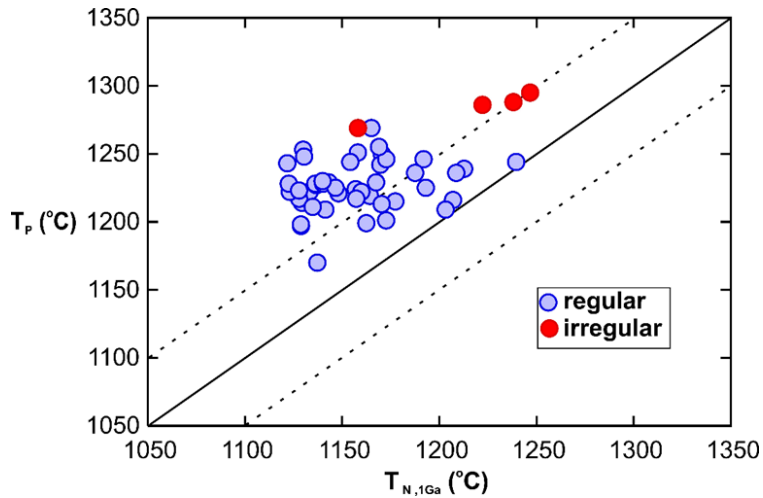


Fig. 4.11 Comparison of platelet degradation temperature (T_p) and nitrogen aggregation temperature (T_N) assuming 1 Ga mantle residence. Solid line indicates a 1:1 correlation and dashed lines indicate $\pm 50^\circ\text{C}$ error

In summary, the platelet peak areas derived with our approach result in platelet degradation temperatures that show better agreement with nitrogen-in-diamond temperatures, compared to automated baseline fitting. On a qualitative level, relative to the regular trend derived by Woods (1986), most of Karowe samples display near-regular behaviour (Fig. 4.5a) and hence have not been affected by intense heating or deformation events.

4.5 Conclusion

The wide range of diamond morphologies in Karowe diamonds is matched by a wide variation in aggregation states (0 to 100 %B) and total nitrogen contents (≤ 15 to 1217 at.ppm). Karowe eclogitic diamonds have higher nitrogen contents (median=513 at.ppm) than peridotitic diamonds (median=129 at.ppm), similar to eclogitic and peridotitic diamonds worldwide. Based on nitrogen

aggregation, two populations can be recognised: The dominant group, with low to intermediate nitrogen aggregation states, indicates time-averaged mantle residence temperatures between 1050 and 1200 °C for a period of 3 Ga. A smaller population of diamonds with $>80\%$ B reflects residence temperatures between 1120-1280 °C. A minor group of diamonds shows evidence of platelet degradation, suggesting exposure to high temperatures and/or shear stresses.

The carbon isotope compositions of Karowe diamonds range from -34.5 to -2.0 ‰ with a median value at -4.8 ‰. Both eclogitic and peridotitic diamonds have mantle-like $\delta^{13}\text{C}$ values (mainly between -6.0 to -3.5 ‰) but the mode of peridotitic diamonds (-3.8 ‰) is offset by about 1 ‰ relative to eclogitic diamonds (mode at -4.8 ‰). This shift in mode may relate to precipitation of peridotitic diamonds from more reducing fluids (i.e., with somewhat lower CO_2/CH_4 ratios). Six diamonds with eclogitic inclusions and two with peridotitic inclusions have carbon isotope compositions below -10.0 ‰. These moderately to strongly ^{13}C -depleted compositions likely represent variable mixtures of subducted former organic matter and mantle carbon. In combination, our results indicate that Karowe diamonds grew episodically from fluids of variable compositions (mantle-like and subduction related).

Chapter Five

5.0 Summary of the main findings

Overall, the five questions investigated by this thesis project were fully addressed and the results are generally comparable to those of previous studies conducted on other localities in the Orapa kimberlite cluster (such as Orapa, Damtshaa and Letlhakane) and globally. In terms of xenoliths, the Karowe kimberlites preferentially sampled shallow the spinel peridotites of the uppermost mantle. The data obtained from the diamonds and their mineral inclusions suggest the involvement of subducted carbon in the formation of diamonds at Karowe.

5.1 The lithospheric mantle beneath Karowe mine

Karowe mantle xenoliths are mostly derived from shallow mantle, which encountered variable degrees of partial melting and metasomatic processes. Xenoliths are dominated by coarse to granolublastic textured spinel lherzolites (14 out of 24), with exsolution lamellae of clinopyroxenes and orthopyroxenes and low equilibration temperatures (630 to 800 °C). The Mg# in olivine grains range between 91.2 and 92.5 (median: 92.1) consistent with extensive melt depletion (27 to 36 % melt extraction). A small proportion of the xenoliths sampled from the garnet facies is represented by garnet-spinel lherzolites (n=4), one garnet lherzolite as well as garnet clinopyroxenites (n=3) and a single eclogite. The trace element compositions of the garnets and clinopyroxenes indicate cryptic melt metasomatism and in some instances, modal metasomatism associated with the introduction of phlogopite. These styles of metasomatism have also been reported in Orapa and Letlhakane xenoliths and relate to either the large-scale Bushveld intrusive event, or to melt/fluids associated with the ~1.8 Ga formation of the Magondi Belt. Clinopyroxene-based geothermobarometry on xenocrysts and the single garnet lherzolite xenolith indicates a 39 to 40 mW/m² model paleogeotherm of Hasterok and Chapman (2011) beneath Karowe with a 210

km thick lithosphere and a diamond window that is ~90 km wide. This large diamond window is consistent with the presence of several major economic diamond deposits in this region of the Zimbabwe craton.

5.2 Paragenetic origins of Karowe diamonds

The eclogitic mantle is the predominant source of diamonds at Karowe (53 %), although relatively rare in the mantle xenolith samples examined in this study. Peridotitic diamond substrates account for 44 %, followed by two diamonds of sublithospheric origin (2 %) and a diamond of websteritic association (1 %). The dominant eclogitic diamond substrates are compositionally variable, ranging from typical basaltic to cumulate-like protolith compositions. This variability is reflected by a wide range in the CaO contents (4-16 wt%) of garnets and the Mg# (69-92) and jadeite contents (14-48 mol%) of clinopyroxenes as well as the presence of three kyanite inclusions. Calculated bulk rock REE_N patterns indicate that both shallow and deep levels of the subducted slab(s) were sampled. The peridotitic inclusion suite comprises of highly depleted harzburgitic to dunitic diamond substrates, with almost half the garnets having CaO contents <1.8 wt %, consistent with pyroxene-free (dunitic) sources. One low-Ca garnet inclusion records a very high Cr₂O₃ content (14.7 wt%), implying that highly depleted cratonic lithosphere at the time of diamond formation extended to at least 210 km depth. A sublithospheric inclusion suite is established by three eclogitic garnets containing a majorite component, a feature so far unique within the Orapa cluster. These sublithospheric diamonds may provide the link to the occurrence of large to extremely large gem-quality diamonds that are nitrogen “free” Type IIa or Type IaB containing low contents of completely aggregated nitrogen (D’Haenens-Johansson et al. 2017). The two majoritic garnet-bearing diamonds are not Type IIa but have very low to moderate nitrogen contents and highly aggregated nitrogen (30 and 250 at.ppm with 95 and 86 %B respectively).

Their discovery shows that sublithospheric diamond sources were tapped by the Karowe kimberlite, further strengthening the recent observation by Smith et al. 2016 that large Type II diamonds generally originate from the sublithospheric mantle.

5.3 Diamond characteristics

On the basis of the observations made in this study, the Karowe diamonds have variable morphologies, with a dominance of octahedra (30 %), macles (20 %) and moderately resorbed morphologies (transitional between octahedra and rounded dodecahedra; 18 %). The remaining 32 % are made up of rounded dodecahedra, cubo-octahedra, pseudo-hemimorphic and aggregated crystals. Karowe diamonds show wide ranges in nitrogen contents from below the limit of detection (≤ 15 at.ppm up to 1217 at.ppm) with nitrogen aggregation states spanning the full range from Type IaA (0 %B) to IaB (100 %B). Eclogitic diamonds contain higher nitrogen contents (median=513 at.ppm) than peridotitic diamonds (median=129 at.ppm), similar to eclogitic and peridotitic diamonds worldwide. Based on nitrogen aggregation states, two populations were recognised: a dominant population of Type IaA to IaAB diamonds with less than 70 %B and a minor population of highly aggregated Type IaAB to IaB (80 to 100 %B) diamonds.

The $\delta^{13}\text{C}$ values of the analysed diamonds range from -34.5 to -2.0 ‰ with a median at -4.8 ‰, indicating that Karowe diamonds grew episodically from fluids of variable compositions. For eclogitic diamonds, the $\delta^{13}\text{C}$ values range between -21.5 and -2.5 ‰ with a median at -4.9 ‰. With the exception of two diamonds which display an unusual, strongly ^{13}C -depleted compositions (-34.5 and -14.9 ‰), most of peridotitic diamonds have a typical mantle-like $\delta^{13}\text{C}$ range (-8.6 to -2.0 ‰). Both eclogitic and peridotitic diamonds have $\delta^{13}\text{C}$ values predominantly in the range -6.0 to -3.5 ‰, but the mode of peridotitic diamonds (-3.8) is offset by about +1 ‰ relative to eclogitic diamonds (mode at -4.8 ‰). This shift in mode could reflect precipitation of peridotitic diamonds

from more reducing fluids (i.e., with somewhat lower CO_2/CH_4 ratios). These moderately to strongly ^{13}C -depleted compositions likely represent variable mixtures of subducted former organic matter and mantle carbon.

6.0 Future work and considerations

To fill the information gap about the different generations of diamonds at Karowe, further investigations are needed on the geochronology of mineral inclusions in diamonds, a topic which is beyond the scope of this study. There are still more inclusion studies required to better define the proportion of sublithospheric diamonds at Karowe, in view of the large diamond population.

From the clinopyroxene xenocryst-based geotherm, the results show an offset of ~ 1 to 2 mW/m^2 between shallow (40 to 41 mW/m^2) and deeper (~ 38 to 39 mW/m^2) xenocryst groups when plotted against an established 40 mW/m^2 paleogeotherm (Hasterok and Chapman 2011) derived by Stiefenhofer et al. (1997) for Letlhakane peridotite xenoliths. Therefore, more data is required to compare the xenocryst-base geotherm for Karowe with a xenolith-derived geotherm and to determine if the offset relative to Letlhakane is due to cooling or reveals a mantle section below Karowe that moved out of the diamond stability field.

References

- Ai Y (1994) A revision of the garnet-clinopyroxene Fe^{2+} -Mg exchange geothermometer. *Contributions to Mineralogy and Petrology* 115:467-473
- Armstrong JT (1995) CITZAF-a package of correction programs for the quantitative electron microbeam X-ray of thick polished materials, thin-films, and particles. *Microbeam Analysis* 4:177-200
- Aulbach S, Jacob DE, Cartigny P, Stern RA, Simonetti SS, Wörner G, Viljoen KS (2017) Eclogite xenoliths from Orapa: Ocean crust recycling, mantle metasomatism and carbon cycling at the western Zimbabwe craton margin. *Geochimica et Cosmochimica Acta* 213:574-592
- Aulbach S, Viljoen KS (2015) Eclogite xenoliths from the Lace kimberlite, Kaapvaal Craton: From convecting mantle source to palaeo-ocean floor and back. *Earth Planetary Science Letters* 431:274-286
- Aulbach S, Jacob DE (2016) Major-and trace-elements in cratonic eclogites and pyroxenites reveal heterogeneous sources and metamorphic processing of low-pressure protholiths. *Lithos* 262:586-605
- Barnes SJ, Roeder PL (2001) The range of spinel compositions in terrestrial mafic and ultramafic rocks. *Journal of Petrology* 42 (12):2279-2302
- Beard BL, Fraracci KN, Clayton RA, Mayeda TK, Snyder GA, Sobolev NV, Taylor LA (1996) Petrography and geochemistry of eclogites from the Mir kimberlite, Yakutia, Russia. *Contrib Mineral and Petrol* 125:293-310

- Bell AS, Burger PV, Le L, Shearer CK, Papike JJ, Sutton SR, Newville M, Jones J (2014) XANES measurements of Cr valence in olivine and their applications to planetary basalts. *Am Mineral* 99(7):1404-1412
- Bernstein S, Hanghøj K, Kelemen P, Brooks CK (2006) Ultra-depleted, shallow cratonic mantle beneath West Greenland: dunitic xenoliths from Ubekendt Ejland. *Contributions to Mineralogy and Petrology* 152:335-347
- Bernstein S, Kelemen PB, Hanghøj K (2007) Consistent olivine Mg# in cratonic mantle reflects Archean mantle melting to the exhaustion of orthopyroxene. *Geology* 35(5):459-462
- Beyer C, Frost DJ (2017) The depth of sub-lithospheric diamond formation and the redistribution of carbon in the deep mantle. *Earth Planet Sci Lett* 461:30-39
- Borst AM (2012) The formation and modification of the sub-cratonic lithospheric mantle beneath Botswana. A petrological, geochemical and isotopic study of peridotite xenoliths from the Letlhakane Kimberlite mine. Master Thesis, VU University Amsterdam, Netherlands
- Boyd FR, Dawson JB, Smith JV (1984) Granny Smith diopside megacrysts from the kimberlites of the Kimberley area and Jagersfontein, South Africa. *Geochim Cosmochim Acta* 48:381-384
- Boyd FR, Gurney JJ (1986) Diamonds and the African lithosphere. *Science* 232:472-477
- Boyd FR, Pokhilenko NP, Pearson DG, Mertzman SA, Sobolev NV, Finger LW (1997) Composition of the Siberian cratonic mantle: evidence from Udachnaya peridotite xenoliths. *Contributions to Mineralogy and Petrology* 128:228-246

- Boyd FR, Pearson DG, Mertzman SA (1999) Spinel-facies peridotites from the Kaapvaal root. In Proceedings of the 7th International Kimberlite Conference, Red Roof Design, Cape Town, South Africa, pp 40-48
- Boyd SR, Kiflawi I, Woods GS (1994) The relationship between infrared absorption and the A defect concentration in diamond. *Philosophical Magazine B* 69:1149-1153
- Boyd SR, Kiflawi I, Woods GS (1995) Infrared absorption by the B nitrogen aggregate in diamond. *Philosophical Magazine B* 72:351-361
- Breeding CM, Shigley JE (2009) The “type” classification system of diamonds and its importance in gemology. *Gems and Gemology* 2 (45):96-111
- Brey GP, Köhler T (1990) Geothermobarometry in four-phase lherzolites II. New thermobarometers, and practical assessment of existing thermobarometers. *Journal of Petrology* 31(6):1353-1378
- Brey GP, Bulatov V, Gurnis A, Harris JW, Stachel T (2004) Ferropericlasite—a lower mantle phase in the upper mantle. *Lithos* 77:655-663
- Brook MC (2012) Botswana's Diamonds: Prospecting to Jewellery. Gaborone, Botswana, p 36
- Bruno M, Massaro FR, Prencipe M, Demichelis R, De La Pierre M, Nestola F. (2014). Ab initio calculations of the main crystal surfaces of forsterite (Mg_2SiO_4): a preliminary study to understand the nature of geochemical processes at the olivine interface. *Journal of Physical Chemistry C* 118: 2498-2506.
- Bulanova GP, Griffin WL, Ryan CG, Shestakova OY, Barnes SJ (1996) Trace elements in sulfide inclusions from Yakutia diamonds. *Contrib Mineral Petrol* 124:111-125

- Bulanova GP, Pearson DG, Hauri EH, Griffin BJ (2002) Carbon and nitrogen isotope systematics within a sector-growth diamond from the Mir kimberlite, Yakutia. *Chemical Geology* 188 (2002):105-123
- Canil D (1990) Experimental study bearing on the absence of carbonate in mantle-derived xenoliths, *Geology* 18:1011-1013
- Canil D, O'Neill HSC (1996) Distribution of ferric iron in some upper-mantle assemblages. *J Petrol* 37 (3):609-635
- Carlson RW, Pearson DG, Boyd FR, Shirey SB, Irvine G, Menzies AH, Gurney JJ (1999) Re–Os systematics of lithospheric peridotites: implications for lithosphere formation and preservation. In *Proceedings 7th International Kimberlite Conference, Red Roof Design, Cape Town*, pp 99-108
- Cartigny P, Harris JW, Javoy M (2001) Diamond genesis, mantle fractionations and mantle nitrogen content: a study of $\delta^{13}\text{C-N}$ concentrations in diamonds. *Earth and Planet Science Letters* 185:85-98
- Cartigny P (2005) Stable isotopes and the origin of diamonds. *Elements* 1:79-84
- Chinn IL, Perritt SH, Stiefenhofer J, Stern RA (2018) Diamonds from Orapa Mine show a clear subduction signature in SIMS stable isotope data. *Contributions to Mineralogy and Petrology. Proceedings of the 11th International Kimberlite Conference.*
- Clackson SG, Moore M, Walmsley JC, Woods GS (1990) The relationship between platelet size and the frequency of the B' infrared-absorption peak in Type Ia diamond. *Philosophical Magazine B-Physics of Condensed Matter Statistical Mechanics Electronic Optical and Magnetic Properties* 62 (2):115-128.

- Creighton S, Stachel T, Matveev S, Höfer H, McCammon C, Luth RW (2009) Oxidation of the Kaapvaal lithospheric mantle driven by metasomatism. *Contributions to Mineralogy and Petrology* 157(4):491–504
- Davis GL (1977) The ages and uranium contents of zircons from kimberlites and associated rocks. *Year Book Carnegie Institution of Washington*, 76 pp.631-635.
- Dawson JB (1980) *Kimberlites and their xenoliths*. Springer-Ver-lag, Berlin Heidelberg New York.
- Day HW (2012) A revised diamond-graphite transition curve. *American Mineralogist* 97:52-62
- Deines P, Harris JW, Gurney JJ (1993) Depth-related carbon isotope and nitrogen concentration variability in the mantle below the Orapa kimberlite, Botswana, Africa. *Geochimica Cosmochimica Acta* 57(12):2781-2796
- Deines P, Harris JW (2004) New insights into the occurrence of ^{13}C -depleted carbon in the mantle from two closely associated kimberlites: Letlhakane and Orapa, Botswana. *Lithos* 77:125-142
- Deines P, Stachel T, Harris JW (2009) Systematic regional variations in diamond carbon isotopic composition and inclusion chemistry beneath the Orapa kimberlite cluster, in Botswana. *Lithos* 112:776-784
- D’Haenens-Johansson UFS, Smith EM, Smit KV, Wang W, Moses TM (2017) The 812-carat pure Type IaB constellation diamond from Karowe- Part of an even larger rough? Extended Abstracts, 11th International Kimberlite Conference, Gaborone, Botswana. No. 11IKC-4611
- De Wit MJ, de Ronde CE, Tredoux M, Roering C, Hart RJ, Armstrong RA, Green RW, Peberdy E, Hart RA (1992) Formation of an Archaean continent. *Nature* 357(6379):553-562

- Eggler DH, Baker DR (1982) Reduced volatiles in the system C-O-H: implications to mantle melting, fluid formation and diamond genesis. In: Akimoto S, Manghnani MH (eds) High pressure research in geophysics. Centre Acad Publ, Tokyo, pp 237-250
- Erlank AJ, Waters FG, Hawkesworth CJ, Haggerty SE, Allsopp HL, Rickard RS, Menzies M (1987) Evidence for mantle metasomatism in peridotite nodules from the Kimberley pipes, South Africa. In: Menzies M, Hawkesworth CJ (eds) Mantle metasomatism. Academic Press, London, pp 221-309
- Evans T, Harris JW (1989) Nitrogen aggregation, inclusion equilibration temperatures and the age of diamonds. In: Ross J et al (eds) Kimberlites and related rocks. Geol Soc Am Special Publication vol 14. Blackwell, Carlton, pp 1001-1006
- Evans T, Kiflawi I, Luyten W, Tendeloo GV, Woods GS (1995) Conversion of platelets into dislocation loops and voidite formation in Type IaB diamonds: Proceedings of the Royal Society 882 of London Series a-Mathematical and Physical Sciences 449:295-313
- Floyd P (1991) Oceanic basalts. Springer (New York), pp 456
- Foley S, Tiepolo M, Vannucci R (2002) Growth of early continental crust controlled by melting of amphibolite in subduction zones. Nature 417(6891):837-840
- Fouch MJ, James DE, VanDecar JC, van der Lee S, Kaapvaal SG (2004) Mantle seismic structure beneath the Kaapvaal and Zimbabwe Cratons. South African Journal of Geology 107(1-2):33-44
- Fritsch E, Hainschwang T, Massi L, Rondeau B (2007) Hydrogen-related optical centers in natural diamond: An update. New Diamond and Frontier Carbon Technology 17:63-89
- Goss JP, Briddon PR, Hill V, Jones R, Rayson MJ (2014) Identification of the structure of the 3107 cm⁻¹ H-related defect in diamond. Journal of Physics: Condensed Matter 26, 145801

- Grégoire M, Bell DR, le Roex AP (2002) Trace element geochemistry of phlogopite-rich mafic xenoliths: their classification and their relationship to phlogopite-bearing peridotites and kimberlites revisited. *Contributions to Mineralogy and Petrology* 142: 603-625
- Grégoire M, Tinguely C, Bell DR, Le Roex AP (2005) Spinel lherzolite xenoliths from the Premier kimberlite (Kaarvaal craton, South Africa): nature and evolution of the shallow upper mantle beneath the Bushveld complex. *Lithos* 84:185-205
- Griffin WL, O'Reilly SY, Natapov LM, Ryan CG (2003) The evolution of lithospheric mantle beneath the Kalahari Craton and its margins. *Lithos* 71:215-241.
- Griffin WL, Ryan CG (1995) Trace elements in indicator minerals: area selection and target evaluation in diamond exploration. *Journal of geochemical Exploration* 53(1-3):311-337
- Griffin WL, Shee SR, Ryan CG, Win TT, Wyatt BA (1999) Harzburgite to lherzolite and back again: metasomatic processes in ultramafic xenoliths from the Wesselton kimberlite, Kimberley, South Africa. *Contributions to Mineralogy and Petrology* 134:232-250
- Grütter HS, Apter DB, Kong J (1999) Crust-mantle coupling: evidence from mantle-derived xenocrystic garnets. In Gurney JJ, Gurney JL, Pasco MD, Richardson SH (Eds), *The J.B Dawson Volume, Proceedings of the VIth International Kimberlite Conference, Red Roof Design, Cape Town*, pp 307-313
- Grütter HS, Gurney JJ, Menzies AH, Winter F (2004) An updated classification scheme for mantle-derived garnet, for use by diamond explorers. *Lithos* 77:841-857
- Grütter H, Latti D, Menzies A (2006) Cr-saturation arrays in concentrate garnet compositions from kimberlite and their use in mantle barometry. *Journal of Petrology* 47:801-820
- Grütter HS (2009) Pyroxene xenocryst geotherms: Techniques and application. *Lithos* 112(Supplement 2):1167-1178

- Gurney JJ, Jakob W, Dawson JB (1979) Megacrysts from the Monastery kimberlite pipe, South Africa. *The Mantle Sample: Inclusion in Kimberlites and Other Volcanics*, pp 227-243
- Gurney JJ, Harris JW, Rickard RS (1984) Silicate and oxide inclusions in diamonds from the Orapa Mine, Botswana. *Kimberlites II: the mantle and crust-mantle relationships*. Elsevier, Amsterdam, pp 3-9
- Gurney JJ, Helmstaedt HH, Richardson SH, Shirey SB (2010) Diamonds through Time. *Economic Geology* 105:689-712.
- Hanson EK, Moore JM, Bordy EM, Marsh JS, Howarth G, Robey J (2009) Cretaceous erosion in central South Africa: evidence from upper-crustal xenoliths in kimberlite diatremes. *South African Journal of Geology* 112 (2):125-140
- Harley SL (1984) An experimental study of the partitioning of Fe and Mg between garnet and orthopyroxene. *Contributions to Mineralogy and Petrology* 86:359-373
- Harris JW (1968) The recognition of diamond inclusions. Part 1: syngenetic mineral inclusions *Industrial Diamond Review*, 28, pp. 402-410
- Harris JW, Hawthorne JB, Oosterveld MM (1986) A composition of characteristics of diamonds from the Orapa and Jwaneng kimberlite pipes in Botswana. Extended Abstract. 4-th International Kimberlite Conference, Perth, pp. 395-397
- Harte B (1983) Mantle peridotites and processes - the kimberlite sample. In: Hawkesworth CJ, Norry MJ (eds) *Continental basalts and mantle xenoliths*. Shiva, Nantwich, pp 46-91
- Harte B (1977) Rock nomenclature with particular relation to deformation and recrystallisation textures in olivine-bearing xenoliths. *Journal of Geology* 85:279-288

- Harte B (2010) Diamond formation in the deep mantle: the record of mineral inclusions and their distribution in relation to mantle dehydration zones. *Mineralogical Magazine* 74(2):189-215
- Hasterok D, Chapman DS (2011) Heat production and geotherms for the continental lithosphere. *Earth and Planetary Science Letters* 307:59-70
- Herzberg C, Rudnick R (2012). Formation of cratonic lithosphere: an integrated thermal and petrological model. *Lithos* 149: 4-15
- Hops JJ, Gurney JJ, Harte B (1992) The Jagersfontein Cr-poor megacryst suite-towards a model for megacryst petrogenesis. *Journal of Volcanology Geothermal Research* 50:143-160
- Horstwood MS, Nesbitt RW, Noble SR, Wilson JF (1999) U-Pb zircon evidence for an extensive early Archean craton in Zimbabwe: A reassessment of the timing of craton formation, stabilization, and growth. *Geology* 27(8):707-710
- Hunt L, Stachel T, McCandless TE, Armstrong J, Muehlenbachs K (2012) Diamonds and their mineral inclusions from the Renard kimberlites in Quebec. *Lithos* 142:267-284
- Ickert RB, Stachel T, Stern RA, Harris, JW (2013) Diamond from recycled crustal carbon documented by coupled $\delta^{18}\text{O}$ - $\delta^{13}\text{C}$ measurements of diamonds and their inclusions. *Earth and Planetary Science Letters* 364:85-97
- Ireland TR, Rudnick RL, Spetsius Z (1994) Trace elements in diamond inclusions from eclogites reveal link to Archean granites. *Earth and Planetary Science Letters* 128:199-213
- Jacob DE (2004) Nature and origin of eclogite xenoliths from kimberlites. *Lithos* 77:295-316
- Johnson KTM, Dick HJB, Shimizu N (1990) Melting in the oceanic upper mantle: an ion microprobe study of diopsides in abyssal peridotites. *Journal of Geophysics Research* 95:2661-2678

- Kaminsky FV, Khachatryan GK (2001) Characteristics of nitrogen and other impurities in diamond, as revealed by infrared absorption data. *Canadian Mineralogist* 29:1733-1745
- Key RM, Ayres N (2000) The 1998 edition of the national geological map of Botswana. *Journal of African Earth Sciences* 30(3):427-451
- Kiflawi I, Bruley J, Luyten W, Van Tendeloo G (1998) 'Natural' and 'man-made' platelets in Type Ia diamonds. *Philosophical Magazine B* 78:299-314
- Kirkley MB, Gurney JJ, Otter ML, Hill SJ, Daniels LR (1991) The application of C isotope measurements to the identification of the sources of C in diamonds. *Applied Geochemistry* 6:477-494
- Kiseeva ES, Yaxley GM, Stepanov AS, Tkalčić H, Litasov KD, Kamenetsky VS (2013) Metapyroxenite in the mantle transition zone revealed from majorite inclusions in diamonds. *Geology* 41:883-886
- Kiseeva ES, Wood BJ, Ghosh S, Stachel T (2016) The pyroxenite-diamond connection. *Geochemical Perspectives Letters* 2:1-9
- Klemme S, Blundy JD, Wood BJ (2002) Experimental constraints on major and trace element partitioning during partial melting of eclogite. *Geochim Cosmochim Acta* 66:3109-3123
- Kopylova MG, Gurney JJ, Daniels LR (1997) Mineral inclusions in diamonds from the River Ranch kimberlite, Zimbabwe. *Contrib Mineral Petrol* 129: 366-366
- Kramers JD, Kreissig K, Jones MQ (2001) Crustal heat production and style of metamorphism: a comparison between two Archean high grade provinces in the Limpopo Belt, Southern Africa. *Precambrian Research* 112 (1-2):149-163

- Krogh EJ (1988) The garnet-clinopyroxene Fe-Mg geothermometer-a reinterpretation of existing experimental data. *Contributions to Mineralogy and Petrology* 99:44-48
- Leahy K, Taylor, W (1997) The influence of the Glennie domain deep structure on the diamonds in Saskatchewan kimberlites: *Russian Geology and Geophysics* 38:481-491.
- Li JP, O'Neill HSC, Seifert F (1995) Subsolidus phase relations in the system MgO-SiO₂-Gr-O in equilibrium with metallic Cr, and their significance for the petrochemistry of Chromium. *Journal of Petrology* 36(1):107-132
- Ludwig KR (2003) ISOPLOT 3.0: A geochronological toolkit for microsoft excel, Berkeley Geochronology Center. Special publication no. 4
- Luguet A, Behrens M, Pearson DG, König S, Herwartz D (2015) Significance of the whole rock Re-Os ages in cryptically and modally metasomatised cratonic peridotites: Constraints from HSE-Se-Te systematics. *Geochimica et Cosmochimica Acta* 164:441-463
- Luth RW, Stachel T (2014) The buffering capacity of lithospheric mantle: implications for diamond formation. *Contributions to Mineralogy and Petrology* 168(5):1-12
- Lynn M, Nowicki T, Valenta M, Robinson B, Gallagher M, Bolton R, Sexton J (2014) Lucara Diamond Files Updated Technical Report on Sedar (accessed 3rd December 2017)
- Majaule T, Hanson RE, Key RM, Singletary SJ, Martin MW, Bowring SA (2001) The Magondi Belt in northeast Botswana: regional relations and new geochronological data from the Sua Pan area. *Journal of African Earth Sciences* 32(2):257-267
- Mather K, Pearson DG, McKenzie D, Kjarsgaard B, Priestley K (2011) Constraining the depth and thermal history of cratonic lithosphere using peridotite xenolith and xenocryst thermobarometry and seismology. *Lithos* 125: 729-742

- McCandless TE, Gurney JJ (1989) Sodium in garnet and potassium in clinopyroxene: criteria for classifying mantle eclogites. In: Ross J, Jaques AL, Ferguson J, Green DH, O'Reilly SY, Danchin RV, Janse AJA (eds) Kimberlites and related rocks, vol 2. GSA Special Publication No. 14, Perth, pp 827-832
- McDonough WF, Rudnick RL (1998) Mineralogy and composition of the upper mantle. *Reviews in Mineralogy* 37:139-164
- McDonough WF, Sun S (1995) The composition of the Earth. *Chemical Geology* 120:223-253
- McGregor ID, Carter JL (1970) The chemistry of garnets and clinopyroxenes of eclogite and peridotite xenoliths from Roberts Victor Mine, South Africa. *Physics of the Earth and Planetary Interiors*. **3**, 391-397 (1970).
- McGuire AV, Francis CA, Dyar MD (1992) Mineral standards for electron microprobe analyses of oxygen. *American Mineralogist* 77:1087-1091
- Mendelsohn MJ, Milledge HJ (1995) Geologically significant information from routine analysis of the mid-infrared spectra of diamonds. *International Geology Review* 37:95-110
- Meyer HOA (1987) Inclusions in diamond. In: Nixon PH (ed) *Mantle xenoliths*. John Wiley New York pp 501-522
- Meyer HOA, Boyd FR (1972) Composition and origin of crystalline inclusions in diamonds. *Geochimica et Cosmochimica Acta* 6:1255-1273
- Meulemans TM, Borst AM, Davidheiser B, Davies GR. (2012) The origin and modification of the sub-continental lithospheric mantle of Botswana: constraints from peridotite xenoliths of the Orapa mine Botswana. 10IKC extended abstract#351
- Miensopust MP, Jones AG, Muller MR, Garcia X, Evans RL (2011) Lithospheric structures and Precambrian terrane boundaries in northeastern Botswana revealed through

- magnetotelluric profiling as part of the Southern African Magnetotelluric Experiment.
Journal of Geophysical Research 116:1978-2012
- Moore AE (2014) The origin of large irregular gem-quality type II diamonds and the rarity of blue type IIb varieties. South African Journal of Geology 117:219-236
- Moore RO, Gurney JJ, Griffin WL, Shimizu N (1991) Ultra-high pressure garnet inclusions in Monastery diamonds: trace element abundance patterns and conditions of origin.
European Journal of Mineralogy 3:213-230
- Morimoto N (1988) Nomenclature of pyroxenes. Mineralogy and Petrology 39:55-76
- Motsamai T, Harris JW, Stachel T, Pearson DG, Armstrong J (2018) Mineral inclusions in diamonds from Karowe Mine, Botswana: super-deep sources for super-sized diamonds. Mineralogy and Petrology. Proceedings of the 11th International Kimberlite Conference.
- Navon O, Hutcheon ID, Rossman GR, Wasserburg GJ (1988) Mantle-derived fluids in diamond micro-inclusions. Nature 335:784-789
- Nestola F, Nimis P, Angel RJ, Milani S, Bruno M, Prencipe M, Harris, JW. (2014). Olivine with diamond-imposed morphology included in diamond. Syngeneses or protogeneses?
International Geology Review 56 1658-1667.
- Nestola F, Jung H, Taylor LA (2017). Mineral inclusions in diamonds may be syn-chronous but not syngenetic. Nature. Communications.8.
- Nickel KG, Green DH (1985) Empirical geothermobarometry for garnet peridotites and implications for the nature of the lithosphere, kimberlites and diamonds. Earth Planetary Science Letters 73:158-170
- Nimis P, Grütter H (2010) Internally consistent geothermometers for garnet peridotites and pyroxenites. Contributions to Mineralogy and Petrology 159:427

- Nimis P, Taylor WR (2000) Single clinopyroxene thermobarometry for garnet peridotites. Part I. Calibration and testing of a Cr-in-cpx barometer and an enstatite-in-cpx thermometer. *Contributions to Mineralogy and Petrology* 139:541-554
- Nixon PH, Boyd FR (1979). Garnet bearing lherzolites and discrete nodule suites from the Malaita alnoite, Solomon Islands, S.W. Pacific, and their bearing on oceanicmantle composition and geotherm. In: Boyd, F.R., Meyer, H.O.A. (Eds.) *The mantle sample: inclusions in kimberlite and other volcanics*. American Geophysical Union, Washington D.C pp. 400-423
- Norman MD (1998) Melting and metasomatism in the continental lithosphere: laser ablation ICPMS analysis of minerals in spinel herzolites. *Contributions to Mineral and Petrology* 130: 240-255
- O'Neill HSC, Wood BJ (1979) An experimental study of Fe-Mg partitioning between garnet and olivine and its calibration as a geothermometer. *Contributions to Mineralogy and Petrology* 70:59-70
- O'Neill, HSC (1981). The Transition between spinel lherzolite and garnet lherzolite, and Its Use as a Geobarometer. *Contributions to Mineralogy and Petrology* 77:185-194
- Paton C, Hellstrom J, Paul B, Woodhead J, Hergt J (2011) Iolite: Freeware for the visualisation and processing of mass spectrometric data. *Journal of Analytical Atomic Spectrometry* 26:2508-2518
- Pearson DG, Canil D, Shirey SB (2003) Mantle samples included in volcanic rocks: xenoliths and diamonds. In: *Treatise on Geochemistry: Vol. 2 The Mantle*. Carlson RW (ed) Elsevier, New York, p 171-277

- Pearson DG, Shirey SB (1999) Isotopic dating of diamonds. In: Lambert David D, Ruiz J (eds) Application of radiogenic isotopes to ore deposit research and exploration, 12. Society of Economic Geologists, Boulder, CO, United States, pp 143–171
- Pearson DG, Wittig N (2008) Formation of Archaean continental lithosphere and its diamonds: the root of the problem. *Journal of the Geological Society* 165:895-914
- Pearson DG, Wittig N (2014) The formation and evolution of cratonic mantle lithosphere-Evidence from mantle xenoliths. In: *Treatise on Geochemistry*, Ed. R.W. Carlson, Volume 2, Chapter 3, p255-292.
- Pearson DG, Liu J, Smith CB, Mather KA, Krebs MY, Bulanova GP, Kobussen A (2017). Characteristics and origin of the mantle root beneath the Murowa diamond mine: Implications for craton and diamond formation. Special Publication of the Society of Economic Geologists, in press
- Pokhilenko NP, Sobolev NV, Boyd FR, Pearson DG, Shimizu N (1993) Megacrystalline pyrope peridotites in the lithosphere of the Siberian Platform; mineralogy, geochemical peculiarities and the problem of their origin: *Russian Geology and Geophysics* 34: 56-67
- Prinz M, Manson DV, Hlava PF, Keil K (1975) Inclusions in diamonds: garnet lherzolite and eclogite assemblages. *Physics and Chemistry of Earth* 9:797-815
- Richardson SH, Erlank AJ, Harris JW, Hart SR (1990). Eclogitic diamonds of Proterozoic age from Cretaceous kimberlites. *Nature* 346:54–56.
- Robertson R, Fox JJ, Martin AE (1934) Two Types of Diamond. *Philosophical Transactions of the Royal Society of London A* 232:463-535
- Robinson, DN (1979) Surface textures and other features of diamonds. Unpublished PhD thesis. University of Cape Town. 221 pp.

- Robinson DN, Gurney JJ, Shee SR (1984) Diamond eclogite and graphite eclogite xenoliths from Orapa, Botswana. In: Kornprobst J (ed) Kimberlites. II. The mantle and crust-mantle relationships. Elsevier, Amsterdam, pp 11-24
- Roeder PL (1994) Chromite: From the fiery rain of chondrules to the Kilauea Iki lava lake. *The Canadian Mineralogist* 32: 729-746.
- Roduit, N. JMicroVision: Image analysis toolbox for measuring and quantifying components of high-definition images. Version 1.2.7. <http://www.jmicrovision.com> (accessed 4 March 2017).
- Schulze DJ (2003) A classification scheme for mantle-derived garnets in kimberlite: a tool for investigating the mantle and exploring for diamonds. *Lithos* 71:195-213
- Shee SR, Gurney JJ (1979) The Mineralogy of xenoliths from Orapa, Botswana. American Geophysical Union, pp 37-49
- Shilobreeva S, Martinez I, Busigny V, Agrinier P, Laverne C (2011) Insights into C and H storage in the altered oceanic crust: Results from ODP/IODP Hole 1256D. *Geochimica et Cosmochimica Acta* 75(9):2237-2255
- Shirey SB, Cartigny P, Frost DJ, Keshav S, Nestola F, Nimis P, Pearson DG, Sobolev NV, Walter MJ (2013) Diamonds and the geology of mantle carbon. *Reviews in Mineralogy Geochemistry* 75(1):355-421
- Shu Q, Brey GP, Hofer HE, Zhao Z, Pearson DG (2016) Kyanite/corundum eclogites from the Kaapvaal Craton: subducted troctolites and layered gabbros from the Mid-to Early Archean. *Contributions to Mineralogy and Petrology* 171:11-34
- Simon NS, Carlson RW, Pearson DG, Davies GR (2007) The origin and evolution of the Kaapvaal cratonic lithospheric mantle. *Journal of Petrology* 48 (3):589-625

- Simon NS, Irvine GJ, Davies GR, Pearson DG, Carlson RW (2003) The origin of garnet and clinopyroxene in “depleted” Kaapvaal peridotites. *Lithos* 71 (2-4):289-322
- Smart KA, Heaman LM, Chacko T, Simonetti A, Kopylova M, Mah D, Daniels D (2009) The origin of high-MgO diamond eclogites from the Jericho Kimberlite, Canada. *Earth and Planetary Science Letters* 284(3-4):527-537
- Smart KA, Chacko T, Stachel T, Muehlenbachs K, Stern RA, Heaman LM (2011) Diamond growth from oxidized carbon sources beneath the Northern Slave Craton, Canada: a $\delta^{13}\text{C}$ -N study of eclogite-hosted diamonds from the Jericho kimberlite. *Geochim Cosmochim Acta* 75:6027-6047
- Smith CB, Pearson DG, Bulanova GP, Beard AD, Carlson RW, Wittig N, Sims K, Chimuka L, Muchemwa E (2009) Extremely depleted lithospheric mantle and diamonds beneath the southern Zimbabwe Craton. *Lithos* 112:1120-1132
- Smith EM, Shirey SB, Nestola F, Bullock ES, Wang J, Richardson SH, Wang W (2016) Large gem diamonds from metallic liquid in Earth’s deep mantle. *Science* 354:1403-1405
- Sobolev Jr NV, Kuznetsova IK, Zyuzin NI (1968) The petrology of grosspyrite xenoliths from the Zagadochnaya kimberlite pipe in Yakutia. *Journal of Petrology* 9:253-280
- Sobolev EV, Lenskaya SV, Lisoivan VI (1969) Lamellar formations in the structure of natural diamonds. *Journal of Structural Chemistry* 9:917-920
- Sobolev NV (1977) Deep-seated inclusions in kimberlites and the problem of the composition of the upper mantle. (Translated from the Russian edition, 1974). American Geophysical Union, Washington DC, pp 279
- Sobolev VS, Sobolev NV (1980) New proof on very deep subsidence of eclogitized crustal rocks. *Dokl Akad Nauk SSSR* 250:683-685

- Speich L, Kohn SC, Wirth R, Bulanova GP, Smith CB (2017) The relationship between platelet size and the B¹ infrared peak of natural diamonds revisited. *Lithos* 278281:419-426.
- Speich L, Kohn SC, Bulanova GP, Smith C.B (2018) The behaviour of platelets in natural diamonds and the development of a new mantle thermometer. *Contributions to Mineralogy and Petrology*. 173:39.
- Spetsius ZV (2004) Petrology of highly aluminous xenoliths from kimberlites of Yakutia. *Lithos* 77:525-538
- Stachel T, Harris JW (1997) Syngenetic inclusions in diamond from the Birim field (Ghana) - a deep peridotitic profile with a history of depletion and re-enrichment. *Contributions to Mineralogy and Petrology*. 127:336-352
- Stachel T, Viljoen KS, Brey GP, Harris JW (1998) Metasomatic processes in lherzolitic and harzburgitic domains of diamondiferous lithospheric mantle: REE in garnets from xenoliths and inclusions in diamonds. *Earth and Planetary Science Letters* 159:1-12.
- Stachel T, Aulbach S, Brey GP, Harris JW, Leost I, Tappert R, Viljoen KF (2004a) The trace element composition of silicate inclusions in diamonds: a review. *Lithos* 77:1-19
- Stachel T, Viljoen KS, McDade P, Harris JW (2004b) Diamondiferous lithospheric roots along the western margin of the Kalahari Craton-the peridotitic inclusion suite in diamonds from Orapa and Jwaneng. *Contributions to Mineralogy and Petrology* 147:32-47
- Stachel T, Harris JW (2008) The origin of cratonic diamonds-constraints from mineral inclusions. *Ore Geology Reviews* 34:5-32
- Stachel T, Harris JW (2009) Formation of diamond in the Earth's mantle. *Journal of Physics Condensed Matter* 21:1-10
- Stachel T. (2014) Diamond: Mineralogical Association of Canada Short Course 44, p. 1-28.

- Stachel. T, Harris. JW, Hunt. L, Muehlenbachs. K, Kobussen. A, EIMF (2015) Argyle diamonds- How subduction along the Kimberley Craton edge generated the world's biggest's diamond deposit. Society of Economic Geology, Special Publication, 20
- Stachel T, Luth RW (2015) Diamond formation-where, when and how? *Lithos* 220-223:200-220
- Stachel T, Chacko T, Luth RW (2017) Carbon isotope fractionation during diamond growth in depleted peridotite: Counterintuitive insights from modelling water-maximum CHO fluids as multi-component systems. *Earth and Planetary Science Letters* 473:44-51
- Stagno V, Ojwang DO, McCammon CA, Frost DJ (2013) The oxidation state of the mantle and the extraction of carbon from Earth's interior. *Nature* 493:84-88
- Stern RA, PalotM, Howell D, Stachel T, Pearson DG, Cartigny P, Oh A.(2014) Methods and reference materials for SIMS diamond C- and N-isotope analysis. Canadian Centre for Isotopic Microanalysis, Research Report 14-01. University of Alberta, Education and Research Archive
- Stiefenhofer J, Viljoen KS, Marsh JS (1997) Petrology and geochemistry of peridotite xenoliths from the Letlhakane kimberlites, Botswana. *Contributions to Mineralogy and Petrology.* 127:147-158
- Streckeisen A (1976) To each plutonic rock its proper name. *Earth Science Reviews* 12:1-33
- Sun S, McDonough W (1989) Chemical and isotopic systematics of oceanic basalts: implications for mantle composition and processes. Geological Society, London, Special Publications 42:313-345
- Tappert R, Stachel T, Harris JW, Muehlenbachs K, Ludwig T, Brey GP (2005) Subducting oceanic crust: the source of deep diamonds. *Geology* 33:565-568

- Tappert R, Tappert MC (2011) *Diamonds in Nature: A Guide to Rough Diamonds*. Springer Verlag, Berlin, pp 21-26
- Taylor WR, Green DH (1989) The role of reduced C-O-H fluids in mantle partial melting. In: *Kimberlites and Related Rocks: Proceedings of the 4th International Kimberlite Conference, Vol. 1*. Oxford: Blackwell Scientific, pp. 592-602.
- Taylor WR, Jaques AL, Ridd M (1990) Nitrogen-defect aggregation characteristics of some Australasian diamonds; time-temperature constraints on the source regions of pipe and alluvial diamonds: *American Mineralogist* 75:1290-1310
- Taylor WR (1998) An experimental test of some geothermometer and geobarometer formulations for upper mantle peridotites with application to the thermobarometry of fertile lherzolite and garnet websterite. *Neues Jahrbuch für Mineralogie Abhandlungen* 172:381-408
- Timmerman S, Koornneef JM, Chinn IL, Davies GR (2017) Dated eclogitic diamond growth zones reveal variable recycling of crustal carbon through time. *Earth and Planetary Science Letters* 463:178-188
- Treloar PJ (1988) The geological evolution of the Magondi mobile belt, Zimbabwe. *Precambrian Res* 38(1):55-73
- van Achterbergh E, Griffin WL, Stiefenhofer J (2001) Metasomatism in mantle xenoliths from the Letlhakane kimberlites: estimation of element fluxes. *Contributions to Mineralogy and Petrology* 141:397-414
- Van Reenen DD, Barton JM, Roering C, Smith CA, Van Schalkwyk JF (1987) Deep crystal response to continental collision: The Limpopo belt of southern Africa. *Geology* 15(1):11-14

- Viljoen KS, Smith CB, Sharp ZD (1996) Stable and radiogenic isotope study of eclogite xenoliths from the Orapa kimberlite, Botswana. *Chemical Geology* 131:235-255
- Viljoen F, Dobbe R, Smit B (2009) Geochemical processes in peridotite xenoliths from the Premier diamond mine, South Africa: evidence for the depletion and refertilisation of subcratonic lithosphere. *Lithos* 112:1133-1142
- Viljoen F, Dobbe R, Harris J, Smit B (2010) Trace element chemistry of mineral inclusions in eclogitic diamonds from the Premier (Cullinan) and Finsch kimberlites, South Africa: implications for the evolution of their mantle source. *Lithos* 118:156-168
- Walter MJ (1998) Melting of garnet peridotite and the origin of komatiite and depleted lithosphere. *Journal of Petrology* 39: 29-60
- Walter MJ, Bulanova GP, Armstrong LS, Keshav S, Blundy JD, Gudfinnsson G, Lord OT, Lennie AR, Clark SM, Smith CB (2008) Primary carbonatite melt from deeply subducted oceanic crust. *Nature* 454(7204):622-630
- Weiss Y, McNeill J, Pearson DG et al (2015) Highly saline fluids from a subducting slab as the source for fluid-rich diamonds. *Nature* 524:339-342
- Welbourn CM, Rooney MLT, Evans DJF (1989) A study from diamonds of cube and cube related shape from the Jwaneng mine. *Journal of Crystal Growth* 94:229-252
- Wiggers-de Vries DF, Bulanova GP, De Corte K, Pearson DG, Craven JA, Davies GR (2013a) Micron-scale coupled carbon isotope and nitrogen abundance variations in diamonds: evidence for episodic diamond formation beneath the Siberian Craton. *Geochimica et Cosmochimica Acta* 100:176-199
- Wiggers-de Vries DF, Pearson DG, Bulanova GP, Smelov AP, Pavlushin AD, Davies GR (2013b) Re-Os dating of sulphide inclusions zonally distributed in single Yakutian

- diamonds: Evidence for multiple episodes of Proterozoic formation and protracted timescales of diamond growth. *Geochimica et Cosmochimica Acta* 120:363-394
- Winterburn PA, Harte B, Gurney JJ (1990) Peridotite xenoliths from the Jagersfontein kimberlite pipe: I. Primary and primary-metasomatic mineralogy. *Geochimica et Cosmochimica Acta* 54:329-341
- Woods GS, Collins AT (1983) Infrared absorption spectra of hydrogen complexes in type I diamonds. *Journal of Physics and Chemistry of Solids* 44:471-475
- Woods GS (1986) Platelets and the infrared absorption of type Ia diamonds. *Proceedings of Royal Society of London, A. Mathematical and Physical Sciences.* 407:219-238
- Wudrick M, Pearson DG, Stachel T, Armstrong J, Woodland SJ, Motsumai T (2017) Age of the lithospheric mantle beneath the Karowe Diamond Mine. *Extended Abstracts, 11th International Kimberlite Conference, Gaborone, Botswana. No. 11IKC-4489*
- Wyllie PJ, Huang W (1976) Carbonation and melting reactions in the system CaO-MgO-SiO₂-CO₂ at mantle pressures with geophysical and petrological applications. *Contributions to Mineralogy and Petrology* 54:79-107
- Yurimoto H, Ohtani E (1992) Element partitioning between majorite and liquid: a secondary ion mass spectrometric study. *Geophysical Research Letters* 19(1):17-20
- Zibera L, Nimis P, Kuzmin D, Malkovets VG (2016) Error sources in single-clinopyroxene thermobarometry and a mantle geotherm for the Novinka kimberlite, Yakutia. *American Mineralogist* 101 (10):2222-2232

Appendix A-Geochemical data for Karowe xenoliths and xenocrysts

Table A1 Natural minerals and synthetic materials used as calibration standards for analysis of mineral grains from xenoliths as well as mineral inclusion in diamonds.

Standard name	Element	Analysing crystal	Origin	Reference
Gore Garnet	Al-K α	TAPJ	Gore Mountain Mine, New York, USA	Vielzeuf D, Champenois M, Valley JW, Brunet F, and Devidal JL (2005) SIMS analyses of oxygen isotopes; matrix effects in Fe-Mg-Ca garnets. Chem Geol 223:208-226. doi:10.1016/j.chemgeo.2005.07.008
Rhodonite	Mn-K α	LIFH	Sterling Hill, Franklin, New Jersey, USA	Huebner JS, Woodruff ME (1985) Chemical composition and critical evaluation of microprobe standards available in the reston microprobe facility. US Geological Survey Open File Report 85-718 (http://www.geology.wisc.edu/~johnf/ofr_85_718.pdf)
TiO ₂ Rutile	Ti-K α	PETH	synthetic TiO ₂ from MTI	http://www.mtixtl.com/tio2substrates.aspx
CaMgSi ₂ O ₆ Diopside	Ca-K α	PETH	Astimex, palest blue,	Wakefield, Quebec, Canada
Labradorite	Ca-K α	PETH	USNM 115900, Lake County, Oregon, USA	Jarosewich E, Nelen JA, Norberg JA (1980) Reference samples for electron microprobe analysis. Geostandard Newslett 4:43-47 (https://mineralsciences.si.edu/facilities/standards.htm)
Fayalite	Fe-K α	LIFH	USNM 85276, Rockport, Massachusetts, USA	
Cr ₂ O ₃ (Chromium Oxide)	Cr-K α	PET	Synthetic, Alfa Aesar, 36258, Chromium(III) oxide, 99.6 % purity (metals basis)	https://www.alfa.com
Ca ₅ (PO ₄) ₃ F Apatite	P-K α	PETH	Apatite from alkaline source, Dwyer Mine, Wilberforce, Ontario, Canada	Tacker RC (2004) Hydroxyl ordering in igneous apatite. Am Mineral 89:1411–1421
Frank Smith Pyrope Garnet	Si-K α	TAPJ	Frank Smith kimberlite, South Africa	Royal Ontario Museum collection. Composition from bulk XRF analysis
	Mg-K α	TAP		
	Al-K α	TAPJ		

Table A1 continues.....

Standard name	Element	Analysing crystal	Origin	Reference
Ni (Nickel Wire)	Ni-K α	LIFH	Synthetic, Alfa Aesar, 43132, Nickel wire, 0.5 mm dia, annealed, 99.98 % (metals basis)	https://www.alfa.com
Fo90.5	Si-K α	TAPJ	Harrat al Kishb, Saudi Arabia	McGuire AV, Francis CA, Dyar MD (1992) Mineral standards for electron microprobe analyses of oxygen. Am Mineral 77:1087-1091
	Mg-K α	TAP		
Fo93	Si-K α	TAPJ	Balsam Gap, North Carolina, USA	Yund RA (1997) Rates of grain boundary diffusion through enstatite and forsterite reaction rims. Contrib Mineral Petrol 126:224-236
	Mg-K α	TAP		
KAlSi ₃ O ₈ Sanidine	K-K α	PET	Fe-bearing K-feldspar, Itrongay, Madagascar	Ackermann S, Kunz M, Armbruster T, Schefer J and Hanni H (2005) Cation distribution in a Fe-bearing K-feldspar from Itrongay, Madagascar. A combined neutron-and X-ray single crystal diffraction study. Schweiz Miner Petrog 84:345-354. doi.org/10.5169/seals-63754
NaAlSi ₃ O ₈ Albite	Na-K α	TAP	Albite Harvard 131705, from the Harvard Mineralogical Museum, Virginia, USA	McGuire AV, Francis CA, Dyar MD (1992) Minerals standards for electron microprobe analyses of oxygen. Am Mineral 77:1087-1091 (http://iageo.com/microanalytical-reference-materials/)
Standard name	Element	Analysing crystal	Origin	Reference

These Excel Tables will be accessible through the UAL Dataverse dataset.

Table A2 Major element mineral compositions and modal proportions of 24 mantle xenoliths from Karowe mine

Table A3 Major element compositions of clinopyroxene xenocrysts

Table A4 Trace element concentrations of clinopyroxenes and garnets in peridotite, pyroxenite, and eclogite xenoliths from Karowe

Appendix B-Geochemical data for mineral inclusions in Karowe diamonds

These Excel Tables will be accessible through the UAL Dataverse dataset.

Table B1 Major- (in wt%) and trace-element (in ppm) compositions of mineral inclusions from Karowe diamonds. For trace element concentrations, the BCR2G reference material was used to confirm precision and accuracy of the results

Table B2 Composition of sulphide inclusions from Karowe diamonds, reported in both wt% and at. %

Table B3 Eclogitic bulk rock compositions (oxides in wt%, trace elements in ppm) reconstructed for 50% garnet and 50% cpx (by weight), with N-MORB trace element compositions from Sun and McDonough (1989)

Appendix C- Physical characteristics, FTIR and SIMS data for Karowe diamonds

This Excel Table will be accessible through the UAL Dataverse dataset.

Table C1 Physical characteristics, FTIR and SIMS analysis results for Karowe diamonds